ACOUSTIC BLACK HOLE EFFECT FOR VIBRATION CONTROL

LILING TANG

Ph.D

The Hong Kong Polytechnic University

2018

The Hong Kong Polytechnic University

Department of Mechanical Engineering

ACOUSTIC BLACK HOLE EFFECT FOR

VIBRATION CONTROL

LILING TANG

A thesis submitted in partial fulfillment of the requirements for
the degree of Doctor of Philosophy

August 2017

CERTIFICATE OF ORIGINALITY

I hereby declare that this thesis is my own work and that, to the best of my knowledge and belief, it reproduces no material previously published or written, nor material that has been accepted for the award of any other degree or diploma, except where due acknowledgement has been made in the text.

(Signed)

Liling Tang   (Name of student)

ABSTRACT

Developing highly-damped and light-weighted structures is of great importance for various engineering problems. The Acoustic Black Holes (ABH) effect reduces the phase velocity of flexural waves to zero when the structural thickness approaches zero according to a power-law thickness variation, resulting in zero wave reflections and high energy concentrations at the wedge tip. The ABH effect thus shows promising application potentials for vibration controls since only a very small amount of damping materials is required at the energy focalization region. In this thesis, a flexible wavelet-decomposed and energy-based model is established to study various ABH features by preserving the full coupling between the damping layers and the host 1-D ABH structure. Highly consistent with the FEM and experimental results, numerical simulations demonstrate that the proposed wavelet-based model is particularly suitable to characterize the ABH-induced drastic wavelength fluctuation phenomenon. The ABH feature as well as the effect of the wedge truncation and that of the damping layers on the vibration response of the beam is systematically analyzed. It is shown that the conventionally neglected mass of the damping layers needs particular attention when their thickness is comparable to that of the ABH wedge around the tip area. Meanwhile, this model predicts the loss of the ABH effect in a finite beam around the local resonance frequencies of the beam portion delimited and pinned by the excitation point, which should be avoided

in the particular application frequency ranges. Due to its modular and energy-based feature, the developed model offers a general platform allowing the embodiment of other control or energy harvesting elements to guide ABH structural design for various applications.

To maximum the ABH effect with a minimum achievable truncation thickness, a modified ABH thickness profile and an extended platform of constant thickness are systematically investigated using the developed model. Compared with conventional ABH profile, numerical results show that the modified thickness profile brings about a systematic increase in the ABH effect at mid-to-high frequencies in terms of system loss factor and energy distribution, especially when the truncation thickness is small and the profile parameter m is large. The use of an extended platform further increases the ABH effect to broaden the frequency band whilst providing rooms for catering particular low frequency applications.

As a further extension of the study, the performances of single ABH and multiple ABHs are compared. Multiple ABHs are shown to be able to enhance the overall low frequency performance of the ABH. Meanwhile, multiple ABHs also bring about broadband attenuation bands and wave suppression phenomena at low frequencies. To better understand the underlying physics, the developed model is expanded to an infinite structure with periodic ABH elements. Numerical results show that the periodic boundary conditions in terms of displacement and rotational slope imposed on a unit cell, based on the finite model, are sufficient to describe the

band structures of the corresponding infinite lattice. The analysis reveals that the attenuation bands correspond exactly to the band gaps of the infinite structure with the same ABH elements, resulting from the local resonances of the ABH elements. Therefore, enhancing ABH effect by increasing the taper power index m or reducing the truncation thickness h_0 would help to generate broader and lower-frequency band gaps. To simultaneously achieve band gaps at high frequencies whilst maintaining the structural strength, a new type of phononic beams is proposed by carving the uniform beam inside with two double-leaf ABH indentations. By incorporating the ABH-induced locally resonant effect and Bragg scattering effect generated by a strengthening stud connecting the two branches of the indentations, ultra-wide band gaps, covering over 90% of the entire frequency range, are achieved through a proper tuning of the ABH parameters and that of the stud. Both numerical and experimental results show that with only three cells, the proposed phononic beams allow considerable vibration energy attenuation within an ultra-broad frequency range, pointing at promising applications in vibration control and high performance wave filter design.

List of publications already published, accepted and submitted

Refereed Journal Articles:

[1] **L.L. Tang**, and L. Cheng, Ultrawide band gaps in phononic beams with double-leaf acoustic black hole indentations, *The Journal of the Acoustical Society of America* **142**, 2802-2807 (2017).

[2] **L.L. Tang**, and L. Cheng, Broadband local resonant bandgaps in periodic structures with embedded acoustic black holes, *Journal of Applied Physics* **121**，194901 (2017).

[3] **L.L. Tang**, and L. Cheng, Enhanced Acoustic Black Hole effect in beams with a modified thickness profile and extended platform, *Journal of Sound and Vibration* **391**, 116-126 (2017).

[4] **L.L. Tang**, and L. Cheng, Loss of acoustic black hole effect in a structure of finite size, *Applied Physics Letters* **109**, 014102 (2016).

[5] **L.L. Tang**, L. Cheng, H.L. Ji, and J.H. Qiu, Characterization of Acoustic Black Hole effect using a one-dimensional fully-coupled and wavelet-decomposed semi-analytical model, *Journal of Sound and Vibration* **374**, 172-184 (2016).

[6] T. Zhou, **L.L. Tang**, H.L. Ji, J.H. Qiu, and L. Cheng, Dynamic and static properties of a double-layered compound acoustic black hole structures, *International Journal of Applied Mechanics* **9**, 1750074 (2017).

Conference Papers:

[1] **L.L. Tang**, L. Cheng, A Wavelet-decomposed Semi-Analytical Model for

Acoustic Black Hole Effect Analyses, (Invited paper), *11th International Symposium on Vibration of Continuous Systems*, Llanberis, Snodonia, Wales, UK, July 16-21, 2017

[2] **L.L. Tang**, L. Cheng, 1D phononic lattice with periodic compound acoustic black hole indentations for the generation of ultra-wide energy attenuation bands, *Inter. Noise*, Hong Kong, Aug. 27-30, 2017

[3] **L.L. Tang**, L. Cheng, Ji, J.H. Qiu, Enhanced Acoustic Black Hole effect using a modified thickness profile, *Inter. Noise*, Hamgurg, Aug. 21-24, 2016.

[4] **L.L. Tang**, S. Zhang, H.L, Ji, J.H. Qiu, L. Cheng, Characterization of Acoustic Black Hole effect using a 1-D fully-coupled and wavelet-decomposed semi-analytical model, *Inter. Noise*, San Francisco, USA, Aug. 9-12, 2015

[5] **L.L. Tang**, S. Zhang, H.L, Ji, J.H. Qiu, L. Cheng, A wavelet-decomposed semi-analytical model for flexural vibration of a beam with Acoustic Black Hole effect, *16th Asia Pacific Vibration Conference*, Hanoi, Vietnam, Nov. 24-26, 2015.

Acknowledgement

At the end of my PhD journey, I would like to thank many people for their support and encouragement over the past three years. First and foremost, I would like to give my heartful gratefulness to my surpervisor Prof. Li Cheng. It is his diligent guidance that leads me from a abecedarian to a researcher, thinking issues independently, compreshensively and postively. Without his constant support and encouragement, I cannot finish my PhD study. His enthusiatic and meticulous attitude to the research will continue to motivate my research life.

I would also like to thank Prof. Steve Conlon and Prof. Edward C. Smith for their support during my visiting study in the Pennsylvania State University. They enrich me with the theoretical and experimental acoustical skills. Inditional thanks to Prof. Jinhao Qiu and Prof. Hongli Ji in Nanjing University of Aeroautics and Astronautics for their help and comments.

Many thanks also give to Dr. Su Zhang for his help of the wavelet analysis, and Dr. Peng Li for his helpful disscussion and suggestions in my research work. I also appreciate the kindness and help from my colleagues Dr. Cheng Yang, Dr. Xiang Yu, Zhongyu Hu, Tong Zhou, Li Ma, Shengbo Shan, Xiaoqi Zhang, Fuzhen Wen, Yehai Li, Hong Wang, Di Wu, and Yu Xiong in PSU.

I would like to express my special thanks to my husband, Dr. Junshi Zhang. His endless love, support, and encouragement keep me through so much tough time. I

Table of contents

List of figures

xiv

List of tables

Nomenclature

Symbol	Description
A	Complex coefficient of admissible functions
A	Lattice constant
C	Wave velocity
E	Complex stiffness
E_b	Stiffness of the beam
E_d	Stiffness of damping layers
E_k	Kinetic energy of the system
E_p	Potential energy of the system
F	Frequency
f_c	Center frequency
f_{cha}	Characteristic frequency of the ABH effect
f_R	Normalized frequency, equaling to $f*a/c$
F(t)	Applied force
F	Force matrix
g, *s*	Translation parameters of MHW
h(x)	Thickness of the tapered profile
h_b	Thickness of the uniform beam part
h_d	Thickness of damping layer

h_0	Thickness of truncation thickness
i, p	Scaling parameters of MHW
J	Imaginary unit
K	Wave vector
K	Stiffness of translational spring
$\mathbf{K}$	Stiffness matrix
l_{Uni}	Length of the uniform part
l_{ABH}	Length of the ABH part
l_p	Length of the extended platform
L_{ABH}	Sum length of the ABH part and the extended platform
L	Lagrangian of the system
M	Power index of the ABH thickness profile
$\mathbf{M}$	Mass matrix
N	Number
P	Scaling parameter of MHW
Q	Stiffness of rotational spring
$r\ s$	Translational parameters of MHW
R_0	Reflection coefficient
T	Time
T	Displacement transmission
U	Displacement along x directions

W	Displacement along z directions
W	The work done by external force
x_0	x coordinate of the truncation
x_b	x coordinate of the beam
x_d	x coordinate of damping layers
x_f	x coordinate of external force
ρ_b	Density of the beam
ρ_d	Density of damping layers
η_b	Loss factor of the beam
η_d	Loss factor of damping layers
$\bar{\eta}$	Average loss factor
E	Coefficient of the ABH tapered thickness profile
ω	Angular frequency
ω_n	Natural angular frequency
$\varphi_{i,s}(x)$	Admissible displacement functions
$\alpha(*)$	Rounds the elements of * to the nearest integers towards zero
$\beta(*)$	Rounds the elements of * to the nearest integers towards infinity
λ	Wavelength
Φ	Wave phase
Γ	Mean quadratic velocity ratio between the ABH part and the uniform part

Δf Bandwidth of the band gap

Δl Length of the stud

Chapter 1 Introduction

1.1 Overview of the Acoustic Black Hole Phenomenon

Developing advanced light-weight structures with good vibration damping and noise insulation capability is of great importance for various engineering problems. Structural waves are difficult to control because they are dispersive and can quickly spread out over the structures and the surroundings. Traditional methods of reducing structural vibrations usually require additional weight such as covering structures with heavy viscoelastic materials [1], which limits its application when considering economic efficiency, especially in the transportation industry. The approach using a graded impedance interface for attenuating structural wave reflections at the edges of plates and bar [2] may potentially allow alleviating the abovementioned drawback of traditional methods. Their applications, however, are limited in practical applications due to the technological difficulties in creating suitable impedance interfaces. Wave manipulation starts to draw the ever-increasing attention in achieving peculiar wave phenomenon, such as negative refraction and cloaking by acoustic metamaterials [3-5]. Among other technologies, the concept of Acoustic Black Hole (ABH) emerges as another interesting technique for the wave manipulation which starts to arouse intensive interest from researchers during the last decade. Due to the unique energy concentration/focalization phenomenon of the ABH, only a very small

amount of damping materials is required at the energy focalization region to achieve efficient damping of flexural waves.

The concept of the Black Hole was first proposed by Pierre Simon Laplace in 1795, referring to an object from which light could not escape. Nearly 150 years later, a similar effect was observed in acoustics by Pekeris [6], noting the absence of reflected waves in an inhomogeneous stratified fluid with a sound velocity declining to zero as depth increases. Mironov later observed a similar phenomenon in a tapered structure [7]. For a plate in particular, it was noticed that, by reducing the wall thickness to zero according to a power-law profile, the local phase and the group velocities of the flexural waves also gradually approach zero irrespective of frequencies, resulting in no energy reflection at the tip in an ideal scenario [8-11]. This tapered feature embedded in the structure was referred to as Acoustic Black Hole (ABH). The geometrical approach [11], initially applied by Krylov, shows that to obtain zero reflection, the relationship between the local thickness h and the distance from the edge x needs to satisfy certain conditions: $h(x)=\varepsilon x^{m}$ ($m\geq2$) as shown in Fig. 1.1. In a sense, the structural waves can be manipulated, through thickness changes in this case, to create energy trapping and localization so that only a very small amount of added damping materials is required for energy absorption [12-14], which is particularly important for vibration control in light-weighted structures with wide applications in aerospace and automotive industries.

2
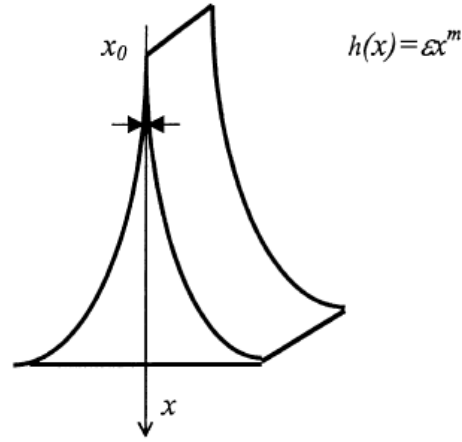
Fig. 1.1 Sketch of a power-law profile wedge from Ref. [12].

1.2 Theoretical Model and Numerical Analyses

In terms of theoretical and numerical studies, geometrical acoustics approach was first used to analyse the flexural wave propagation in tailored wedges with an ideal geometrical shape [11-14]. With a power-law profiled wedge, the wave phase of a flexural wave propagating from any arbitrary point x towards zero point can be expressed as

$$\Phi = \int_0^x k(x)\mathrm{d}x \qquad (1.1)$$

where $k(x)$ is the is a local wavenumber: $k(x) = 12^{1/4} k_p^{1/2}(\varepsilon x^m)^{-1/2}$; in which $k_p = \omega/c_p$ is the wavenumber of a plate wave with $c_p = 2c_t(1-c_t^2/c_l^2)^{1/2}$ the phase velocity; c_l and c_t are the longitudinal and shear wave velocities in a wedge material, and $\omega = 2\pi f$ is the circular frequency. As one can see, when $m \geq 2$, the phase Φ becomes infinite, which indicates the wave will never reach the edge. Therefore, the wave will never

be reflected back either and become trapped around the wedge tip, which is what mentioned above as the ABH phenomenon.

In the ideal scenario, ABH effect could achieve zero reflection in an ideal geometrical shape with thickness diminishing to zero and be used for effective vibration damping. However, truncated edges always exist in practical wedges with a residual tip thickness, which lowers the performance as 'black holes'. Therefore, as first noticed in Ref. [7], without additional damping treatment, the typical values of the reflection coefficient in steel can become as large as 50-70 % even for a small thickness truncation, indicative of the impossibility to use such wedges as practical vibration dampers. It was then observed that the situation for real wedges (with truncations) can be significantly improved by covering the wedge surfaces with thin damping layers to increase the wave energy dissipation in the energy localization area (near the sharp edges) [12-14]. The effect of a thin damping film was taken into consideration utilizing the model of Ross-Unar-Kerwin (RUK) [1] on the system loss factor and imaginary part of a flexural wave number, Im $k(x)$ as [12]

$$\text{Im}\, k\left(x\right) = \left[\frac{12^{1/4} k_p^{1/2}}{h^{1/2}(x)}\right]\left[\frac{\eta}{4} + \frac{3}{2}\frac{h_d}{h(x)}\frac{E_d}{E}\eta_\text{d}\right] \tag{1.2}$$

where h_d, E_d, and η_d is the thickness, Young modulus and loss factor of damping layers, respectively.

Then, the total reflection coefficient R_0 from the truncation point x_0 to the point x can be expressed by

4

$$R_0 = \exp(-2\int_{x_0}^{x} \operatorname{Im} k(x)\mathrm{d}x) \tag{1.3}$$

As a result, the reflection coefficient of such structures was analytically expressed in simplified formulae for different power-law profiles of order m=2, 3, 4 and for a sinusoidal profile [12]. The reflection coefficient of a beam with a termination can be also obtained through Kundt-like measurement [15]. Take a wedge of quadratic shape with $h(x)=\varepsilon x^2$ as a example, the reflection coefficient R_0 can be derived and expressed as:

$$R_0 = \exp(-2\mu_1 - 2\mu_2) \tag{1.4}$$

where

$$\mu_1 = \frac{12^{1/4} k_p^{1/2} \eta}{4\varepsilon^{1/2}} \ln(\frac{x}{x_0}) \tag{1.5}$$

$$\mu_2 = \frac{3 \times 12^{1/4} k_p^{1/2} \eta_b h_b}{4\varepsilon^{3/2}} \frac{E_b}{E} \frac{1}{x_0^2}\left(1 - \frac{x_0^2}{x^2}\right) \tag{1.6}$$

One can see from the Eqs. (1.4), (1.5) and (1.5) that, the presentence of an damping layer brings substantial reduction of the reflection coefficient, sometimes down to 1% to 3%. Corresponding numerical results in Fig. 1.2 show a smaller truncation thickness and a larger value of relative stiffness between the damping layer and the wedge structure benefit to reduce the whole reflection coefficient. Meanwhile, ABHs are most efficient at the mid-to- high frequencies.
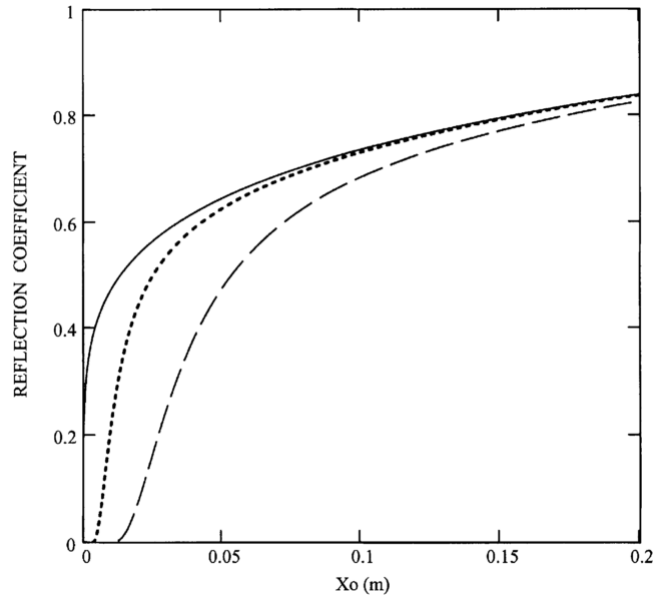
Fig. 1.2 Effect of the wedge truncation x_0 (in m) on the reflection coefficient R_0 from Ref. [12]: solid curve denotes to an uncovered wedge, dotted and dashed curves reresent to wedges covered by thin damping films with the values of relative stiffness $E_b/E=2/30$ and $E_b/E=2/3$; respectively; the film material loss factor is 0.2, and the film thickness is 5 mm.

Although a higher taper power m leads to a smaller reflection coefficient, the underlying theoretical smoothness assumption of the geometrical acoustics approach may break at this situation [12, 16]. The smoothness assumption requires that the change in the wave number must be small over a distance which is comparable to the structural wavelength, namely the normalized wave number variation is much less than 1[16]. Numerical results reveal that increasing m decreases the reflection coefficient but also increases the normalized wavenumber variation and hence may violate the smoothness criterion at lower frequencies. Therefore, the predicted results

should be carefully examined when applying the above ABH theory. A multi-objective optimization by considering both the low frequency performance of ABH and the smoothness criterion was proposed using evolutionary search [17]. To achieve a superior ABH effect in a low frequency vibration absorber, the optimized beam taper should be longer and the initial and final beam height should be small.

An impedance method which is not limited by the hypothesis of geometrical acoustics has also been proposed by Georgiev *et al.* for beam structures [18, 19], which in turn leads to a Riccati equation for the beam impedance. Numerical integration of the equation yields the frequency- and spatially-dependent impedance of the beam, from which the reflection matrix was obtained. The above two types of approaches only consider semi-infinite structures, even only the ABH wedge part in some cases [12, 14]. This is obviously different from the practical situation in which structures are finite in size with real boundary, and an ABH profile is usually only part of conventional structures. All these combined, multiple reflections take place between boundaries as well at the intersection between the ABH portion and the rest of the structure, which cannot be apprehended by the existing models. On the other hand, existing approaches consider the effect of a thin damping layer through Ross-Unar-Kerwin (RUK) model [1], which assumes the thickness of the damping layer is much smaller than that of the wedge and thus ignores its added mass effect. In practice however, the thickness of even an extremely thin damping layer would be comparable to that of the wedge tip, where ABH effect is the largest, which suggests

7

the importance of considering the added mass effect and the full coupling between the damping layer and the power-law profile wedge. This issue becomes even more important when other control and energy harvesting elements are added. Moreover, the RUK model is only applicable to a uniform damping layer. The geometrical and material characteristics as well as the location of damping layers are shown to greatly affect the performance of damping layers on energy dissipation [18, 20]. An optimization on these parameters as well as the thickness variation of the damping layers might be an additional way to achieve the maximum energy dissipation.

Another wave model was developed to calculate the mobility of plates with 1D wedge or with a power-law profiled central hole [21]. The ability of the model in predicting the ABH effect for vibration damping had also been demonstrated by experiments [22]. However, in this model, although the equivalent loss factor of a damped wedge can be obtained by separating the wedge into many discrete steps, which is still based on RUK model, large error may occur if the wedge follows large power-law profile. A 2D numerical model through the finite difference method was developed to study the ABH-induced higher model overlap factor, which again was based on RUK model [23]. The scattering effect of the flexural waves by inserting a pit of ABH in an infinite thin plate was also theoretically investigated using a wave based model without considering the effect of damping layers [24]. The ABH was shown to act as a resonant scatter to exhibit a maximum of scattering effect. Generally, nearly all existing models, to the best of our knowledge, ignore the

dynamic coupling between the damping layers and the wedge, which may be very important when the local wedge tip covered by thick damping layers or when other control and energy harvesting elements are added. Although a Rayleigh-Ritz variational energy method with considering full coupling effect of damping layers was proposed to study a rectangular plate with a 1D ABH profile [25], the application is restricted by the reachable frequency range, which is probably due to the fact that simple trigonometric shape functions can hardly characterise the rapid variation of the structural wavelength in such ABH structures. Meanwhile, as illustrated in detail below, ABH effect shows its significant potential in controlling sound radiation [26-28] and developing enhanced energy harvester [29-31] while most existing models do not offer the flexibility of considering additional control and energy harvesting elements for further potential applications.

1.3 Experiments and Implementation of the ABH

Experimental studies on ABH have been primarily applying 1D ABH in a variety of beam-like and plate-like structures, as shown in Fig. 1.3. Krylov first measured the point mobility of a steel plate with a quadratic wedge covered with an absorbing layer[32]. The results show a substantial reduction of the resonant peaks compared with uncovered wedge, which demonstrates the existence of ABH effect and implies its possibility application. A steel rod of a quadratic profile with its sharp tip

covered by absorbing layers was also tested by Kralovic and Krylov [33]. The combination of this special geometrical structure and the additional absorbing layers significant reduce the resonant vibrations in the mid-to- high frequency range. The modal analysis on a beam with a power-law profile covered by a thin damping layer shows that the ABH takes effect, as evidenced by an increase of the Modal Overlap Factor of the beam [23]. The reflection coefficient of the ABH beam terminations was also shown to decrease in a clear manner by using the Kundt-like measurement method [15]. In addition, the effect of 1D ABH is also satisfactorily investigated in practical structures experimentally, such as turbofan blades [34]. Except for vibration attenuation, the ABH effect was also used to enhance the ultrasonic radiation in wedge structures with cubic profile [35].

(a)
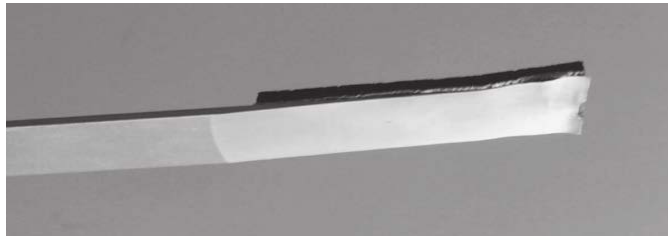
(b)

Fig. 1.3 1D ABH in (a) beam structures from Ref. [23] and (b) plate structures from

Ref. [32]

For the above 1D ABH structures, Krylov *et al.* [12] showed that the inevitable truncation (the residual thickness at the wedge tip) resulting from the limited manufacturing capability would significantly compromise the ideal ABH effect by generating wave reflections. To maximize the ABH effect, however, the ultimate pursuit of extremely thin wedge tip is of high cost and poses harsh demand for the precision machining and would also lead to tip damage of tearing and irregularities. Bowyer *et al.* investigated the effects of the manufacturing processes (such as TIG-welding, Mig-welding, gluing and direct machining) and the tolerances on damping flexural vibrations in wedge-like structures with a power-law profile [20]. Results indicated that the damage on the wedge tip does not notably affect the ABH effect and the damping layer on the flat surface of the wedge may yielded better damping effect than that on the top of the profile. Denis *et al.* [36] reported that an imperfect wedge tip would surprisingly reduce the reflection because of the resultant scattering effects. Bayod *et al*. investigated the wedge extended at the sharp edge to achieve better vibration damping compared with conventional wedge [37]. Experiments and FEM analyses were carried out to confirm this concept. Probably due to the lack of simulation tools, however, no deep explanation and parametric studies were provided in that work to guide the design of the modified wedge. Meanwhile various modified wedge thickness profiles were also proposed [15, 30]. Although similar ABH effect as the conventional profile was observed, the effect of

parameters defining the modified profiles still needs to be systematically analyzed and quantified.

Although ABH effect can ideally be achieved by a power-law profiled wedge, the exposed sharp tip of the wedge is not only delicate and structurally weak, but also impractical to use. To tackle the problem, proposals were made to move the wedges inside structures to form what is called ABH indentation, such as power-law slots machined inside plates, shown in Fig. 1.4(a), the effect of which on damping flexural vibrations is comparable with the methods using wedges at the plate edges [38, 39]. 2D ABH profiles were also incorporated into plate structures for vibration attenuation [18, 22, 40, 41] and energy focalization [42, 43], as shown in Fig. 1.4(b). Using an elliptical plate with a pit of power-law profile placed in one of its foci, the velocity fields of the plate with and without ABH were measured and analyzed [18]. It was shown that the driving-point mobility of the elliptical plate with ABH was significantly reduced compared to the other configurations. The experiments on a cylindrical plate incorporating a tapered hole of power-law profile with additional damping layer also showed a substantial suppression of the resonant vibration [22]. The effect of wave focusing and wave speed reduction was studied in time domain both numerically and experimentally [42]. The wave energy focalization could also be achieved by imperfect ABH indentation, which would however be offset from indentation centre [43].
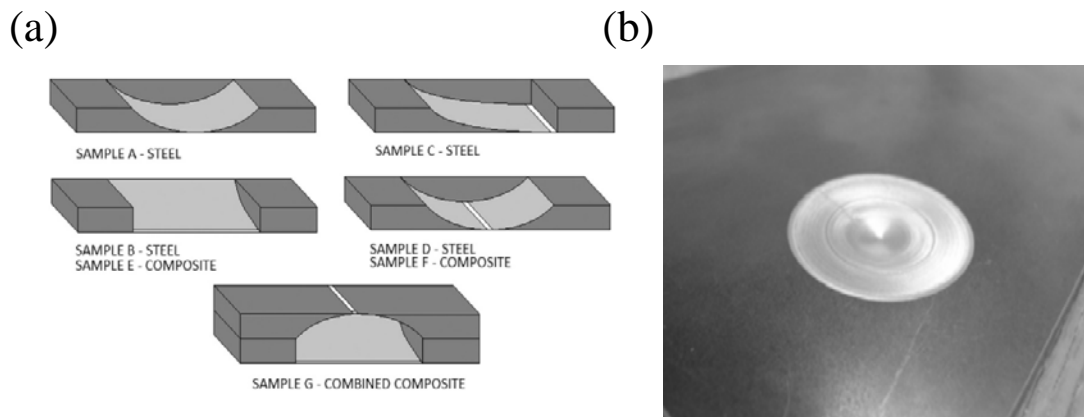
Fig. 1.4 ABH slots within plates from Ref. [38] and (b) 2D ABH in plates from Ref. [41]

Multiple 2D ABHs have also been included in structures for achieving and possible enhancing the ABH effect. Indentations of power-law profiles were drilled inside the structures [40, 41]. The experimental results show that the introduction of the central holes would increase the damping effect and the layout of the indentations determines whether the indentations will increase the damping. Various specific structures using 1-D slots and 2-D cylindrical pits were also proposed inside composite plates [44]. The resonant vibrations were greatly damped without the damping layers because of the large values of the loss factor in the composites. A plate with twenty ABH cells covered by damping layers was shown to produce significant reductions of the surface-averaged mobility in comparison with its uniform counterpart [45]. In particular, the low frequency ABH performance is mainly attributed to the low order local ABH modes.

In the above implementation of ABHs, nearly all structures suffer from the

structural weakness problems for practical applications, due to the extremely thin

residual thickness of the ABH profiles. On the other hand, almost all the references

mentioned above reveal that the ABH effect is most efficient only at mid-high

frequencies. Possible extension of the ABH effect to lower frequencies is still a great

challenge and is of particular importance for energy harvesting and noise control

applications.

1.4 Applications of the ABH effect

Up to now, ABHs have been mainly explored for the purpose of suppression of

flexural structural vibrations or sound radiation control to a less extent. For the

former, applications were initiated such as turbo-fan blades with ABH trailing edge

[34, 46], design of tennis racquets [33], or even biomedical applications such as

artificial cochlear [47]. Preliminary research also shows that a ABH can be curved

into an Archimedean spiral to reduce the space occupancy while maintaining the

efficiency in vibration reductions [48]. The ABH effect can also be used in

semi-passive vibration control with shunted piezoelectric transducers [49]. For the

later, Conlon et al. used Finite Element and Boundary Element models to investigate

both vibration and structural sound radiation of plate structures embedded with

ABHs and found that the low order local modes of the ABH could affect the

performance of the ABH effect at lower frequencies [26]. However, the broadband

absorption only happens above the frequency where the bending wave length is no smaller than the ABH diameter. Bowyer *et al.* reported some early experimental results, showing a significant reduction of the noise radiation of a plate with six ABHs [27]. The ABH feature was also incorporated into the Helmholtz resonators to increase the sound absorption bandwidth [31].

Other potential application of the ABH includes energy harvesting and wave manipulations. The initial design of energy harvesters based on ABH was firstly investigated in both steady and transient excitations [29]. Because of the high energy density concentrated on the ABH part, the harvested energy was in drastic increase compared with traditional structures, as demonstrated by the experiments [30]. On the other hand, structures with periodic ABHs were also proposed and studied, with particular attention paid to their wave propagation characteristics [50]. Resulting from the ABH effect, remarkable wave properties were achieved, such as zero group velocity in the fundamental modes, negative group refraction index, and birefraction. Applications of ABH-like profiles in various meta-surfaces were also attempted in the realization of anomalous refraction, focal lenses and phase masks [51]. An overall review about the applications of ABHs can be found in Ref. [52].

In the above applications, on one hand, the presence of vibration control or energy harvesting elements may affect the formation of the ideal ABH effect through their coupling with the host structure. Meanwhile, topological or system optimizations may be needed to achieve the maximum performance. To this end, a

15

flexible model, which allows the consideration of the full coupling between the host ABH structure and various control or energy-harvesting elements to be embedded, is of paramount importance. On the other hand, the limitation of applying the ABH effect lies in that the elastic or acoustic wavelengths should at least be comparable with the expected geometrical dimensions of practical ABHs, which can make ABHs non-effective or less effective in the low and mid-frequency range. The use of periodic arrays of ABHs may offer the possibility of making ABH more efficient at relatively low frequencies, which still warrants further investigations. Meanwhile, the possible accumulated ABH effect and wave filter effect induced by multiple or periodic ABHs also remain unknown. Explorations of these issues may shed light on the underlying physics of the ABHs and guide significant applications in future vibration control and sound absorption applications.

1.5 Research objectives and thesis layout

From the above literature review, the major existing problems related to the ABH can be identified at both fundamental and engineering level, bottlenecking its applications. The crucial issue of the coupling between the ABH near the energy concentration area and the damping layer coating is not well apprehended by the existing models. It is anticipated that, due to the high energy concentration and the weakness of the structure in that area, the added effect (in terms of mass, stiffness

and damping) of the damping layer would be very significant and important. A meticulous study of this effect, as well as thickness changes of the damping layer will be crucial for optimizing the performance of energy dissipation. Moreover, when other control elements or energy harvesting elements are added, the full coupling between these elements and the host needs to be apprehended. Besides, the finite size and the real boundaries of the structures may create multiple reflections, which cannot be apprehended by existing models. In terms of engineering applications, on one hand, manufacturing an ideally tailored power-law profile of a structure with embedded ABH tip thickness being zero can hardly be achieved in practice. The inevitable truncation at the wedge tip of the structure can significantly weaken the expected ABH effect by creating wave reflections. Therefore, on the premise of the minimum achievable truncation thickness by the current manufacturing technology, exploring ways to ensure and achieve better ABH effect becomes very important. On the other hand, ABH mainly take effect in high frequencies while practical engineering vibration or sound radiation focuses on low and medium frequencies, the contradiction of which should be resolved, such as by multiple or periodic ABHs. Meanwhile, producing the ABH effect while ensuring the mechanical rigidity and integrity of the structure also needs to be tackled before the ABH technique can find more real engineering applications. These issues will be addressed in the present thesis.

The general objective of the thesis is therefore twofold. From the basic research

viewpoint, this thesis attempts to provide answers to the aforementioned fundamental issue. From engineering application viewpoint, modified ABH profile or periodic ABHs with enhancement ABH effect as well as high structural strength will be explored to suit engineering applications.

More specifically, the following objectives will be targeted:

1). To establish a semi-analytical model for more realistic prediction and analysis of the coupling between the ABH and various damping treatment or other control elements.

2). To investigate various parameters influences on the ABH effect and further optimize damping treatment for largest energy absorption.

3). To explore method to enhance ABH effect when ideal ABH cannot be manufactured.

4). To extend the semi-analytical model to structures with multiple or periodic ABHs, for further enhancing ABH effect and broadening the ABH effectiveness to low frequencies.

5). To explore structural designs towards more effective energy trapping and dissipation while ensuring the mechanical properties of the overall structure.

The general outline of the thesis is as follows. Chapter 2 presents a wavelet-decomposed semi-analytical model to analyze a Euler-Bernoulli beam with embedded ABH features. Unlike most existing models, this model considers the full coupling between the ABH-features host structure and the damping layers coated

over its surface, as well as the finite size and real boundary conditions. The theoretical model based on Lagrange equations and the solution using Mexican Hat wavelet are given in Sec. 2.1. The cases of both the ideal ABH without truncation and the ABH with truncation are investigated to numerically validate the accuracy of the model against the Finite Element results in Sec. 2.2. Based on this model, ABH phenomena and parameter influences are analyzed in Chapter 3. The effects of the damping layers and their full coupling with the host structure are systematically investigated. The effect of the thickness, location, and the thickness variation of the damping layers are investigated with a view to increasing the ABH effect for better energy dissipation. Particularly, the loss of the ABH effect is revealed in a finite beam structure as a result of the energy localization. The developed model and the uncovered phenomena are systematically validated by experiments in Sec. 3.5.

In practice, zero ABH tip cannot be manufactured and a truncation thickness will always exist at the ABH wedge tip, which significantly increases the wave reflection and consequently reduce the ABH effect. For a given truncation thickness, methods to enhance the ABH effect are explored in Chapter 4 through a combination of a modified thickness profile and an extended platform. Subsequently in Chapter 5.1, multiple ABHs in beam structures are investigated by utilizing the developed wavelet-decomposed energy method to take advantage of the possible accumulated ABH effect and wave filter effect for vibration isolation applications. In Chapter 5.2, the energy method is further extended for investigating infinite structures with

periodic ABHs. Parametric analyses are also carried out to guide the design of structures with multiple ABHs for vibration control. To avoid the inherent structural weakness brought by the extremely thin truncation thickness, Chapter 6 investigates a double-layered compound beam with periodic double-leaf ABH indentations using a finite element (FE) package, COMSOL Multiphysics 5.2. The band structures are studied and parametric analyses are conducted to generate ultra-wide band gaps for vibration isolation and wave filter applications. Meanwhile, experiments are conducted in Chapter 6.4 to validate the numerical results. Finally, conclusions along with some suggestions for further work are summarized in Chapter 7.

Chapter 2 Wavelet-Decomposed Full-Coupled Model

As mentioned in Chapter 1, nearly all existing theoretical models ignore the full coupling between the ABH wedge and the additive components over it, which may be very important when the local wedge tip is covered by thick damping layers or other control and energy harvesting elements. Meanwhile, multiple reflections take place between structural boundaries as well at the intersection between the ABH portion and the rest of the structure in structures with finite size and real boundaries, which cannot be fully apprehended by the existing models. Therefore, the consideration of more realistic structures with finite size and boundary is necessary to guide the design of practical ABH structures. This chapter presents a semi-analytical model to analyze an Euler-Bernoulli beam with embedded ABH feature by considering its full coupling with the damping layers coated over its surface. The beam is of finite length with arbitrary boundary conditions. Based on the energy method, the damping layer is considered as an integral part of the system, thus conserving its full coupling with the host structure. Meanwhile, due to its energy-based and modular nature, this model allows easy extension to further include other embedded control or energy harvesting elements for potential applications.

The challenges in present problem lie in the fast-varying nature of the wave speed and that of the wavelength when the flexural waves enter from the uniform part into the ABH tapered region. To tackle the problem, Mexican hat wavelets are

proposed to decompose the displacement field of the system via Lagrange's equation, leading to the theoretical model presented in Section 2.1. Mexican hat wavelets are briefly introduced and analyzed in terms of their advantage in tackling the present ABH induced fast-varying wavelength problems. In Section 2.2, numerical results are compared with FEM for validations both for an ABH wedge with and without a truncation thickness. Much of the work presented in this chapter has been published in [53].

2.1 Theoretical Model and Formulation

2.1.1 Modeling Procedure

As shown in Fig. 2.1, consider an Euler-Bernoulli beam undergoing flexural vibration under a point force excitation $F(t)$ at x_f. The response is calculated at point x_m. The beam is composed of a uniform portion with constant thickness h_b from x_{b1} to x_{b2}, an ABH portion with power-law profiled thickness, $i.e.\ h(x) = \varepsilon x^m$, from x_0 and x_{b1}, and damping layers with variable thickness $h_d(x)$ from x_{d1} and x_{d2}. The whole system is assumed to be symmetrical with respect the mid-line of the beam. The non-uniform end of the beam is free and the other end is elastically supported by artificial translational and rotational springs [54, 55], the stiffness of which can be adjusted to achieve various boundary conditions. For example, when the stiffnesses of the translational and rotational springs are both set to be extremely high compared

with that of the beam, a clamped boundary is achieved. This treatment also

eliminates the geometrical boundary conditions of the system, thus facilitating the

choice of admissible functions in the following displacement-discomposed analysis

based on Hamilton principle. The damping of both the beam and the damping layer

are taken into account through complex stiffness E, *i.e.*, $E = E (1+j\eta)$, where η is the

damping loss factor.
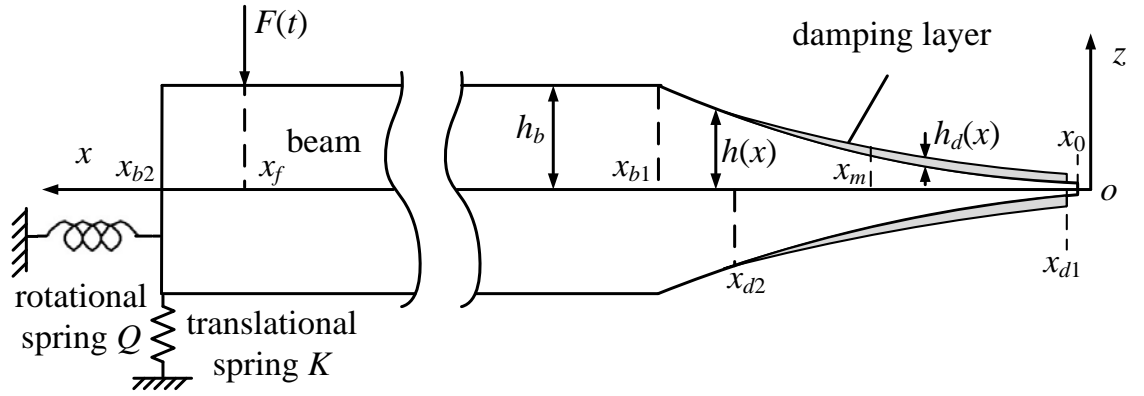
Fig. 2.1 An Euler-Bernoulli beam with symmetrical ABH power-law profiles.

Based on Euler-Bernoulli beam theory, the displacement field of the beam

writes

$$\{u, w\} = \left\{-z \frac{\partial w}{\partial x}, w(x,t)\right\} \tag{2.1}$$

where the vector $\{u, w\}$ represents the displacement of a point either on the beam or

on the damping layers, along x and z directions, respectively. Note the above

assumption assumes a perfect bonding of the damping layer with the host beam to

ensure the displacement continuity. The flexural displacement w can be expanded

23

as

$$w(x,t) = \sum_n a_n(t)\varphi_n(x) \tag{2.2}$$

where $\varphi_n(x)$ are the assumed admissible functions and $a_n(t)$ the complex unknowns

to be determined.

Upon constructing the Hamiltonian functional, its extremalization leads to the

following Lagrange's equations

$$\frac{\mathrm{d}}{\mathrm{d}t}\left(\frac{\partial L}{\partial \dot{a}_n(t)}\right) - \frac{\partial L}{\partial a_n(t)} = 0 \tag{2.3}$$

where the Lagrangian of the system L can be expressed as

$$L = E_k - E_p + W \tag{2.4}$$

in which E_k represents the kinetic energy of the system; E_p the potential energy and

W the work done by the external force. They can be obtained by

$$E_k = \frac{1}{2}\int \rho \left(\frac{\partial w}{\partial t}\right)^2 \mathrm{d}V \tag{2.5}$$

$$E_p = \frac{1}{2}\int EI(x)\left(\frac{\partial^2 w}{\partial x^2}\right)^2 \mathrm{d}x + \frac{1}{2}Kw(x_{b2},t)^2 + \frac{1}{2}Q\left(\frac{\partial w(x_{b2},t)}{\partial x}\right)^2 \tag{2.6}$$

$$W = F(t)\cdot w(x_f,t) \tag{2.7}$$

Keep in mind that the kinetic energy and the potential energy in Eqs. (2.5) and

(2.6) are the sum of the whole system, so the integration should be carried out for

both the beam and the damping layers. Based on the energy concept, the damping

layers are modeled as part of the system with its intrinsic material properties

(modulus E_d, density ρ_d) and full coupling with the beam. Similarly, should other

24

control or energy harvesting elements be present, their energy terms can also be easily added into the system.

Substituting Eqs. (2.4) to (2.7) into Eq. (2.3) yields the following linear equations in matrix form:

$$\mathbf{M\ddot{a}}(t) + \mathbf{Ka}(t) = \mathbf{f}(t) \tag{2.8}$$

Where $\mathbf{M}$ and $\mathbf{K}$ are, respectively, the mass matrix (real) and stiffness matrix (complex due to the material viscoelasticity); $\mathbf{a}(t)$ and $\mathbf{f}(t)$ are, respectively, the vector of the response $a_i(t)$ and the force. In a harmonic regime, the vector of the response and the vector of the force are represented as:

$$\mathbf{a}(t) = \mathbf{A}e^{j\omega t} \tag{2.9}$$

$$\mathbf{f}(t) = \mathbf{F}e^{j\omega t} \tag{2.10}$$

Then Eq. (2.8) can be rewritten as,

$$[\mathbf{K} - \omega^2 \mathbf{M}]\mathbf{A} = \mathbf{F} \tag{2.11}$$

The forced vibration response can be obtained by solving the Eq. (2.11) directly. For free vibration, setting the force vector in Eq. (2.11) to zero leads to the following eigenvalue equation:

$$\mathbf{M}^{-1}\mathbf{KA} = \omega^2 \mathbf{A} \tag{2.12}$$

which gives the natural frequencies and the corresponding mode shapes. Since the system is complex, recalling the express of the stiffness, the eigenvalues take complex form as

$$\omega^2 = \omega_n^2 (1 + j\eta) \tag{2.13}$$

where ω_n is the natural frequency and η the corresponding modal loss factor of the system. The latter will be particularly useful to characterize the energy absorption of the damping layers as a result of ABH effect.

2.2.2 Solution Using Mexican Hat Wavelet Expansion

In the modelling, the key challenge is to find suitable admissible functions in Eq. (2.2) to approximate the present displacement field. Although power series (polynomial functions) have been used for non-uniform beams [56, 57] or plates [58-60] with linear or nonlinear thickness variation, none of them are comparable to the degree of thickness variation required by ABH profile. In fact, the present non-uniform beam follows power-law profile with thickness quickly diminishing to zero, especially when the power is larger than 2. The resultant rapidly varying wavelength and corresponding increase in vibration amplitude, particularly near the ABH wedge tip, create particular difficulties to the choice of admissible functions. In fact, using polynomial functions to approximate the displacement as a preliminary attempt in our calculation shows strong singularity even with a few expansion terms. The Mexican hat wavelet (MHW) is hereafter demonstrated to be particularly suitable to describe the tightness of the wave packet near the ABH wedge end.

The MHW is the second derivative of the Gaussian distribution function $e^{-\frac{x^2}{2}}$, which can be defined as following after normalization [61, 62]

$$\varphi(x) = \frac{2}{\sqrt{3}} \pi^{-\frac{1}{4}} [1 - x^2] e^{-\frac{x^2}{2}} \qquad (2.14)$$

MHW drops exponentially to zero along x, which can be treated as approximately localized in [-5, 5]. After the wavelet transform, the mother wavelet of MHW in Eq. (2.14) can be expanded into a set of MHW functions

$$\varphi_{i,s}(x) = \frac{2}{\sqrt{3}} \pi^{-\frac{1}{4}} 2^{i/2} [1 - (2^i x - s)^2] e^{-\frac{(2^i x - s)^2}{2}} \qquad (2.15)$$

where i is the scaling parameter (integer) to stretch or squeeze the MHW and s the translation parameter (integer) to move the MHW along x axis. MHW functions with the scaling parameter $i=0$ and different translation parameters s are shown in Fig. 2.2. It shows that MHW is highly localized and fairly flexible by scaling and translation, which enables MHW to better cope with the local details of the ABH part. Moreover, the smoothness of MHW is also particularly desirable in the approximation. The abovementioned properties make MHW suitable as the basis functions as demonstrated later on.
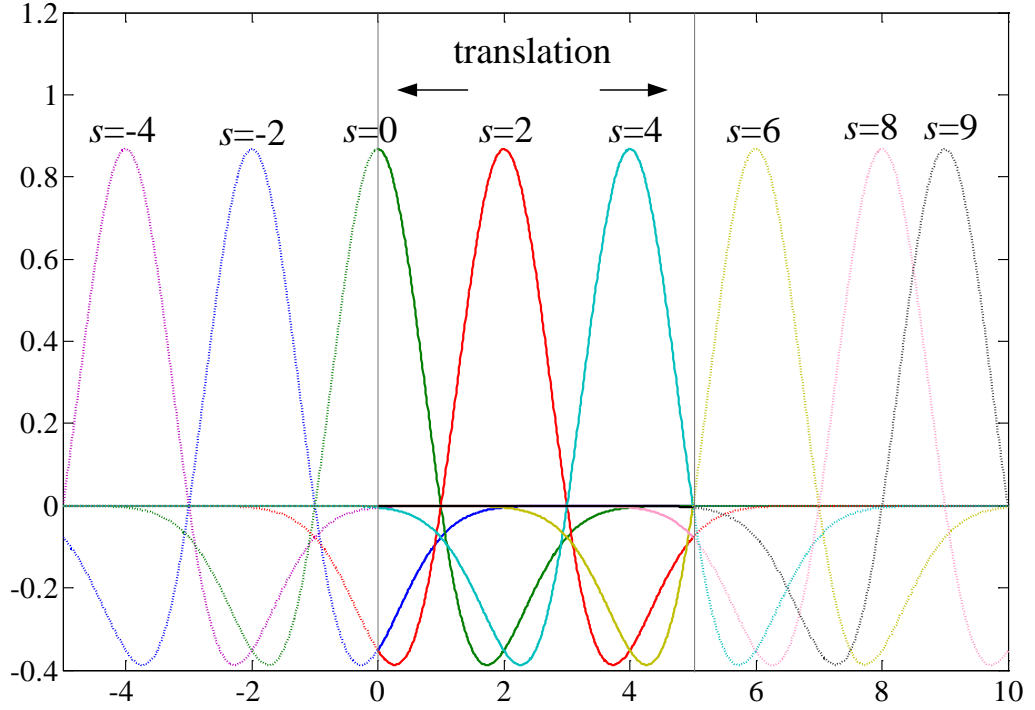
Fig. 2.2 MHW functions with the scaling parameter $i = 0$ and different translation parameters s

Choosing MHW as basis function, Eqs. (2.2) and (2.3) can then be represented as

$$w(x,t) = \sum_i \sum_s a_{i,s}(t)\varphi_{i,s}(x) \tag{2.16}$$

$$\frac{\mathrm{d}}{\mathrm{d}t}\left(\frac{\partial L}{\partial \dot{a}_{i,s}(t)}\right) - \frac{\partial L}{\partial a_{i,s}(t)} = 0 \tag{2.17}$$

Partial derivatives of the displacement over time t and x axis can be obtained as follows

$$\frac{\partial w(x,t)}{\partial t} = \sum_i \sum_s \dot{a}_{i,s}(t)\varphi_{i,s}(x) \tag{2.18}$$

$$\frac{\partial w(x,t)}{\partial x} = \sum_i \sum_s a_{i,s}(t) \frac{\partial \varphi_{i,s}(x)}{\partial x} \tag{2.19}$$

$$\frac{\partial^2 w(x,t)}{\partial x^2} = \sum_i \sum_s a_{i,s}(t) \frac{\partial^2 \varphi_{i,s}(x)}{\partial x^2} \tag{2.20}$$

where

$$\frac{\partial \varphi_{i,s}(x)}{\partial x} = \frac{2}{\sqrt{3}} \pi^{-\frac{1}{4}} e^{-\frac{(2^i x - s)^2}{2}} \left[2^i (2^i x - s)^3 - 3 \cdot 2^i (2^i x - s) \right]$$

$$\frac{\partial^2 \varphi_{i,s}(x)}{\partial x^2} = \frac{2}{\sqrt{3}} \pi^{-\frac{1}{4}} e^{-\frac{(2^i x - s)^2}{2}} \left[-2^{2i} (2^i x - s)^4 + 6 \cdot 2^{2i} (2^i x - s)^2 - 3 \cdot 2^{2i} \right]$$

Submitting Eqs. (2.18), (2.19) and (2.20) into Eqs. (2.5) and (2.6), we can get the kinetic and potential energies of the ABH beam part respectively through the integrations over the ABH part as

$$E_k^{\text{beam\_ABH}} = \frac{1}{2} \int_{x_0}^{x_{b1}} \rho_b \left[\sum_i \sum_s \dot{a}_{i,s}(t) \varphi_{i,s}(x) \right]^2 dx \int_{-h(x)}^{h(x)} dz$$

$$= \varepsilon \rho_b \int_{x_0}^{x_{b1}} \sum_i \sum_s \sum_p \sum_r \dot{a}_{i,s}(t) \dot{a}_{p,r}(t) \varphi_{i,s}(x) \varphi_{p,r}(x) x^m dx \tag{2.21}$$

$$E_p^{\text{beam\_ABH}} = \frac{1}{2} \int_{x_0}^{x_{b1}} E_b \left[\sum_i \sum_s a_{i,s}(t) \frac{\partial^2 \varphi_{i,s}(x)}{\partial x^2} \right]^2 dx \int_{-h(x)}^{h(x)} z^2 dz$$

$$= \frac{E_b \varepsilon^3}{3} \int_{x_0}^{x_{b1}} \sum_i \sum_s \sum_p \sum_r a_{i,s}(t) a_{p,r}(t) \frac{\partial^2 \varphi_{i,s}(x)}{\partial x^2} \frac{\partial^2 \varphi_{p,r}(x)}{\partial x^2} x^{3m} dx \tag{2.22}$$

where the subscripts p and r are the scaling parameter and the translation parameter respectively, same as the subscripts i and s.

Similar, the kinetic and potential energies of the uniform beam part, the damping layers part and the supported spring edges can also be obtained respectively as follows

$$E_k^{\text{beam\_Uni}} = \rho_b h_b \int_{x_{b1}}^{x_{b2}} \sum_i \sum_s \sum_p \sum_r \dot{a}_{i,s}(t) \dot{a}_{p,r}(t) \varphi_{i,s}(x) \varphi_{p,r}(x) \mathrm{d}x \tag{2.23}$$

$$E_p^{\text{beam\_Uni}} = \frac{E_b h_b^3}{3} \int_{x_{b1}}^{x_{b2}} \sum_i \sum_s \sum_p \sum_r a_{i,s}(t) a_{p,r}(t) \frac{\partial^2 \varphi_{i,s}(x)}{\partial x^2} \frac{\partial^2 \varphi_{p,r}(x)}{\partial x^2} \mathrm{d}x \tag{2.24}$$

$$E_k^{\text{damp}} = \rho_d \int_{x_{d1}}^{x_{d2}} \sum_i \sum_s \sum_p \sum_r \dot{a}_{i,s}(t) \dot{a}_{p,r}(t) \varphi_{i,s}(x) \varphi_{p,r}(x) h_d(x) \mathrm{d}x \tag{2.25}$$

$$E_p^{\text{damp}} = \frac{E_d}{3} \int_{x_{d1}}^{x_{d2}} \sum_i \sum_s \sum_p \sum_r a_{i,s}(t) a_{p,r}(t) \frac{\partial^2 \varphi_{i,s}(x)}{\partial x^2} \frac{\partial^2 \varphi_{p,r}(x)}{\partial x^2} \mathrm{d}x \\ \times \left[3\varepsilon^2 x^{2m} h_d(x) + 3\varepsilon x^m h_d^2(x) + h_d^3(x) \right] \tag{2.26}$$

$$E_p^{\text{edge}} = \frac{1}{2} K \sum_i \sum_s \sum_p \sum_r a_{i,s}(t) a_{p,r}(t) \varphi_{i,s}(x_{b2}) \varphi_{p,r}(x_{b2}) \\ + \frac{1}{2} Q \sum_{i=0}^{M} \sum_s \sum_{p=0}^{M} \sum_r a_{i,s}(t) a_{p,r}(t) \left. \frac{\partial \varphi_{i,s}(x)}{\partial x} \right|_{x=x_{b2}} \left. \frac{\partial \varphi_{p,r}(x)}{\partial x} \right|_{x=x_{b2}} \tag{2.27}$$

The total kinetic and potential energies of the system can be therefore expressed as

$$E_k = E_k^{\text{beam\_ABH}} + E_k^{\text{beam\_Uni}} + E_k^{\text{damp}} \tag{2.28}$$

$$E_p = E_p^{\text{beam\_ABH}} + E_p^{\text{beam\_Uni}} + E_p^{\text{damp}} + E_p^{\text{edge}} \tag{2.29}$$

The work done by external force writes

$$W = F(t) \sum_i \sum_s a_{i,s}(t) \varphi_{i,s}(x_f) \tag{2.30}$$

Submitting Eqs. (2.21) to (2.30) into Eqs. (2.3) and (2.4), we can get the components of the mass matrix, stiffness matrix and force vector in Eq. (2.11) as follows

$$M_{ipsr} = M_{ipsr}^{\text{beam\_Uni}} + M_{ipsr}^{\text{beam\_ABH}} + M_{ipsr}^{\text{damp}} \tag{2.31}$$

$$M_{ipsr}^{\text{beam\_Uni}} = 2\rho_b h_b \int_{x_{b1}}^{x_{b2}} \varphi_{i,s}(x) \varphi_{p,r}(x) \mathrm{d}x \tag{2.32}$$

30

$$M_{ipsr}{}^{\text{beam\_ABH}} = 2\varepsilon\rho_b \int_{x_0}^{x_{b1}} \varphi_{i,s}(x)\varphi_{p,r}(x)x^m \mathrm{d}x \tag{2.33}$$

$$M_{ipsr}{}^{\text{damp}} = 2\rho_d \int_{x_{d1}}^{x_{d2}} \varphi_{i,s}(x)\varphi_{p,r}(x)h_d(x)\mathrm{d}x \tag{2.34}$$

$$K_{ipsr} = K_{ipsr}{}^{\text{beam\_Uni}} + K_{ipsr}{}^{\text{beam\_ABH}} + K_{ipsr}{}^{\text{damp}} + K_{ipsr}{}^{\text{edge}} \tag{2.35}$$

$$K_{ipsr}{}^{\text{beam\_Uni}} = \frac{2E_b h_b{}^3}{3} \int_{x_{b1}}^{x_{b2}} \frac{\partial^2 \varphi_{i,s}(x)}{\partial x^2} \frac{\partial^2 \varphi_{p,r}(x)}{\partial x^2} \mathrm{d}x \tag{2.36}$$

$$K_{ipsr}{}^{\text{beam\_ABH}} = \frac{2E_b \varepsilon^3}{3} \int_{x_0}^{x_{b1}} \frac{\partial^2 \varphi_{i,s}(x)}{\partial x^2} \frac{\partial^2 \varphi_{p,r}(x)}{\partial x^2} x^{3m} \mathrm{d}x \tag{2.37}$$

$$K_{ipsr}{}^{\text{damp}} = \frac{2E_d}{3} \int_{x_{d1}}^{x_{d2}} \frac{\partial^2 \varphi_{i,s}(x)}{\partial x^2} \frac{\partial^2 \varphi_{p,r}(x)}{\partial x^2} \left(3\varepsilon^2 x^{2m} h_d(x) + 3\varepsilon x^m h_d{}^2(x) + h_d{}^3(x)\right) \mathrm{d}x$$

$$\tag{2.38}$$

$$K_{ipsr}{}^{\text{edge}} = K\varphi_{i,s}(x_{b2})\varphi_{p,r}(x_{b2}) + Q\frac{\partial\varphi_{i,s}(x)}{\partial x}\bigg|_{x=x_{b2}} \frac{\partial\varphi_{p,r}(x)}{\partial x}\bigg|_{x=x_{b2}} \tag{2.39}$$

$$F_{i,s} = F\varphi_{i,s}(x_f) \tag{2.40}$$

Another key issue is to choose the appropriate range of translation parameter s when the scaling parameter i is defined. Note that all MHW functions in the beam domain $[x_0, x_{b2}]$ should be included into the displacement expansion in Eq. (2.16). Meanwhile, to avoid possible singularity of the matrix **K** and **M**, those MHW functions resulting in zero $\int_{x_0}^{x_{b2}} \varphi_{i,s}(x)\mathrm{d}x$ value should be eliminated. Recall that we assume the mother wavelet of MHW is localized in [-5, 5]. If all MHW functions with different scaling parameters i are supposed to be localized in this range, this may lead to the morbidity of the matrix **K** and **M** because of the huge numerical difference among the MHW functions with different scaling parameters. Therefore, we only assign the MHW functions with the largest scaling parameter i localized in

[-5, 5], while reducing the localized range with each smaller scaling parameter by 1.

For example, given that the MHW functions with the largest scaling parameter

$i=M_{max}$ ($M_{max} \leq 5$) is localized in [-5, 5], the MHW functions with any $i \leq M_{max}$ in the

calculation should be localized in $[-5+(M_{max}-i), 5-(M_{max}-i)]$. Therefore, the

translation parameter s should be within the following range

$$s = [-4 + M_{max} - i + \alpha(x_0 2^i), \gamma(x_{b2} 2^i) + 4 - M_{max} + i],$$
$$(i = M_{min}, M_{min} + 1, ..., M_{max}, \quad 0 \leq M_{min} \leq M_{max} \leq 5) \tag{2.41}$$

where $\alpha(*)$ rounds the elements of $*$ to the nearest integers towards zero; $\gamma(*)$ rounds

the elements of $*$ to the nearest integers towards infinity. As shown in Fig. 2.2,

setting $x_0 = 0$, $x_{b2} = 5$ cm, $M = 0$, and $i = 0$, s should be within the range [-4, 9] to ensure

that all MHW functions in the beam domain [0, 5] are included. Meanwhile each

MHW function with translation s would not result in zero $\int_{x_0}^{x_{b2}} \varphi_{i,s}(x) dx$ value

(namely the value of MHW function (solid line) in [0, 5] should not always equal to

zero). Equation (2.41) shows that under the same scaling parameter i, the range of

translation parameter s is larger with the increasing beam length, *i.e.* (x_{b2}-x_0). For a

given beam length, however, both i and s can be adjusted to ensure that sufficient

terms be used in the expansion to guaranty the calculation accuracy. Generally

speaking, for low frequency calculations, only small scaling parameters are needed

with the smallest scaling parameter M_{min} usually being zero. However, to ensure an

acceptable accuracy of the high frequency calculations, the largest scaling parameter

should be enlarged accordingly while the smallest scaling parameter should be

32

carefully chosen (not necessary being zero) to avoid the huge numerical difference among different scaling parameters and consequently the morbidity of the matrix **K** and **M** as stated above.

2.2 Numerical Results and Discussions

As a numerical example, the geometrical and material parameters of the beam and the damping layers are shown in Table 2.1. The beam is of clamped-free. A harmonic driving force of 1N is applied at x_f=8 cm. The first resonant frequency of a clamped-free uniform beam with a length of 10 cm and the same material properties is used as the reference frequency [63],

$$f_{\text{ref}} = (\beta l)^2 \sqrt{\frac{E_b I}{\rho_b A l^4}} = 209.5 \, \text{Hz}, \quad (\beta l = 1.875104) \qquad (2.42)$$

To verify the accuracy of the present model, FEM results are calculated using finite element analysis software COMSOL Multiphysics v5.2 as a comparison. The non-uniform beams are modeled by 2D beams in the Solid Mechanics Module. The width of beams is set to be unit, while the uniform section and the ABH section of the beam are respectively assigned with different cross section data, namely different cross area and moment of inertia.

Table 2.1

Geometrical and material parameters used in the numerical simulation.

Geometrical parameters	Material parameters
	Beam
$\varepsilon = 0.005$	$E_b = 210$ GPa
$m = 2$	$\rho_b = 7800$ kg/m^3
$h_b = 0.125$ cm	$\eta_b = 0.005$
	Damping layers
$x_0 = 1$ cm	$E_d = 5$ GPa
$x_{b1} = 5$ cm	$\rho_d = 950$ kg/m^3
$x_{b2} = 10$ cm	$\eta_d = 0.3$

2.2.1 Ideal ABH without truncation

We first verify the accuracy of the proposed model when the ABH beam portion is perfectly fabricated without truncation, namely $x_0 = 0$. Table 2.2 and Fig. 2.3 show, respectively, the comparison between the FEM results and the results using the present approach in terms of the natural frequencies and some selected mode shapes. The scaling parameter is from two to three. Table 2.2 shows the errors for the first seven resonant frequencies between the two approaches. It can be seen that reasonable accuracy is obtained for the lower-order modes up to the fifth or sixth one. As shown in Fig. 2.3, the mode shapes calculated by the present approach are also in

acceptable agreement with the ones of FEM. Large vibration amplitude mainly concentrates on the ABH wedge tip in the high order modes, which demonstrates the ABH phenomenon. However, when the thickness of the beam tends to zero, the local phase velocity of the flexural waves also approaches to zero and the vibration amplitude becomes infinite theoretically, which can be hardly simulated by either FEM or the present numerical calculation. Therefore, the resonant frequencies and mode shapes cannot exactly match with each other when no truncation exists. Since the thickness of the beam cannot reach zero in practice, the case without truncation is not the main focus of the work, rather than just showing the general ideal ABH phenomena.

Table 2.2

Resonant frequency comparison between FEM and present approach results for the beam without truncation $x_0 = 0$.

Resonant frequency (Hz)	FEM	Present approach	Error (%)
ω_1	427.74	427.82	0.017
ω_2	964.47	960.28	-0.434
ω_3	1162.64	1154.94	-0.662
ω_4	1465.12	1470.33	0.355
ω_5	1851.49	1896.61	2.437

ω_6	2306.23	2423.38	5.080
ω_7	2831.84	3071.44	8.461
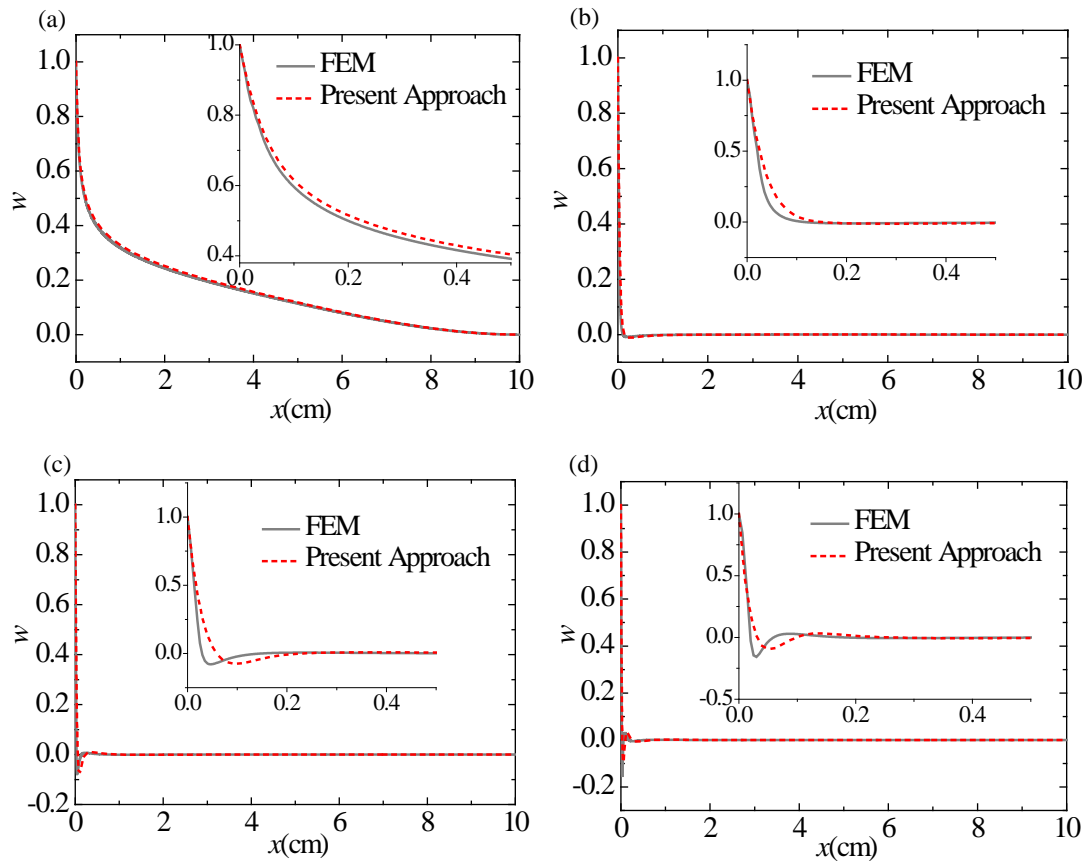
Fig. 2.3 Mode shape comparison between FEM and present approach when $x_0 = 0$ cm

for (a) first mode; (b) third mode; (c) fifth mode; and (d) seventh mode.

2.2.2 ABH with truncation

The accuracy of the present approach increases significantly with the appearance of a truncation, even very small. As shown in Table 2.3 and Fig. 2.4, the present approach guarantees extremely high accuracy for the first thirty-seven modes

in terms of both resonant frequencies (with an error less than 0.5% as compared with FEM) and mode shapes when a small truncation ($x_0 = 1$ cm corresponding to a thickness of the wedge tip of 0.01 cm) is introduced. In this case, the scaling parameter is also chosen from two to three. Similar to Fig. 2.3, Fig. 2.4 shows that ABH takes better effect at higher resonant frequencies and the wavelength decreases proportionally to the local phase velocity of the flexural waves in the ABH wedge. On the other hand, the existence of the truncation, as expected, reduces the ABH effect by increasing the vibration level of the uniform beam part compared with that in Fig. 2.3.

Table 2.3

Resonant frequency comparison between FEM and present approach for the beam with truncation $x_0 = 1$ cm.

Resonant frequency (Hz)	FEM	Present approach	Error (%)
ω_1	432.91	432.77	-0.033
ω_2	1669.52	1669.44	-0.005
ω_3	2972.79	2972.68	-0.004
ω_4	5071.01	5071.64	0.012
ω_5	8000.11	8000.41	0.004
ω_6	11338.33	11338.29	0.000
ω_7	15564.66	15563.33	-0.009

ω_8	20445.83	20445.20	-0.003
...	…	…	…
ω_{20}	132394.69	132388.11	-0.005
ω_{21}	146265.88	146258.45	-0.005
...	…	…	…
ω_{33}	365983.72	367427.36	0.394
ω_{34}	388845.60	390636.11	0.460
ω_{35}	412250.75	413190.71	0.228
ω_{36}	436519.49	436889.19	0.085
ω_{37}	461370.85	463679.23	0.500
ω_{38}	486902.30	493317.59	1.318
ω_{39}	513248.96	523609.75	2.019
ω_{40}	540113.58	546477.55	1.178

Figure 2.5 shows the calculation errors of the resonant frequencies between the FEM and the present approach when different scaling parameters are used (caped at 5%). As can be seen, when the scaling parameter is zero, only the first eight modes can be obtained with an error less than five percent. Increasing the largest scaling parameter to 1, the modal number can be significantly increased to twenty-one. However, if further increasing the largest scaling parameter to 2 while maintaining the smallest scaling parameter to zero, the accurate modal number is adversely reduced to ten, marked as diamonds. This is because of the morbidity of the matrix **K**

and **M** resulting from the huge numerical difference of the MHW functions with the scaling parameter being zero and two as mentioned above. Therefore, the zero scaling parameter is omitted in the calculation and results would be significantly improved. Varying the scaling parameter from two to three, the errors of the first forty modes nearly reduce to less than two percent compared with the FEM results. Figure 2.5 also shows the fast convergence of the present method with MHW decomposition. For low frequency applications, only very small scaling parameters are needed. For high frequency applications, the largest scaling parameter should increase provided the smallest scaling parameter is properly chosen.
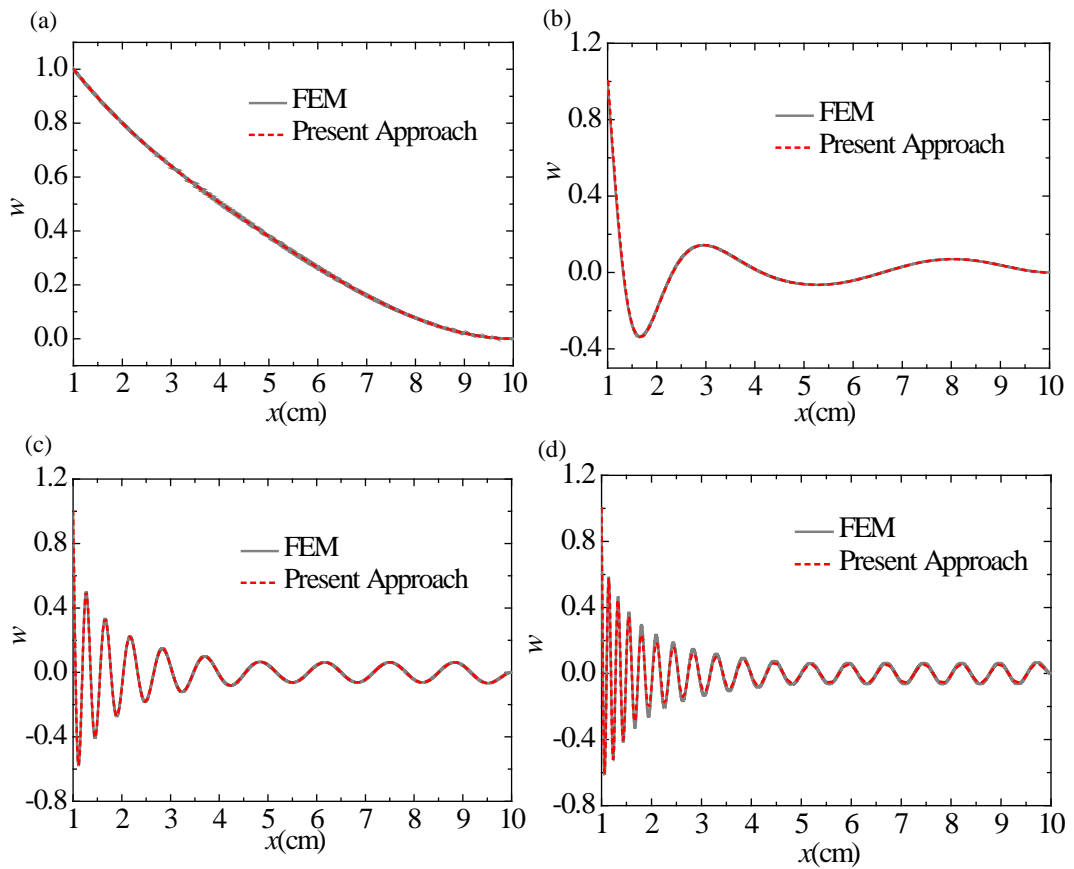
Fig. 2.4 Mode shape comparison between FEM and present approach when $x_0 = 1$ cm

for (a) first mode; (b) fifth mode; (c) twentieth mode; and (d) thirty-fifth mode.
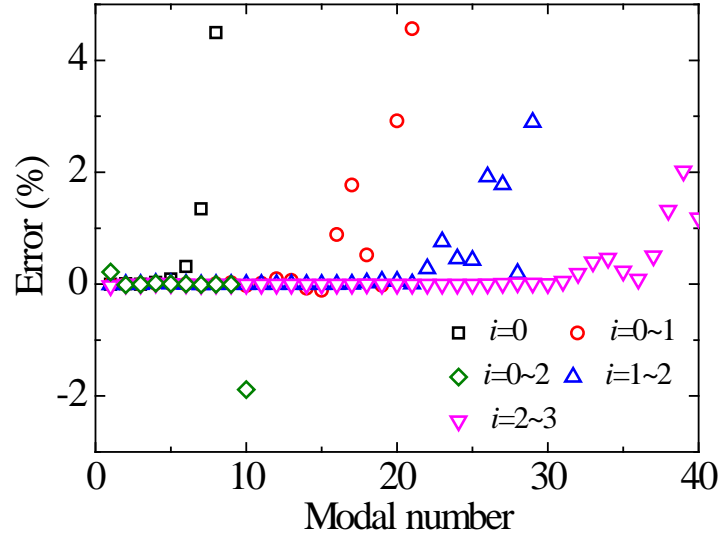
Fig. 2.5 Errors of resonant frequencies (less than five percent) between the FEM and the present approach using different scaling parameters.

Generally speaking, the above results demonstrate that the proposed model together with the use of MHW decomposition can effectively characterize the wavelength fluctuation along the beam as a result of the ABH effect and guarantee high calculation accuracy. In addition, treating MHW with the largest scaling parameter i as approximately localized within a specified region [-5, 5] is also reasonable and will not cause sensible errors in the calculations.

2.3 Short summary

In this Chapter, a semi-analytical model is established to analyze an

Euler-Bernoulli beam with embedded ABH feature and its full coupling with the damping layers coated over its surface. By using Mexican hat wavelet functions to approximate the flexural displacement, the governing equations are obtained based on Lagrange's equation. Highly consistent with the FEM results in terms of the resonant frequencies and mode shapes, especially when a truncation exists, numerical results demonstrate the validity and the suitability of the proposed wavelet-based model to characterize the wavelength fluctuation along the beam as a result of ABH effect. From the numerical results, we can see the ABH effect enables a high energy density concentration in the vicinity of the ABH wedge tip, which is conducive to energy control and utilization within a confined area. However, the practical inevitable truncation will weaken the ABH effect, which will produce wave reflection and needs damping layers treatment for energy absorption as discussed in the following Chapter.

As a final remark, the proposed model provides an efficient way to study the ABH feature and the effect of damping layers using a more realistic ABH-featured beam. Furthermore, due to its modular and energy-based nature, the proposed framework offers a general platform for further including other control or energy harvesting elements into the model to guide the design of ABH structures for various applications.

Chapter 3 ABH Phenomena, Parametric Analyses and Experimental Validations

The model developed in the previous chapter provides an efficient method to study the structure with ABH feature. In this chapter, numerical examples are given in view of demonstrating the validity of the model in producing typical ABH phenomenon and its flexibility and versatility to handle various system configurations. To be specific, ABH feature and the effects of the truncation are analyzed in Sec. 3.1. To compensate the adverse effect of the truncation, damping layers are applied over the ABH tapered part and the effects of the thickness, location and thickness variation are investigated respectively in Sec. 3.2. Moreover, due to the unique feature of this model, the importance of the full coupling between the beam and the damping layers as well as the influence of the structural finite size is evaluated in Sec. 3.3 and 3.4, respectively. The accuracy of the present model is also validated by experimental results in Sec. 3.5. These works are summarized in two journal papers [53, 64].

3.1 ABH feature and effects of the truncation

The beam and its corresponding geometrical and material parameters investigated in this chapter are the same as those shown respectively in Fig. 2.1 and

Table 2.1. To show the ABH feature and the effect of the truncation on the response, Fig. 3.1(a) first presents the cross-point mobility, $\dot{w}(x_m=6\text{cm})/f(x_f)$, for the ABH beam with or without truncation. The case of a uniform beam with the same length as the ABH beam without truncation is also used as reference. It can be seen from Fig.3.1(a) that the response of the beam with ABH feature at point x_m=6cm is slightly reduced at high frequencies. To further reveal the overall vibration level, Figs. 3.1(b) and (c) respectively show the mean quadratic velocity of the uniform portion and the mean quadratic velocity ratio Γ between the ABH portion and the uniform portion. The latter is defined as $\Gamma = 10\log\dfrac{<V^2>_{\text{ABH}}}{<V^2>_{\text{Unif}}}$ to quantify the mean energy density distribution between the ABH portion and uniform portion of the beam. The mean quadratic velocity ratio of the uniform beam is calculated within the same region corresponding to the ABH beam without truncation. As a result of ABH effect, the vibration level of the uniform portion of the ABH beam is slightly reduced at high frequencies, and the vibration energy mainly shifts to the ABH part as shown in Fig. 3.1(c). Not surprisingly, the appearance of the truncation reduces this energy shift thus weakening the ABH effect.
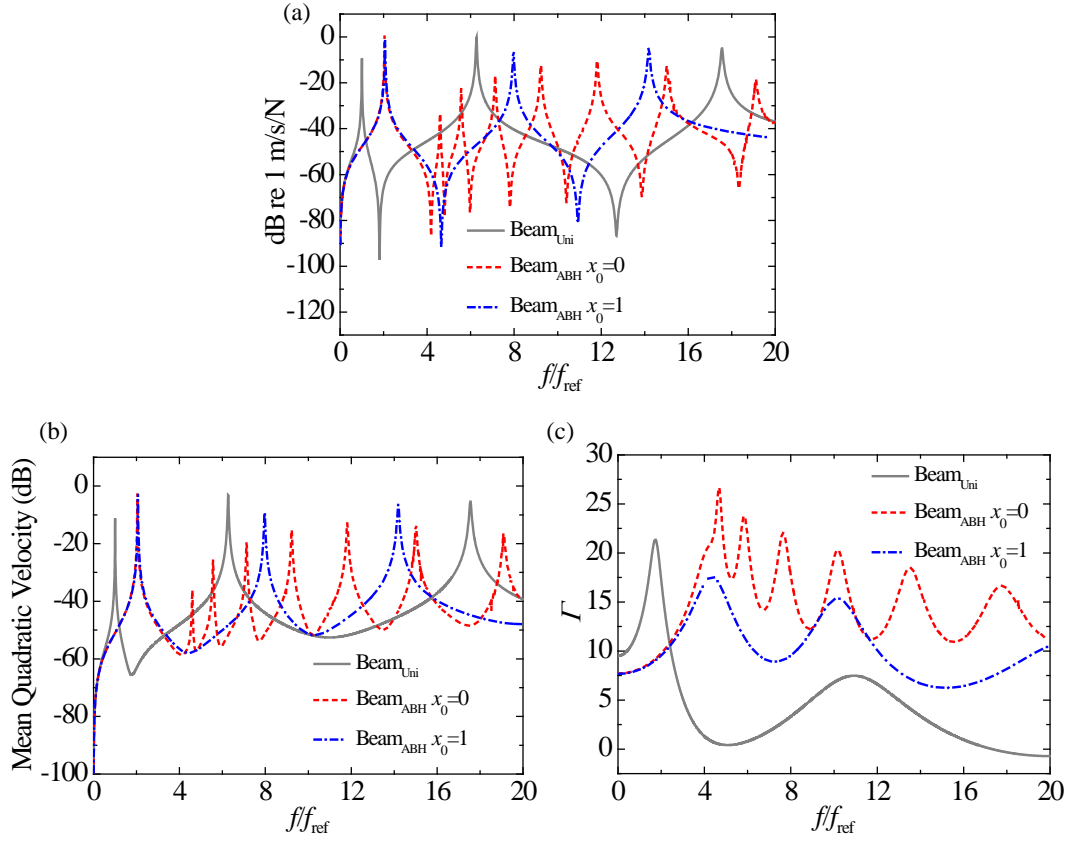
Fig. 3.1 Comparison of (a) the cross-point mobility, $\dot{w}(x_m=6\text{cm})/f(x_f)$, (b) the mean quadratic velocity of the uniform beam portion, and (c) the ratio of mean quadratic velocity of the ABH portion to the uniform beam portion for three different beam conditions.

3.2 Effects of damping layers

Damping layers are suggested to compensate for the adverse effect induced by the truncation [12, 14]. Fig. 3.2 shows the sufficient increasing of the system damping loss factors when damping layers with relatively thin thickness h_d=0.005

cm are applied over the whole surface of the ABH part of the beam. As a reference, the damping layers with same thickness and length are also applied over a uniform beam. Because of the ABH effect in higher frequencies, the concentrating energy on the ABH part enable the damping layers to take much better effect compared with that of the uniform beam, and thus greatly increase the system damping loss factors by as large as 100%.
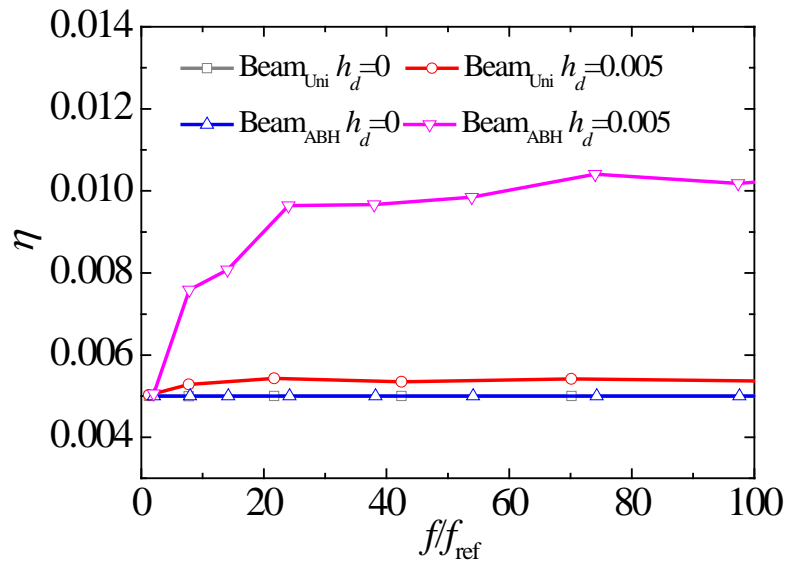
Fig. 3.2 Effect of damping layers on the system damping loss factors of the uniform beam and the beam with ABH feature, respectively ($x_d = 1 \sim 5$ cm).

3.2.1 Effects of the thickness

Figure 3.3 compares the system damping loss factors η when damping layers with different thicknesses are used to cover the whole surface of the ABH part. At the

45

first resonant frequency when the ABH part does not dominate the vibration mode, the damping layers show little effect on the system damping loss factor. With the increasing input frequency, the ABH part starts to dominate the vibration mode; therefore, thicker damping layers create larger system damping as expected. Typically, the system damping loss factor with damping layers of thickness $h_d=0.01$ cm (double of the thickness of the ABH tip) is nearly twice as large as that without damping layers ($h_d=0$). The vibration level of the uniform part and energy ratio are also shown in Fig. 3.4. Consistent with Fig. 3.3, the damping layers with thicker thickness reduce the mean quadratic velocity of the uniform part, the maximum of which can be reduced as much as 11.3 dB at the seventh resonant frequency. The damping layers, on the other hand, increase the energy in the ABH part especially at high frequencies as evidenced by an increase in the quadratic velocity ratio Γ, which demonstrates the compensation effect induced by the surface damping layers.
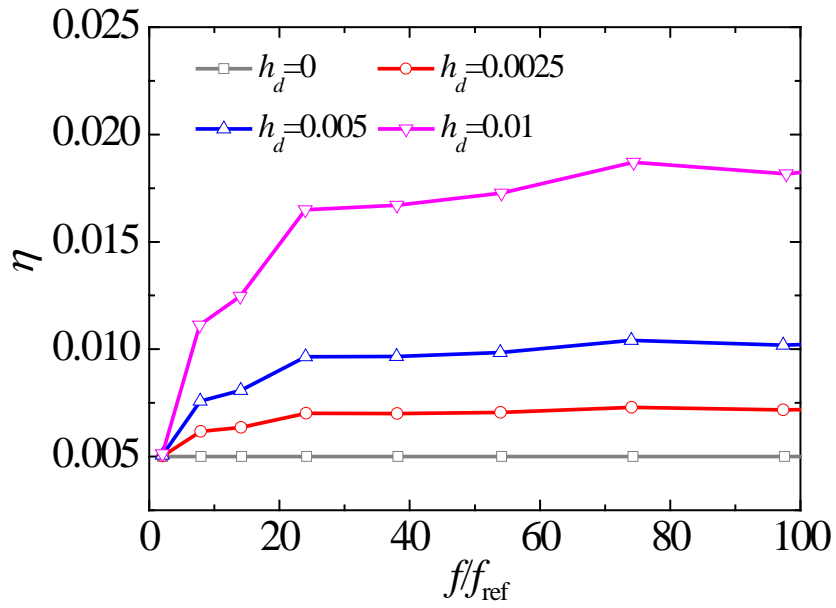
Fig. 3.3 Comparison of the system damping loss factors for different thicknesses of damping layers when x_d=1~5 cm.
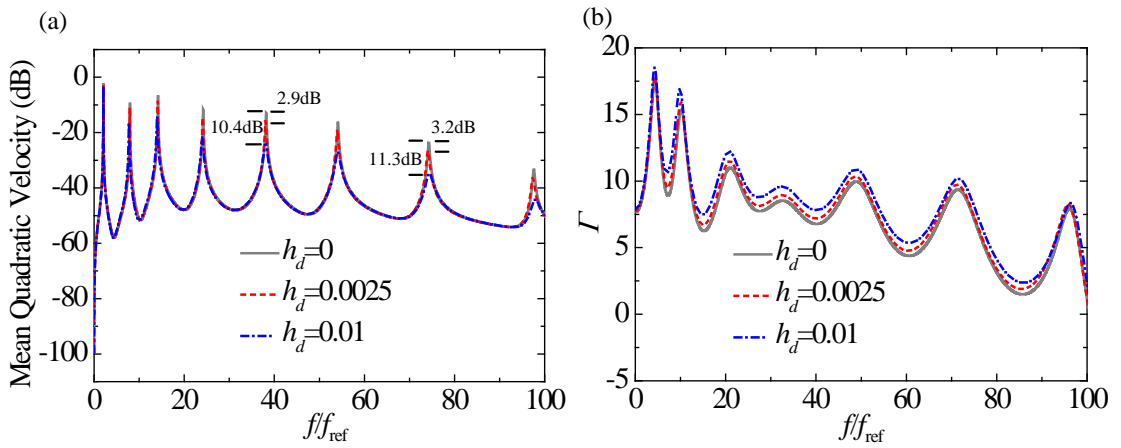
Fig. 3.4 Comparison of (a) the mean quadratic velocity of the uniform beam portion, and (b) the ratio of mean quadratic velocity of the ABH portion to the uniform beam portion for different thicknesses of damping layers when x_d=1~5 cm.

47

3.2.2 Effects of the location and thickness variation

As demonstrated above, damping layers are effective to increase the system damping at high frequencies and thus compensate to certain extent the disadvantage of the inevitable truncation. To obtain the maximum damping, the distribution of the damping layers could be adjusted. As an example, the system damping loss factors for different distributions of damping layers with constant mass are compared in Fig. 3.5. It can be seen that applying damping layers near the ABH tip rather than the whole ABH part significantly increases the system damping loss factor at high frequencies. The maximum loss factor is obtained when the damping layers with thickness of h_d=0.01 cm are deployed in the area from 1 cm to 2 cm, which is close to the ABH tip. Since this small area correspond to the highest energy density, unit mass of damping layers can consume largest energy and increase the system damping loss factor to maximum content.
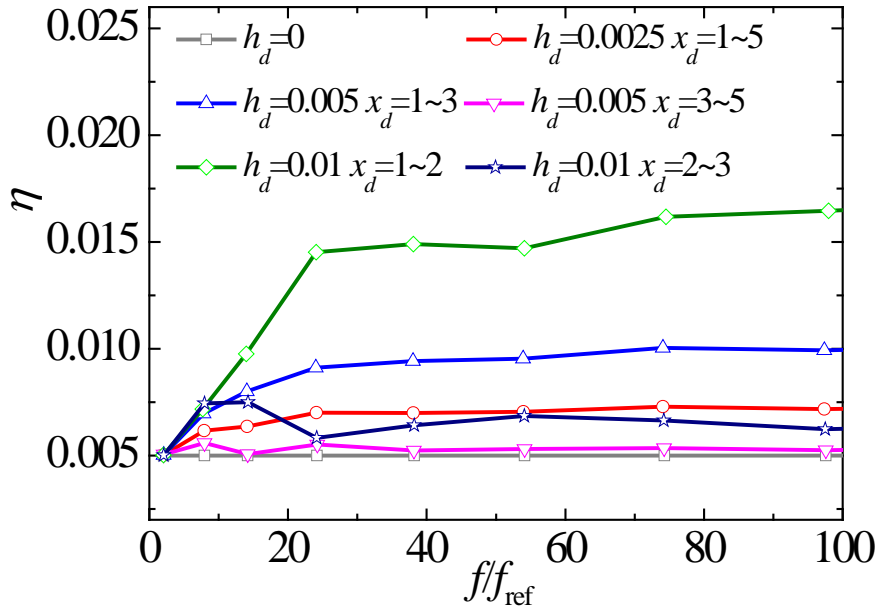
Fig. 3.5 Comparison of the system damping loss factors for different thicknesses and distributions of damping layers with constant mass.

Figure 3.6 further reveals the effect of the thickness variation of damping layers with constant mass on the system damping loss factor. The damping treatment is applied in the area from 1 cm to 2 cm to gain the maximum damping effect as suggested in Fig. 3.5. The case with uniform damping layer thickness of h_d=0.005 cm is used as reference. It can be seen that the effect of the shape of the damping layer is not quite obvious for lower-order modes. However, with the increasing ABH effect at higher frequencies, the shape of the damping layer starts to play an important role in determining the overall damping of the system. Roughly speaking, the wave packets shift closer and tighter near the ABH tip with higher energy density

49

when frequency increases as shown in Fig. 2.4. Therefore, the optimal damping application area also tends to shift towards the ABH tip. Generally, the proposed model provides a tool to eventually optimize the thickness and distribution of the damping layers to achieve the most effective damping effect for a given application, for both free and forced vibration problems.
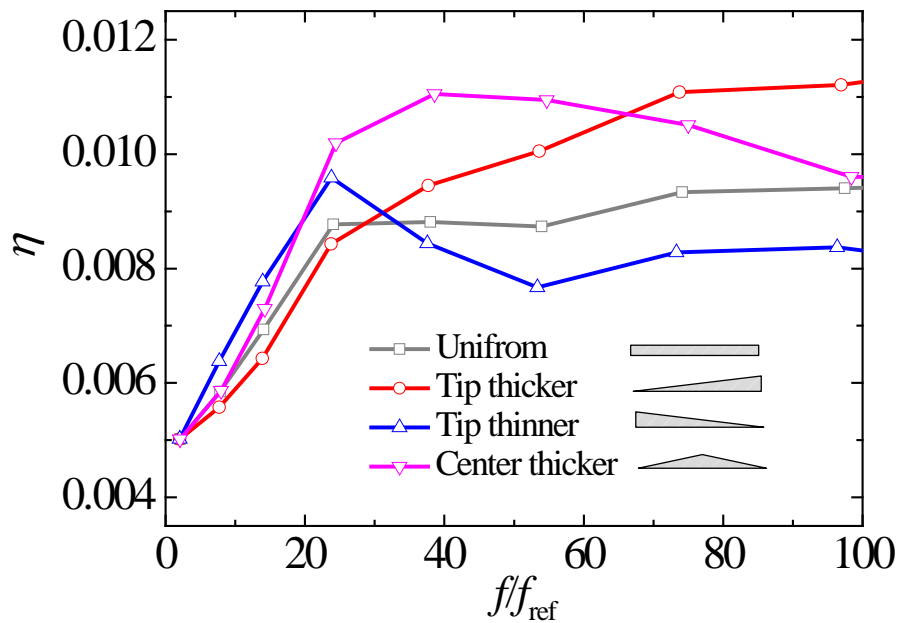
Fig. 3.6 Comparison of the system damping loss factors for different linear distributions of damping layers with constant mass while the uniform thickness damping layer corresponding to the condition of h_d=0.005 cm and x_d=1~2 cm.

3.2.3 Effects of the damping loss factor

Given a damping loss factor of damping layers of 0.3, the maximum reduced mean quadratic velocities of the uniform beam part can be as large as 11.3 dB

compared with the bare beam without damping layers as demonstrated in Fig. 3.4. In practice, the damping loss factor of damping layers can be even larger than 0.3 for some polymers, especially when the material operates in its glass transition region [65]. Fig. 3.7 presents the reduced amplitude of mean quadratic velocities of the uniform beam part compared with bare beam for different damping loss factors for the first six resonant frequencies. The larger the damping loss factor is, the more the vibration level will be reduced as expected.   The reduced mean quadratic velocities of the uniform part for larger damping loss factors at higher resonant frequencies can be appreciable (up to 14 dB in the best case). Therefore, significant damping effect can be achieved by making use of the ABH feature by properly choosing parameters and distribution of the damping layers.
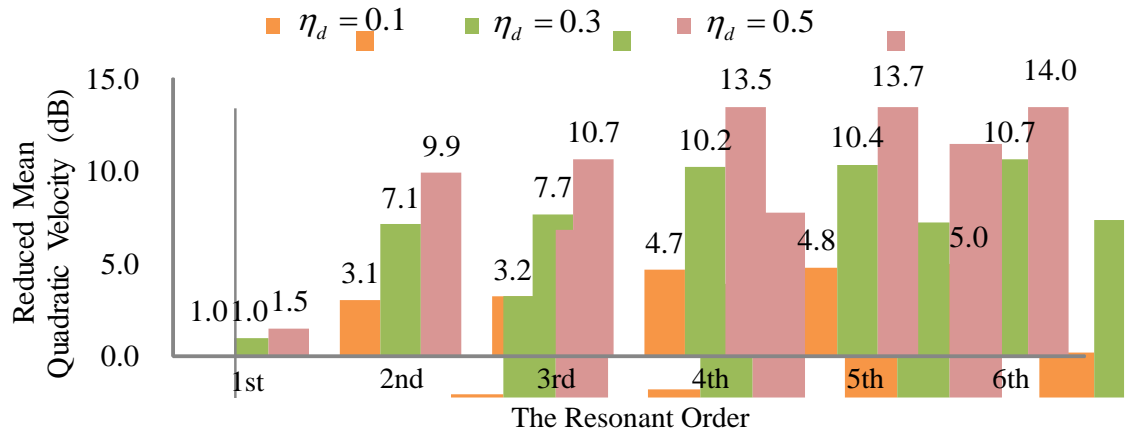
Fig. 3.7 Mean quadratic velocity reduction using damping layers with different damping loss factors (h_d=0.01 cm, x_d=1~5 cm)

3.3 Effects of the full coupling

To evaluate the importance of the full coupling between the beam and the damping layers, Fig. 3.8 and Fig. 3.9 compare the system response with/without considering the mass and the stiffness of the damping layers, respectively. From Fig. 3.8 (a), one can see that when the damping layer is uniformly applied over the whole ABH region with a thin thickness (only a half of the thickness of the ABH tip), the effect of the added mass by the damping layers is relatively small and negligible. When a thicker layer (double of the thickness of the ABH tip) only covers the tip region, however, the higher-order resonant frequencies are shifted to lower frequencies (the maximum reduction can be as large as 298 Hz in the present case) with the consideration of the mass of the damping layer, suggesting that, in this case, the added mass on the ABH tip area can be significant. This is understandable since ABH tip area dominates the vibration mode at these high frequencies as shown in Fig. 2.4. However, both cases in Fig. 3.8 show the negligible effect of the damping layer mass on the overall vibration level of the structure. When considering the stiffness of the damping layers, for the same reason, the high order resonant peaks shifts to high frequencies, more noticeably in Fig. 3.9 (b). Meanwhile, a reduction in the mean quadratic velocity can also be observed in both cases, more noticeable for the tickers layer in Fig. 3.9 (b).
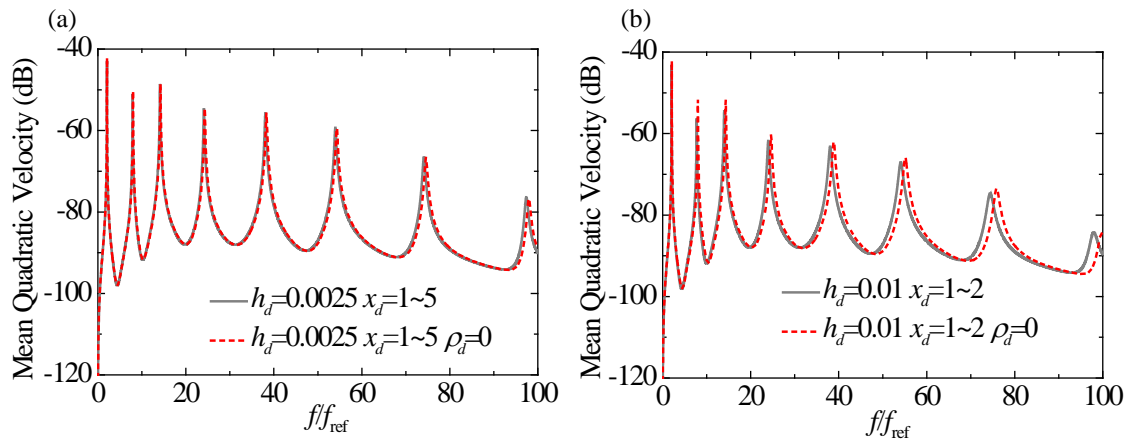
Fig. 3.8 The effect of the mass of damping layers on the mean quadratic velocity of the damping layers covered region for (a) thinner thickness and (b) thinker thickness compared with the thickness of beam tip.
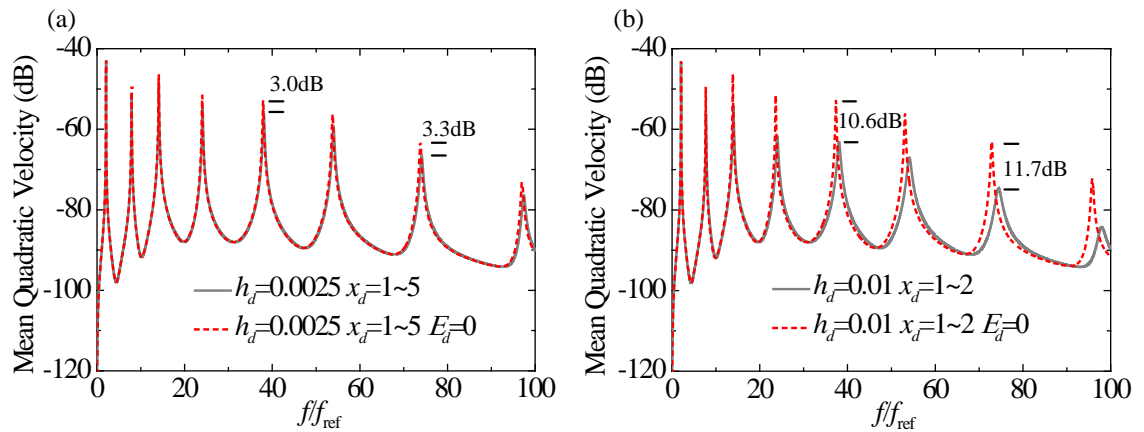
Fig. 3.9 The effect of the stiffness of damping layers on the mean quadratic velocity of the damping layers covered region for (a) thinner thickness and (b) thinker thickness compared with the thickness of beam tip.

3.4 Loss of ABH effect

Existing research indicates that, despite the truncation, the ABH effect is still highly efficient as a broadband phenomenon, although the effect is not obvious below the cut-on frequency [24]. For semi-infinite structures with ABH wedge features, the geometrical acoustic approach [11] was first proposed to analyze the flexural wave propagation properties and revealed an obvious reduction in the reflection coefficient with the increase of frequency [12]. Similar results on the reflection coefficient were also obtained by an impedance method [18]. However, these two types of approaches only deal with semi-infinite structures, namely the finite length in the wedge and the infinite length on the other portion of the structure. In practice, structures are also finite in size with real structural boundaries. In such cases, multiple reflections would take place between the boundaries and excitation points as well as the intersection between the ABH portion and the rest of the structure. Up to now, the reported theoretical models [21, 25, 46] and experiments [20, 22, 32, 37, 46, 66] on finite structures with ABH profiles all confirmed the effectiveness of the ABH effect above the cut-on frequency. With the help of the present developed model, however, we demonstrate that the ABH effect may lose its effect, or fail, in a finite beam in particular frequency bands, which will be called failure frequency bands hereafter.

A beam with a tailored ABH profile wedge, same as the sketch shown in Fig.

2.1, was employed to investigate its flexural vibration response when subjected to a unit point excitation force. The beam consists of an ABH part with a symmetrical thickness profile $h(x) = 0.00125x^2$, 12 cm long, and a uniform part with a constant thickness of 0.64 cm, 16 cm long. The beam is made of steel with a mass density of 7794 kg/m^3 and Young modulus of 200 GPa with free boundary conditions. The harmonic unit force is applied at the point, 8 cm away from the uniform end, namely x_f=24cm.

Figure 3.10 (a) reveals that the mean quadratic velocity of the ABH part, representing its overall vibration level, is particularly low in two regions around 3595 Hz and 11290 Hz, respectively. In Fig. 3.10 (b), the ratio of the mean quadratic velocity of the ABH part to that of the uniform beam part is used to quantify the effectiveness of the ABH effect, on the premise that effective ABH effect results in energy concentration in the tapered ABH region with a high positive Γ. On the contrary, when Γ is negative, we consider the ABH effect is lost or sufficiently weak, in which case we loosely call it failure of the ABH effect. As clearly seen in the Fig. 3.10 (b), around these two bottommost frequency regions the energy mainly concentrates on the uniform part rather than the ABH part as the conventional ABH effect would have suggested. This indicates a clear disappearance of effectiveness of the ABH effect around these frequencies, against the conventionally established broadband nature of the ABH feature reported in the literature. A band is defined as a failure band when its Γ value is negative. In the present case, the bandwidths of two

failure bands are 875 Hz and 1755 Hz respectively.
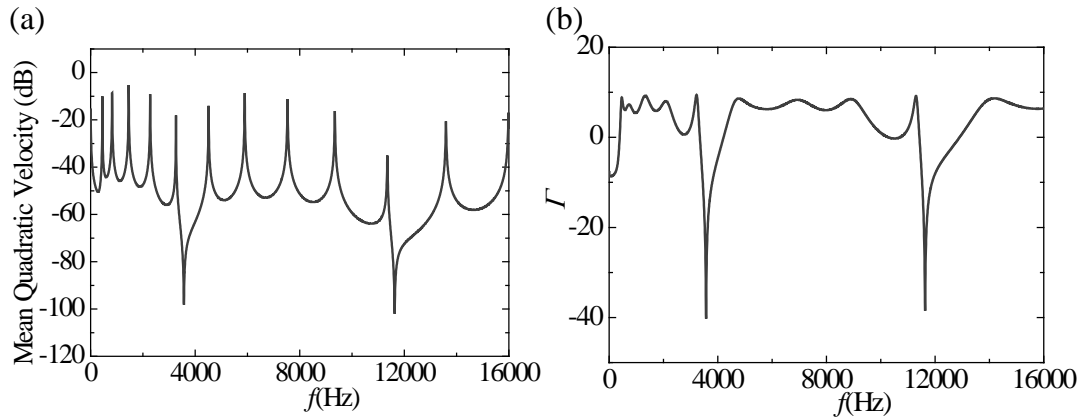
Fig. 3. 10. (a) The mean quadratic velocity of the ABH part and (b) the ratio of mean quadratic velocity of the ABH part to that of the uniform beam part.

To further demonstrate the phenomenon, Fig. 3.11 (a) and (b) depict the displacement distribution of the beam at the first and second bottommost frequencies, for two excitation locations (x_f = 24 cm, and 26 cm, respectively). As a comparison, Fig. 3 (c) also depicts the displacement distribution at two frequencies, outside and adjacent to the two failure bands, respectively (f =3220 Hz and 5840 Hz). Fig. 3.11 (c) shows typical ABH effect in that the vibration mainly concentrates on the ABH part with large vibration level near the wedge tip. However, the results in Fig. 3 (a) and (b) show that the vibration level of the ABH part at two bottommost frequencies is negligible compared with that of the uniform part, which indicates a loss of the ABH effect. It is logical to surmise that, in this situation, applying damping layers or energy harvesting elements on the ABH part would not lead to efficient damping or harvesting performance. For both excitation positions, the figure shows that the low

vibration region of the ABH part roughly starts from the excitation location.
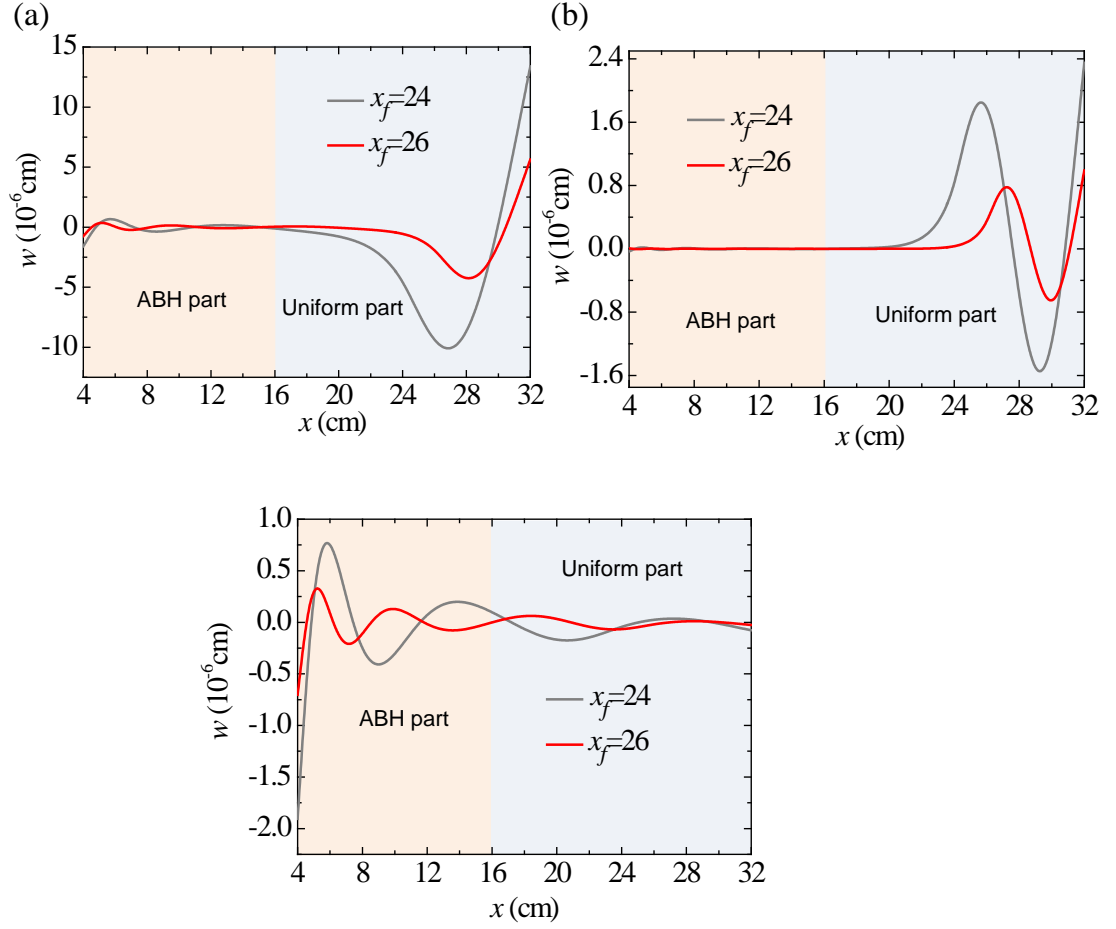
Fig. 3.11 Displacement distribution along the beam at (a) the first bottommost frequency and (b) the second bottommost frequency of the energy ratio Γ where the ABH effect fails, and (c) the frequencies outside and adjacent to the first failure bands (f =3220 Hz and 5840 Hz), with the force applied at x_f = 24 cm and x_f = 26 cm, respectively. Different highlighted areas mean the ABH part and uniform part, respectively.

A plausible reason to explain the observed phenomenon is proposed as follows. Due to the presence of the excitation, a structural discontinuity in the local

impedance is created, demarcating the beam into two subsystems, *i.e.*, the right uniform part and the left part with ABH profile. Within the failure frequency band, multiple wave reflections take place between the structure boundary and the excitation point. This allows the formation of standing waves and local resonances, thus triggering the energy localization effect. Indeed, analyses show that the ABH failure frequencies correspond to the local resonance frequencies of that uniform beam portion with pinned boundary conditions at the force excitation point and the real structural boundary at the other end. In the present case, the observed two bottommost ABH failure frequencies correspond to the first two local resonance frequencies of the beam portion with the pinned-free boundary, which can be predicted [63]. When the excitation frequency approaches the local resonance frequencies of the uniform portion delimited by the excitation point and the structural boundary, energy will be localized within that region due to the local resonance phenomenon, neutralizing the ABH effect in the ABH beam portion. To further confirm this phenomenon and explanation, we changed the excitation point to $x_f = 26$ cm (6 cm away from the end of the uniform beam portion). In this case, the first and second local resonant frequencies of the uniform beam portion are re-calculated, giving 6380 Hz and 20673 Hz, respectively. These values are reasonably close to the two bottommost frequencies corresponding to the minimum energy ratio Γ (6422 Hz and 19844 Hz).

More cases were simulated to confirm the general character of the

phenomenon and the validity of the proposed prediction of the failure frequencies. When changing the boundary conditions and excitation locations, similar ABH failure phenomenon was noticed in each case (not shown here). The first and second bottommost ABH failure frequencies are compared with the corresponding predicted local resonant frequencies of the uniform subsystem delimited by the excitation points at $x_f = 23$ cm and $x_f = 27$ cm, respectively, as displayed in Table 3.1. Treating the excitation point as a pinned constraint, the predicted local resonant frequencies are indeed very close to bottommost ABH failure frequencies for all three different boundary conditions. The failure frequency bands are also highly obvious, ranging from 542 Hz to as large as 2594 Hz. Therefore, the reported ABH failure phenomenon applies to all cases and the phenomenon can be accurately reproduced by the established wavelet-decomposed model, which should be avoided in the targeted application ranges.

TABLE 3.1. The first and second bottommost ABH failure frequencies and their comparison with corresponding predicted local resonant frequencies of the uniform beam portion delimited by the excitation points $x_f = 23$ cm and $x_f = 27$ cm, respectively, and failure frequency bands for three different boundary conditions.

Boundary conditions	Equivalent local boundary conditions	Excitation locations (cm)	Predicted local resonant frequencies (Hz)	Bottommost ABH failure frequencies (Hz)	Difference (%)	Failure frequency bands (Hz)

Free-free	pinned-free	$x_f=23$	2835	2821	0.50	717
			9188	9188	0	1202
		$x_f=27$	9186	9122	0.70	1296
			29769	29774	-0.00017	2594
Free-pinned	pinned-pinned	$x_f=23$	1815	1821	-0.33	542
			7260	7260	0	1999
		$x_f=27$	5880	5880	0	1205
			23521	23520	0.0043	2170
Free-clamped	pinned-clamped	$x_f=23$	2835	2858	-0.81	721
			9188	9176	0.13	1206
		$x_f=27$	9186	9136	0.54	1390
			29769	29712	0.00019	2016

3.5 Experimental validations

In this section, we present some experimental results to further validate the accuracy of the present semi-analytical model as well as the loss of ABH effect uncovered by numerical analyses. The beam is made of steel with a mass density of 7794 kg/m^3 and Young modulus of 200 Gpa. The whole beam has a uniform width of 1 cm. The ABH portion parameters of the beam are: $\varepsilon=0.00125$ cm^{-1} and $m=2$. Other parameters are: $x_0=4$ cm, $x_{b1}=16$ cm, $x_{b2}=32$ cm.

As shown in Fig. 3.12, the beam was supported by two thin strings to simulate free boundary conditions, thus eliminating the effect of boundary supports. The beam

was excited using a broadband electromagnetic shaker at x_f=26 cm, with the force measured through a Bruel and Kjaer force transducer (series 8200) and amplified by a Bruel and Kjaer charge amplifier (series 2635). The Polytec scanning vibrometer (PSV) was used to generate a periodic chirp signal with frequency from 0 Hz to 16 kHz to the shaker via a Bruel and Kjaer power amplifier (series 2706). The response velocity of each point in the beam was scanned by the PSV and post-processed by Fourier average.
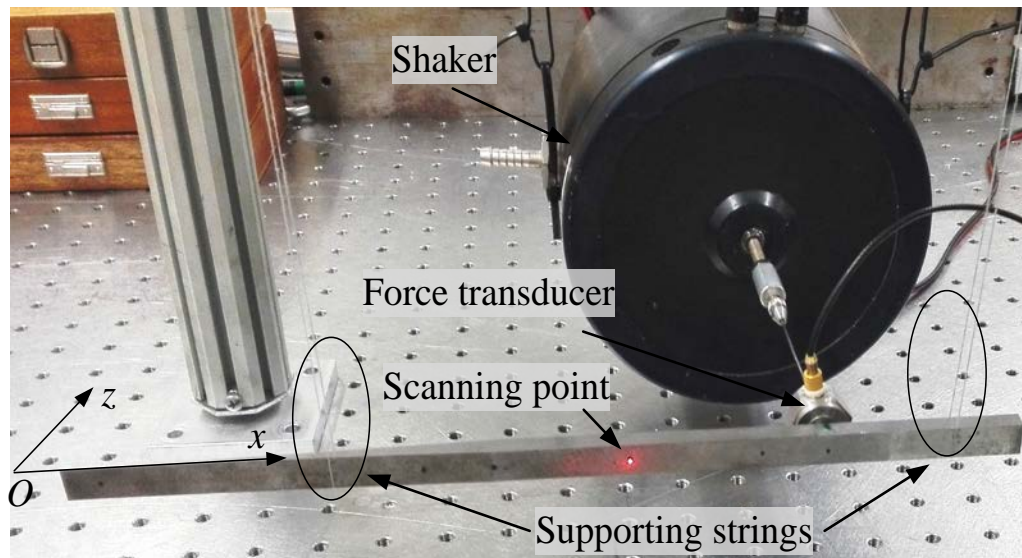
Fig. 3.12 Experimental set-up. A beam with a left ABH part and a right uniform part was hung by two thin strings and excited by a periodic chirp signal from an electromagnetic shaker; the force was measured by a force transducer and amplified by a charge amplifier; a Polytec scanning laser vibrometer was used to scan the beam and measure its vibration response.

The predicted cross-point mobility ($\dot{w}(x_m)/f(x_f)$) calculated by the present

model is compared with the experimental result in Fig. 3.13. The predicted resonant frequencies and anti-resonant frequencies agree very well with that of experiment for the first eight modes with error less than 2%. The increasing error in relatively higher frequencies is likely coming from the omission of the shear and torsional deformation caused by deviation of the excited force from the center axis and the working accuracy of the force transducer at higher frequencies. The predicted amplitude of the cross point mobility is also acceptable compared with the experimental measurements, where the main error is due to the difficulty in determining the accurate loss factor in the experiments. Fig. 3.14 (a) and (b) show the predicted vibration level of the uniform part and that of the ABH part respectively against the experimental results. Both the predicted resonant frequencies and amplitudes are in good agreement with the experimental measurements. Fig. 3.14(c) shows the ratio of the mean quadratic velocity of the ABH part to that of the uniform beam part. As can be seen, the predicted failure of ABH effect agrees well with the experiments results with Γ being negative at most frequencies.
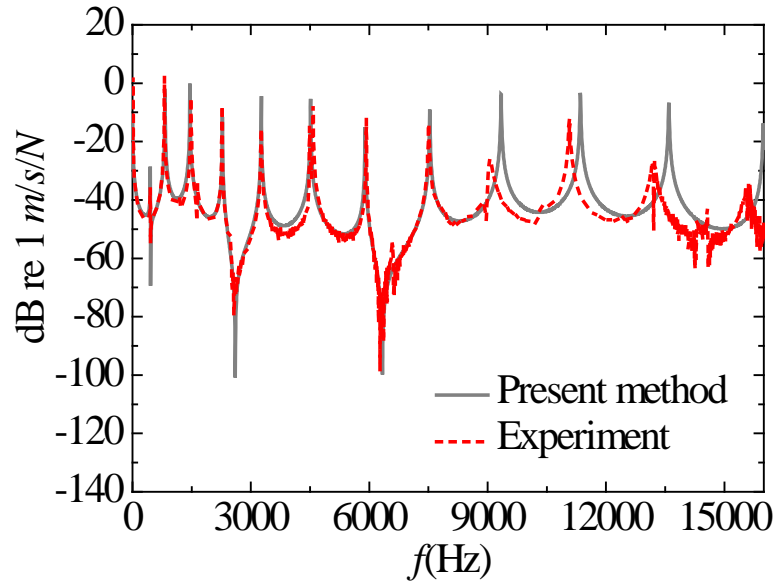
Fig. 3.13 Comparison of the predicted cross point mobility, $\dot{w}(x_m = 5\mathrm{cm}) / f(x_f)$, against experimental measurements.

Furthermore, the predicted displacement distribution in Fig.3.11 is also validated by the experimental results, as shown in Fig. 3.15. The highly consistent results show that the vibration level of the ABH part at the two bottommost frequencies is negligible compared with that of the uniform part, which indicates a loss of the ABH effect. Therefore, the present semi-analytical model does provide correct prediction and sufficient accuracy after being compared with the experimental results. Meanwhile, the disappearance of the ABH effect in a finite beam does exist and should be avoided for the targeted frequency ranges in the ABH applications.
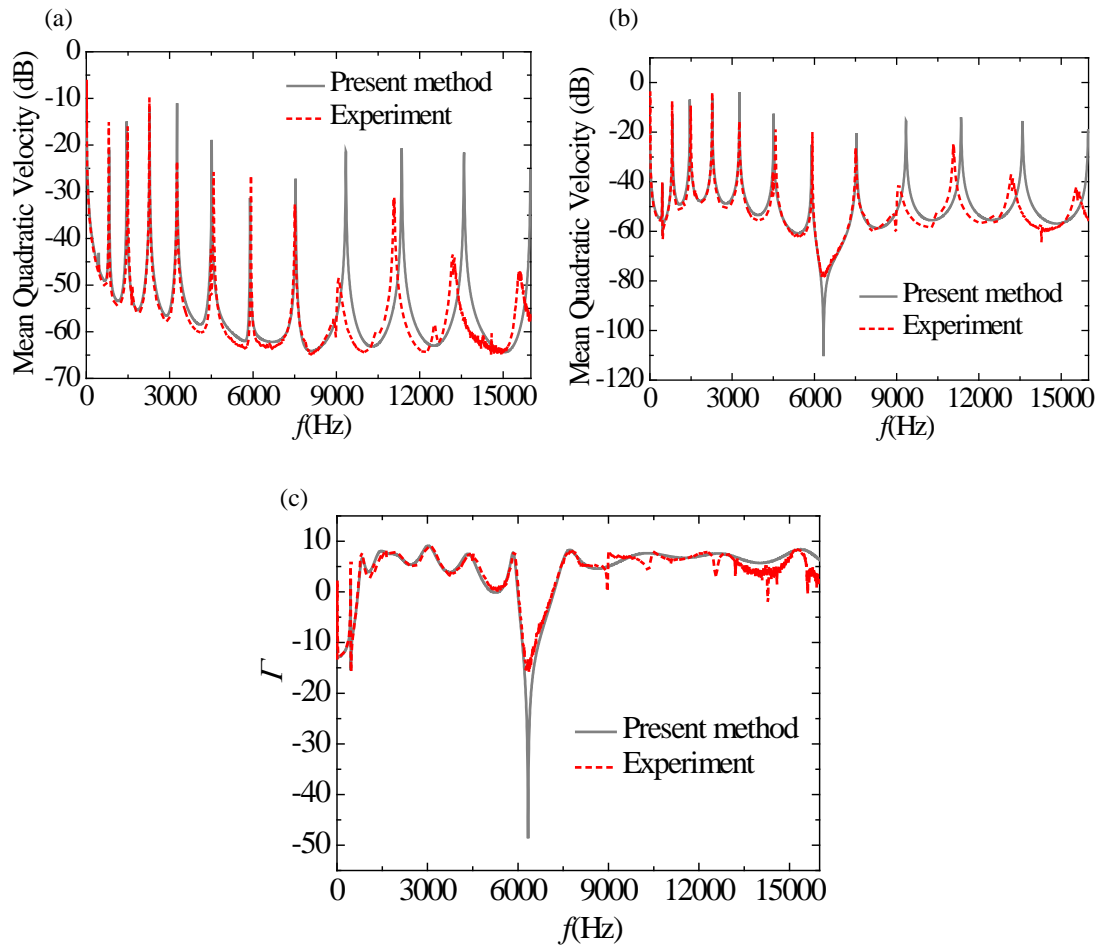
Fig. 3.14 Comparison of the prediction mean quadratic velocity of (a) the uniform

beam portion, and (b) the ABH portion against experimental measurements.
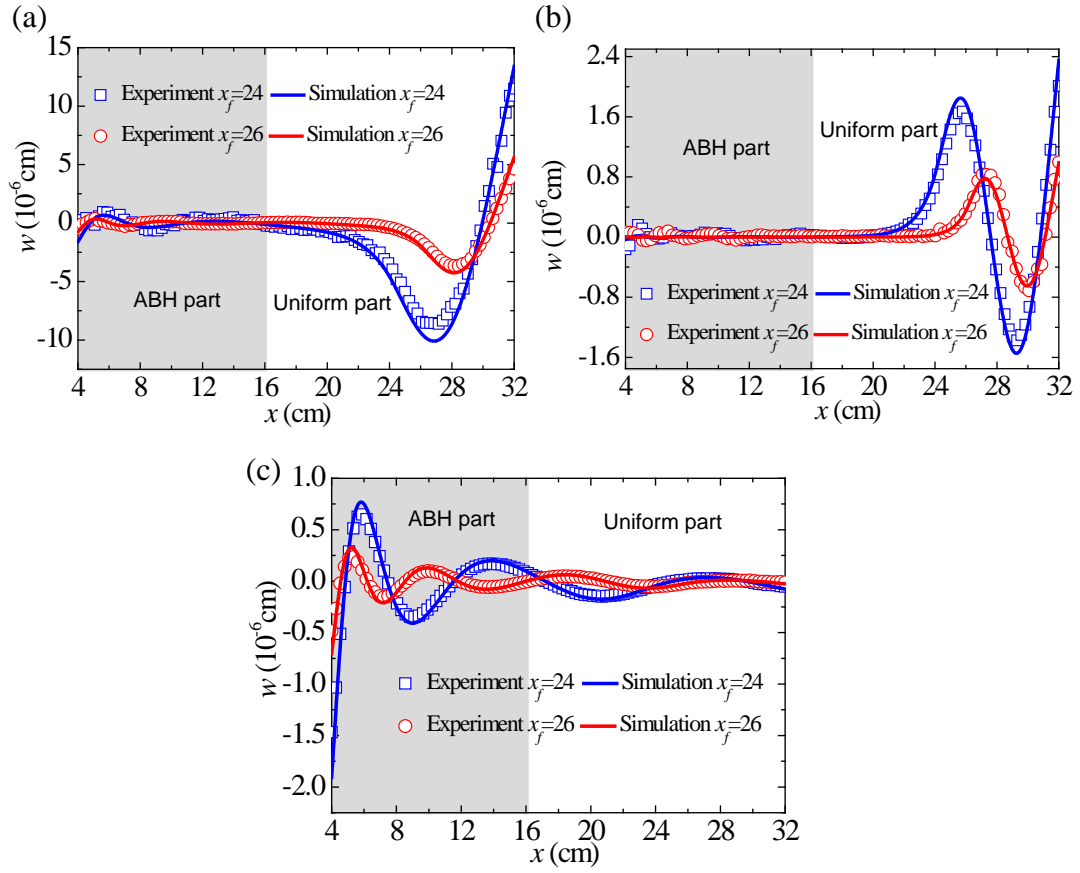
Fig. 3.15 The experimentally measured and numerically predicted displacement distribution along the beam at (a) the first bottommost frequency and (b) the second bottommost frequency of the energy ratio Γ where the ABH effect fails, and (c) the frequencies outside and adjacent to the first failure bands (f =3220 Hz and 5840 Hz), with the force applied at x_f = 24 cm and x_f = 26 cm, respectively.

3.6 Short summary

The proposed wavelet-decomposed and energy-based model provides an efficient way to study the ABH feature and the effect of damping layers using a more

realistic ABH-featured beam. The ABH effect enables a high energy density concentration in the vicinity of the ABH wedge tip, which is conducive to energy control and utilization within a confined area. However, the thickness truncation adversely weakens the ABH effect. Covering the ABH part with damping layers can compensate for the adverse effect of truncation and thus reduce the mean quadratic velocity of the uniform portion of the beam at high frequencies. Damping layers are preferable to be applied near the wedge tip as frequency increases. For a given problem, an optimization using the proposed model is possible to find the exact damping layer configuration to achieve the maximum damping effect. Numerical results also indicate that the stiffness of the damping layers plays a more important role than the mass does, which should be apprehended in the model; while the effect of the added mass also needs particular attention when the thickness of damping layers is considerable to that of the ABH wedge around the tip area. As a general rule, the full coupling between the add-on elements such as the damping layers and the host structure is important to consider, which shows the importance of a fully coupled model.

Meanwhile, the developed model predicts a loss of the ABH effect in a beam of finite size, which up to now has been reported as a broadband phenomenon above the cut-on frequency in semi-infinite ABH structures. The loss of the ABH effect features a significantly impaired energy focalization capability in the tapered ABH region. The width of the failure band can be quite substantial. When this happens, the

vibration energy mainly concentrates within the uniform part of the beam delimited by the excitation force, thus neutralizing the expected ABH effect. Physically, the presence of the shaker, or mechanical excitation, introduces a discontinuity in the local structural impedance to the waves. At certain frequencies (within the failure frequency bands), multiple wave reflections take place between the structure boundary and the excitation point, forming standing waves and local resonances, thus triggering the localization effect. The failure frequencies can be predicted by calculating the local resonance frequencies of the beam portion delimited and pinned by the excitation point, which allows the avoidance of the phenomenon in the targeted application ranges.

As a final remark, the model also guarantees high accuracy with highly consistent results compared with the numerical and experimental results in terms of the resonant frequencies and vibration amplitude as well as the distribution.

Chapter 4 Imperfect ABH and Methods to Enhance ABH Effect

ABH effect shows appealing potential for passive vibration control [12, 18, 21, 22, 32], sound radiation control [26, 27] and energy harvesting [29, 30] due to the high energy concentration within a confined area. However, manufacturing an ideally tailored power-law thickness profile of a structure with embedded ABH feature can hardly be achieved in practice. Past research showed that the inevitable truncation at the wedge tip of the structure resulting from the manufacturing can significantly weaken the expected ABH effect by creating wave reflections [12]. To maximize the ABH effect, however, the ultimate pursuit of extremely thin wedge tips incurs high cost and poses harsh demand for the precision machining and would also lead to tip damage such as tearing. Although Bowyer et al [20] experimentally showed that the damage on the wedge tip does not notably affect the ABH effect; Denis et al [36] reported that the imperfect wedge tip would reduce the reflection because of the resultant scattering effects; structures with ultra-thin or damaged tips however can hardly be applied in industry due to the structural strength problems. Therefore, on the premise of the minimum achievable truncation thickness by currently available manufacturing technology, ways to maximize the ABH effect need to be explored.

Motivated by this, Bayod [37] proposed a modified thin wedge with extended constant thickness to achieve better vibration damping compared with conventional

wedge. Experiments and FEM analyses were carried out to confirm this concept. Probably due to the lack of simulation tools, however, no deep explanation and parametric studies were provided in that work to guide the design of the modified wedge. Meanwhile various modified wedge thickness profiles were also proposed [15, 30, 43]. Although similar ABH effect as the conventional profile was observed, the effect of various parameters defining the modified profiles still needs to be systematically analyzed and quantified. On the other hand, nearly all the references mentioned above focused on the ABH effect at relatively higher frequencies. Possible extension of the ABH effect to lower frequencies is still a great challenge and is of particular importance for applications in energy harvesting and noise control. It is understandable that none of the above could be done without a reliable and flexible simulation tool.

In this chapter, we focus on seeking ways to achieve better ABH effect on the premise of the minimum achievable truncation thickness and the possibility of applying ABH effect at low frequencies. Firstly, an Euler-Bernoulli beam, with modified thickness profile, $h(x) = \varepsilon(x - x_0)^m + h_0$ and an extended platform, is studied using the previously developed wavelet-decomposed model (Sec. 4.1). Then, the effect of the additional thickness h_0 and the extended platform is systematically discussed through numerical simulations (Sec. 4.2). Particularly, we investigate the effect of the profile parameters on the average system loss factor for different additional thicknesses and lengths of extended platform. A particular focus is also put

on exploring the beneficial effect of the extended platform in the low frequency range. Much of the work presented in this chapter has been published in [67].

4.1 Modelling of the system

We consider an Euler-Bernoulli beam composed of a uniform portion with a constant thickness h_b and an ABH portion, same as that shown in Fig. 2.1. The difference is that the ABH part now follows a modified thickness profile, defined as $h(x) = \varepsilon(x - x_0)^m + h_0$, from x_0 to x_{b1} (Fig. 4.1). When x_0 and h_0 are both equal to zero, it retreats to the conventional power-law thickness profile, $i.e.\ h(x) = \varepsilon x^m$. Meanwhile, the tip portion is extended to form a platform with a uniform thickness $h(x_0)$ from the truncation point x_0 to x_{ext}. The covered damping layers with a variable thickness $h_d(x)$ from x_{d1} and x_{d2} can be either on the ABH profile or on the extended platform. The whole system is symmetrical with respect the mid-line of the beam. The extended platform end of the beam is free and the other end is elastically supported by artificial translational and rotational springs as shown in Fig. 2.1, the stiffness of which can be adjusted to achieve various boundary conditions. The damping of both the beam and the damping layer are taken into account through complex stiffness E, $i.e.$, $E = E(1+i\eta)$, where η is the damping loss factor, assigned differently to the beam and the damping layer. The previously developed wavelet-decomposed method based on Lagrange's equation is used to obtain the vibration response.

70

damping layer
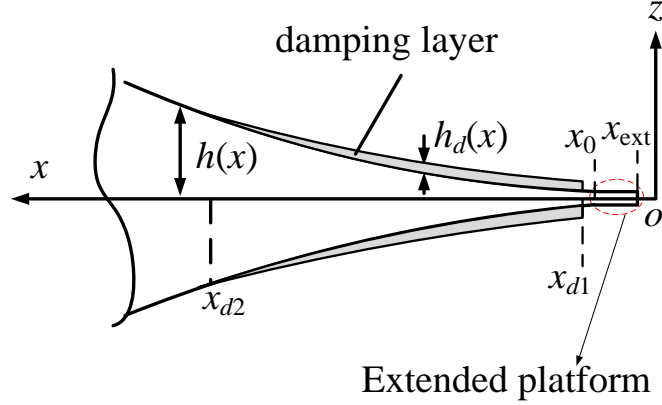
Fig. 4.1 The ABH part with symmetrical modified power-law profile and extended platform.

Decomposing the flexural displacement of the whole beam by MHW functions to obtain the Lagrangian of the system, and then submitting the Lagrangian into the Lagrange's equations, we can finally get and solve the forced and free vibration equations, similar to Eqs. (2.11) and (2.12). The detailed procedure can be referred to Chapter 2.1. Note that the kinetic and potential energies of the extended platform should also be included in the whole system. Accordingly, Eqs. (2.28) and (2,29) are re-expressed as

$$E_k = E_k^{\text{beam\_ABH}} + E_k^{\text{beam\_Uni}} + E_k^{\text{damp}} + E_k^{\text{ABH\_extend}} \tag{4.1}$$

$$E_p = E_p^{\text{beam\_ABH}} + E_p^{\text{beam\_Uni}} + E_p^{\text{damp}} + E_p^{\text{edge}} + E_p^{\text{ABH-extend}} \tag{4.2}$$

where

$$E_k^{\text{ABH\_extend}} = \rho_b h(x_0) \int_{x_{\text{ext}}}^{x_0} \sum_i \sum_s \sum_p \sum_r \dot{a}_{i,s}(t) \dot{a}_{p,r}(t) \varphi_{i,s}(x) \varphi_{p,r}(x) \mathrm{d}x$$

$$E_p^{\text{ABH\_extend}} = \frac{E_b h(x_0)^3}{3} \int_{x_{\text{ext}}}^{x_0} \sum_i \sum_s \sum_p \sum_r a_{i,s}(t) a_{p,r}(t) \frac{\partial^2 \varphi_{i,s}(x)}{\partial x^2} \frac{\partial^2 \varphi_{p,r}(x)}{\partial x^2} \mathrm{d}x$$

71

Meanwhile, considering the modified thickness profile and the additional coverage of damping layers over the extended platform, the kinetic and potential energies from the ABH part and the damping layers should also be considered as

$$E_k^{\text{beam\_ABH}} = \rho_b \int_{x_0}^{x_{b1}} \sum_i \sum_s \sum_p \sum_r \dot{a}_{i,s}(t) \dot{a}_{p,r}(t) \varphi_{i,s}(x) \varphi_{p,r}(x) h(x) \mathrm{d}x \qquad (4.3)$$

$$E_p^{\text{beam\_ABH}} = \frac{E_b}{3} \int_{x_0}^{x_{b1}} \sum_i \sum_s \sum_p \sum_r a_{i,s}(t) a_{p,r}(t) \frac{\partial^2 \varphi_{i,s}(x)}{\partial x^2} \frac{\partial^2 \varphi_{p,r}(x)}{\partial x^2} h(x)^3 \mathrm{d}x \qquad (4.4)$$

$$E_k^{\text{damp}} = \rho_d \int_{x_{d1}}^{x_{d2}} \sum_i \sum_s \sum_p \sum_r \dot{a}_{i,s}(t) \dot{a}_{p,r}(t) \varphi_{i,s}(x) \varphi_{p,r}(x) h_d(x) \mathrm{d}x \qquad (4.5)$$

$$E_p^{\text{damp}} = \frac{E_d}{3} \int_{x_{d1}}^{x_0} \sum_i \sum_s \sum_p \sum_r a_{i,s}(t) a_{p,r}(t) \frac{\partial^2 \varphi_{i,s}(x)}{\partial x^2} \frac{\partial^2 \varphi_{p,r}(x)}{\partial x^2} \left\{ [h(x_0) + h_d(x)]^3 - h(x_0)^3 \right\} \mathrm{d}x$$

$$+ \frac{E_d}{3} \int_{x_0}^{x_{d2}} \sum_i \sum_s \sum_p \sum_r a_{i,s}(t) a_{p,r}(t) \frac{\partial^2 \varphi_{i,s}(x)}{\partial x^2} \frac{\partial^2 \varphi_{p,r}(x)}{\partial x^2} \left\{ [h(x) + h_d(x)]^3 - h(x)^3 \right\} \mathrm{d}x$$

$$(4.6)$$

Then, the components in the mass matrix and stiffness matrix in Eq. (2.11) can be rewritten as

$$M_{ipsr} = M_{ipsr}^{\text{beam\_Uni}} + M_{ipsr}^{\text{beam\_ABH}} + M_{ipsr}^{\text{damp}} + M_{ipsr}^{\text{ABH\_extend}} \qquad (4.7)$$

$$K_{ipsr} = K_{ipsr}^{\text{beam\_Uni}} + K_{ipsr}^{\text{beam\_ABH}} + K_{ipsr}^{\text{damp}} + K_{ipsr}^{\text{edge}} + K_{ipsr}^{\text{ABH\_extend}} \qquad (4.8)$$

where

$$M_{ipsr}^{\text{beam\_ABH}} = 2\rho_b \int_{x_0}^{x_{b1}} \varphi_{i,s}(x) \varphi_{p,r}(x) h(x) \mathrm{d}x$$

$$M_{ispr}^{\text{damp}} = 2\rho_d \int_{x_{d1}}^{x_{d2}} \varphi_{i,s}(x) \varphi_{p,r}(x) h_d(x) \mathrm{d}x$$

$$M_{ipsr}^{\text{ABH\_extend}} = 2\rho_b h(x_0) \int_{x_{\text{ext}}}^{x_0} \varphi_{i,s}(x) \varphi_{p,r}(x) \mathrm{d}x$$

$$K_{ispr}^{\text{beam\_ABH}} = \frac{2E_b}{3} \int_{x_0}^{x_{b1}} \frac{\partial^2 \varphi_{i,s}(x)}{\partial x^2} \frac{\partial^2 \varphi_{p,r}(x)}{\partial x^2} h^3(x) \mathrm{d}x$$

$$K_{ispr}{}^{\text{damp}} = \frac{2E_d}{3}\int_{x_{d1}}^{x_0}\frac{\partial^2\varphi_{i,s}(x)}{\partial x^2}\frac{\partial^2\varphi_{p,r}(x)}{\partial x^2}\left\{\left[h(x_0)+h_d(x)\right]^3 - h(x_0)^3\right\}\mathrm{d}x$$

$$+ \frac{2E_d}{3}\int_{x_0}^{x_{d2}}\frac{\partial^2\varphi_{i,s}(x)}{\partial x^2}\frac{\partial^2\varphi_{p,r}(x)}{\partial x^2}\left\{\left[h(x)+h_d(x)\right]^3 - h(x)^3\right\}\mathrm{d}x$$

$$K_{ispr}{}^{\text{ABH\_extend}} = \frac{2E_b h^3(x_0)}{3}\int_{x_{\text{ext}}}^{x_0}\frac{\partial^2\varphi_{i,s}(x)}{\partial x^2}\frac{\partial^2\varphi_{p,r}(x)}{\partial x^2}\mathrm{d}x$$

The rest of the components in the mass matrix and stiffness matrix and the force vector remain the same as Eqs. (2.32), (2.36), (2.39) and (2.40).

4.2 Numerical results and discussions

Consider two clamped-free beams with the same uniform portion under a harmonic driving force of 1N applied at the point, 3 cm away from the clamped end (as shown in Fig. 4.1). Keep the same truncation thickness $h(x_0)$ and profile parameters ε and m, the responses of the two beams are first analyzed and compared. Case 1 involves a conventional ABH thickness profile ($h_1(x)=\varepsilon x^m$) and case 2 a modified thickness profile ($h_2(x)=\varepsilon(x-x_0)^m+h_0$). The material and geometrical parameters are listed in Table 4.1. Note that truncated at x_0=4 cm, the prescribed truncation thickness $h(x_0)$, 0.02cm, is the same in both cases. As a benchmark system, an entirely uniform beam with the same thickness and length as case 1 is also given as a reference in the following analyses.

Table 4.1

Material and geometrical parameters.

Material parameters	Geometrical parameters
Beam	
$E_b = 210$ GPa	$\varepsilon = 0.00125$
$\rho_b = 7800$ kg/m^3	$m = 2$
$\eta_b = 0.001$	$x_0 = 4$
Damping layers	$h_0 = 0.02$ cm
$E_d = 5$ GPa	$h_b = 0.32$ cm
$\rho_d = 950$ kg/m^3	$h(x_0) = 0.02$ cm
$\eta_d = 0.1$	$l_{Uni} = x_{b2} - x_{b1} = 12$ cm

It should be noted that, in order to keep the same truncated thickness and the same uniform beam thickness, the effective length of the ABH part is different in cases 1 and 2. However, we start from the assumption that the ABH structure is usually used as an add-on part to the existing structure (which is the uniform beam in this particular case). In this context, we would accept a slightly different ABH length as long as the results remain comparable. In the following analyses, within the range we used for ε, m and other parameters, the difference in the ABH length is not very large, especially for cases of our interest when m is large and truncation thickness is small. Meanwhile, we make sure that the cases shown in each figure are comparable by ensuring that the same damping layers are applied in all cases, starting from the

free end with exactly the same thickness and length. The latter is taken as the shortest

ABH length if different ABH profiles are involved in figures where comparisons are

made.

4.2.1 Effect of the modified thickness profile

Since tip truncation is inevitable, we will first investigate the possibility of

changing the thickness profile, aiming at achieving better ABH effect than the

conventional ABH profile with the same truncation. Keeping the same truncation tips

with the same minimum achievable thickness $h(x_0)$, the modified thickness profile

(case 2) is different from the conventional ABH thickness profile (case 1) in that it

possesses an additional thickness term h_0. We first investigate the effect of this

additional thickness term on the ABH effect without the consideration of the

extended platform.

Figure 4.2 shows the mean quadratic velocity of the uniform beam portion and

the mean quadratic velocity ratio Γ ($\Gamma = 10\log\dfrac{<V^2>_{\text{ABH}}}{<V^2>_{\text{Unif}}}$) between the ABH

portion and the uniform portion for three different beams without damping layers. It

can be seen that the overall vibration level of the uniform portion of both beams with

the conventional and modified ABH profiles are slightly lower at higher frequencies

compared with their uniform counterpart as a result of ABH effect. However, due to

the existence of the truncation, flexural waves are reflected back in the absence of the

damping layers, which explains the barely noticeable reduction in the vibration level. Meanwhile, the modified thickness profile takes better ABH effect than the conventional profile by slightly reducing the vibration level at higher frequencies as shown in Fig. 4.2 (a). This can be further confirmed in the Fig. 4.2(b) which shows a clear vibration energy shift to the ABH portion, in case 2 more than in case 1.

Since the damping layers take the upmost effect near the truncation tip as shown in chapter 3. Fig. 4.3 compares the system loss factors for the same three beam cases when same length of damping layers applied. Compared with the entirely uniform beam, while the system loss factor in case 1 with conventional ABH profile being significantly increased at higher frequencies due to the ABH effect, that of case 2 with the modified profile is nearly doubled. Meanwhile, different from case 1, the lower-order modal loss factor in case 2 also attains noticeable increase. Thus, the overall reduction in the vibration level of the uniform portion in case 2 is also larger than that in case 1, in comparison with the entirely uniform beam as revealed in Fig. 4.4, reaching a level as high as 19.2 dB.

(a)

(b)

Fig. 4.2. (a) The mean quadratic velocity of the uniform beam portion, and (b) the ratio of the mean quadratic velocity of the ABH portion to the uniform beam portion for three different beam cases without damping layers.
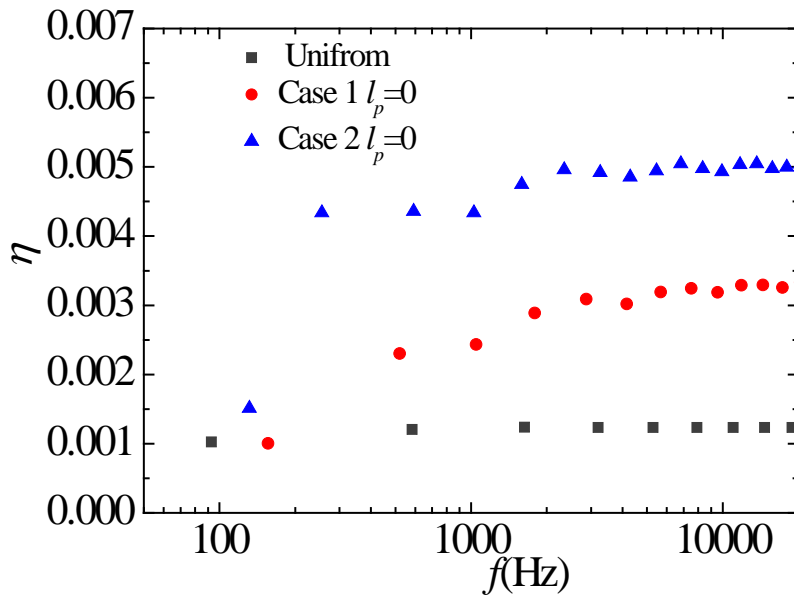
Fig. 4.3 The system loss factors for three different beam cases with same length of damping layers.

Fig. 4.4 (a) The mean quadratic velocity of the uniform beam portion, and (b) the ratio of the mean quadratic velocity of the ABH portion to the uniform beam portion for three different beam cases with same length of damping layers.

Two plausible reasons could explain the reason why the modified thickness profile with an additional thickness h_0 outperforms the conventional ABH profile for the same given thickness truncation. The mode shapes of the entire beam for the two cases are shown and compared in Fig. 4.5. It can be seen that case 2 with modified profile promotes larger structural deformation at the ABH portion for both the first and one representative higher-order (tenth) mode shape. This enables more energy concentration on the ABH portion, conducive to energy absorption by the damping layers. From the perspective of the geometrical acoustic theory, the total wave reflection coefficient R_0 can be expressed as $R_0 = \exp(-2\int_{x_0}^{x} \mathrm{Im}\, k(x)\mathrm{d}x)$ [12], in which the local wavenumber $k(x) = 12^{1/4}(\omega/c_l)^{1/2}h(x)^{-1/2}$ with $c_l = \sqrt{E_b(1+j\eta_b)/\rho_b}$ being the velocity of longitudinal waves. Therefore, R_0 is

78

negatively correlated with the integration term $\int_{x_0}^{x} h(x)^{-1/2}$. The derivatives of the thickness profiles of case 1 and case 2 are respectively $h_1'(x) = \varepsilon m x^{m-1}$ and $h_2'(x) = \varepsilon m (x - x_0)^{m-1}$. It can be seen that $h_1'(x)$ is always larger than $h_2'(x)$. Therefore, given the same starting truncation thickness x_0, the thickness at any point along the beam in case 1 is always larger than that in case 2, i.e. $h_1(x)^{-1/2} < h_2(x)^{-1/2}$. On the other hand, for the same beam thickness $h(x_{b1})$, the corresponding x of case 1 is constantly smaller than that of case 2, i.e. $x_{b1\_1} < x_{b1\_2}$. Consequently, the integration $\int_{x_0}^{x_{b1\_2}} h_2(x)^{-1/2}$ is always larger than $\int_{x_0}^{x_{b1\_1}} h_1(x)^{-1/2}$, resulting in a lower reflection coefficient in case 2 as compared to case 1. This implies better ABH effect achieved by the case 2 for any ε and m as observed above.
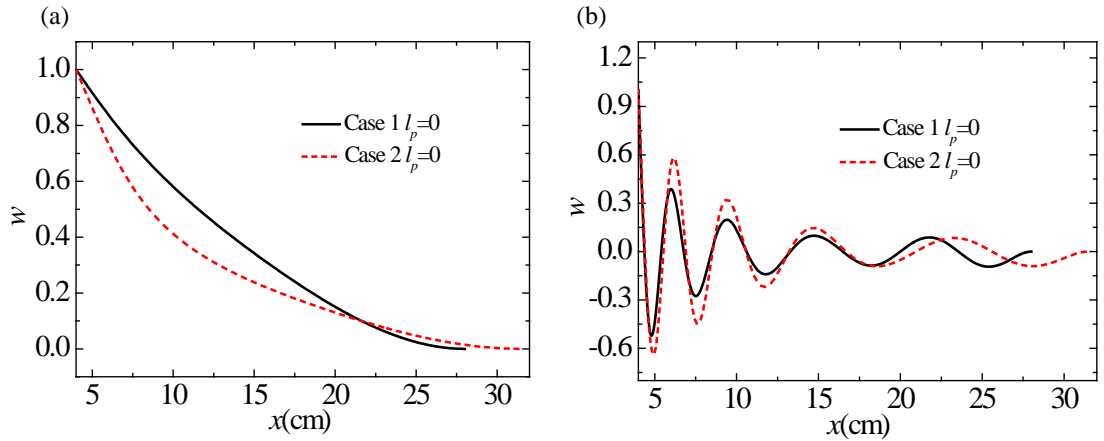
Fig. 4.5 Mode shape comparison for two cases: (a) first mode; (b) tenth mode.

To quantify the broadband ABH feature of the modified profile, the average system loss factor is used and applied to both thickness profiles cases. The band is defined starting from a characteristic frequency f_{cha}, at which corresponding

wavelength λ of the incoming wave approaches and starts to be shorter than the

characteristic ABH dimension, *i.e.* the length of the ABH part, so that the incoming

wave can interact more effectively with the ABH element. For $\lambda = \dfrac{c_b}{f_{cha}} \leq L_{ABH}$ and

$$c_b = \sqrt[4]{\frac{E_b I \omega^2}{\rho_b A}} = \left[4\pi f h_b \sqrt{\frac{E_b}{12\rho_b}} \right]^{\frac{1}{2}} \quad , \quad \text{we get } f_{cha} = \frac{4\pi h_b}{L^2_{ABH}} \sqrt{\frac{E_b}{12\rho_b}} \; . \quad \text{Then, the increase}$$

in the average system damping loss factor is defined as

$$\overline{\Delta \eta} = \frac{1}{m} \sum_p^{p+m} (\eta_{2p} + \eta_{2(p+1)} + \dots + \eta_{2(p+m)}) - \frac{1}{n} \sum_q^{q+n} (\eta_{1q} + \eta_{1(q+1)} + \dots + \eta_{1(q+n)}) \, , \text{ where the first}$$

subscript of η denotes the case number and the second subscript denotes the mode

number above the characteristic frequency.

Figure 4.6 shows the effect of h_0 (*i.e.* the truncation thickness) on $\overline{\Delta \eta}$ for

different parameters (frequency band chosen as 10000 ~ 50000 Hz). It can be seen

that the increase in the ABH effect by the modified profile is much more noticeable

as h_0 reduces, due to the fact that ABH effect is most effective near the very thin

truncation region. Even a small variation in the thickness profiles with a thinner

truncation thickness would lead to significant difference in the ABH effect. For the

same h_0, steeper profile variation with a larger profile parameter m is certainly

helpful, whilst ε, however, showing negligible effect. Noted that to maintain a

reasonable length comparison of the ABH part for different parameters, the change of

m in Fig. 4.6 is not very large. If further increase in the parameter m is needed, the

resultant increase in the ABH effect will be more obvious. Therefore, for larger

profile parameter *m* and smaller truncation thickness, the modified thickness profile

can greatly increase the ABH effect as compared with the conventional ABH profile

having the same truncated tip thickness.
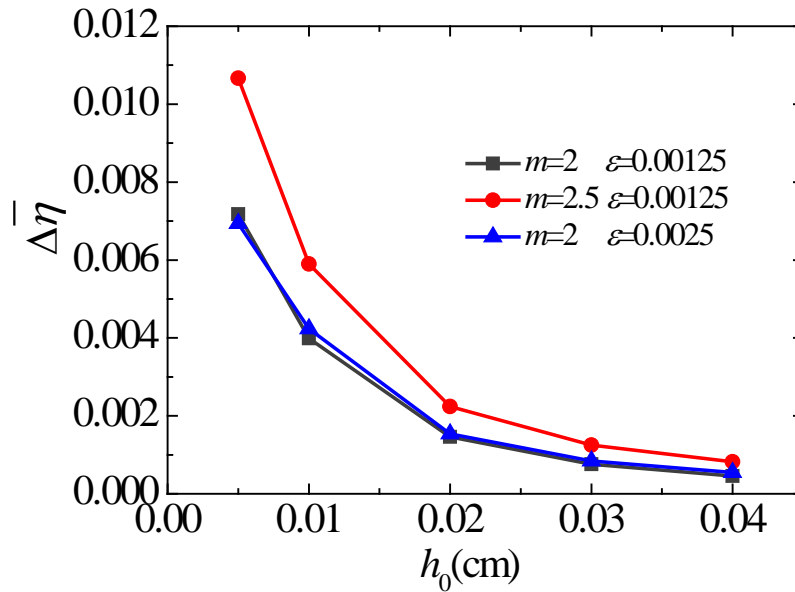
Fig. 4.6 Average increase in system damping loss factor of case 2 compared with

case 1 under different parameters of thickness profile.

4.2.2 Effect of the extended platform

Using both ideal and modified thickness profiles, the truncated tip is extended to

form a platform of constant thickness.   Numerical analyses are performed to explore

the possibility of improving ABH effect at both high and low frequencies using the

extended platform. Figure 4.7 compares the system loss factors for both cases with

and without the platform when ABH portion (extended platforms also considered as

a part of the ABH portion for convenience) is covered by damping layers with same

length. It can be seen that the extended platform, with a length l_p= 4 cm, significantly

increases the system damping at higher frequencies for both thickness profiles. As

defined before, the characteristic frequency ($f_{cha} = \dfrac{4\pi h_b}{L^2_{ABH}}\sqrt{\dfrac{E_b}{12\rho_b}}$) actually shifts to

lower frequencies because the characteristic dimension L_{ABH} of the ABH region is

enlarged by the extended platform, *i. e.* $L_{ABH} = l_{ABH} + l_P$. Taking case 1 as an

example, the characteristic frequency without platform is roughly 2000 Hz, while

that with the platform reduces to about 1100 Hz, as shown in Fig. 4.7.   On the other

hand, compared with the cases without platform, the system loss factor with a

platform also significantly increases below the characteristic frequency. Therefore,

the extended platform allows achieving better broadband ABH effect while providing

the possibility to lower its effective region. Owing to the additional benefit of the

additional thickness h_0 revealed above, the modified thickness profile further

enhances the ABH effect compared with the conventional ABH profile, as

demonstrated in Fig. 4.7.
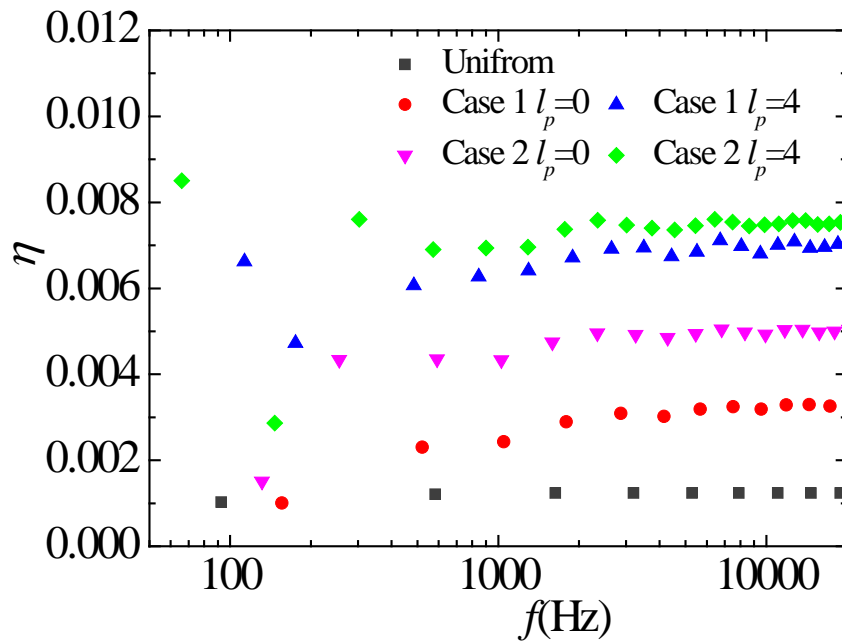
Fig. 4.7 System loss factors for three different beam cases with and without extended platform when damping layers with same length applied.

Focusing on case 2 with the modified thickness profile, Fig. 4.8 shows the vibration level of the uniform part and the energy ratio of the beams with and without platform when damping layers applied. As can be seen from Fig. 4.8 (a), the overall vibration level of the uniform beam portion is reduced with the use of the extended platform, which is systematic at higher frequencies, but more or less at the lower resonant frequencies. It is understandable that the lower frequency alteration in the system damping depends more on the modal characteristics of the system, which certainly deserves a closer examination. In general, however, the platform allows better energy focalization in the ABH part at higher frequencies (Fig. 4.8 (b)).

Meanwhile, the first peak in the energy ratio curves increases significantly while the corresponding frequency shifts to much lower frequency than the case without platform, which implies more effective ABH effect at a lower frequency as well.

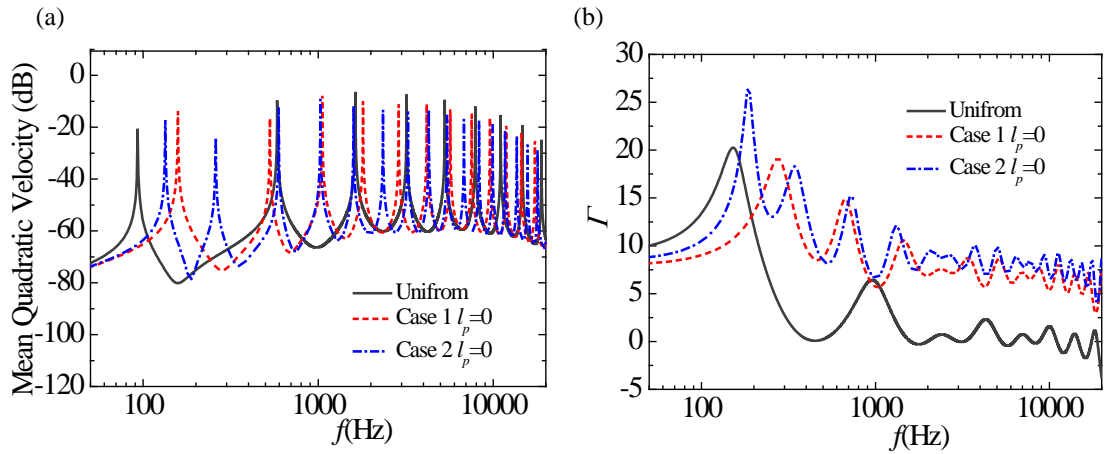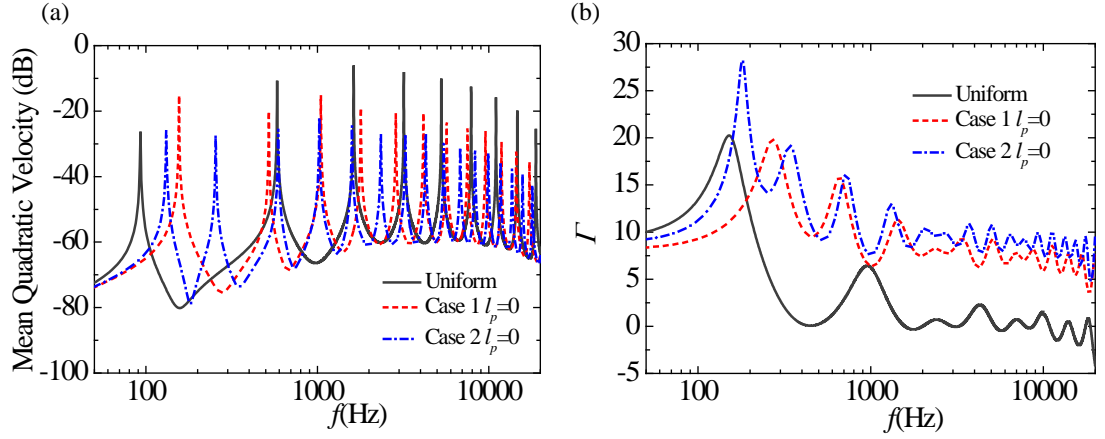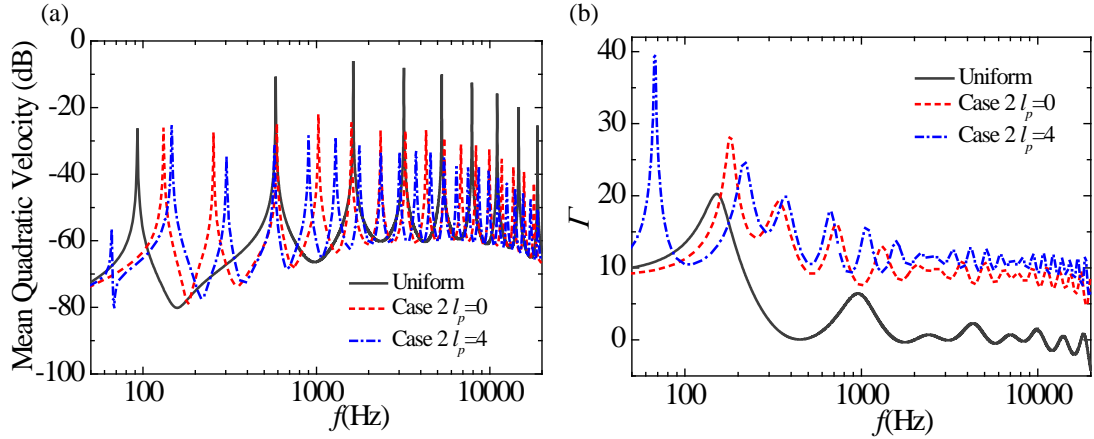Fig. 4.8 (a) Mean quadratic velocity of the uniform beam portion, and (b) ratio of mean quadratic velocity of the ABH portion to the uniform beam portion for case 2 with and without extended platform when damping layers with same length applied.

To further explain the observed phenomena, Fig. 4.9 shows the mode shape with and without the extended platform. Similar to Fig. 4.5, the case with a platform involves more significant structural deformation at the ABH portion than the one without platform at the first mode, allowing better energy concentration in the ABH portion. For higher–order mode (tenth mode as an example), the extended platform prolongs the active area of the ABH by extending the intensive wave packet to the platform area after being compressed by the ABH profile.

Fig. 4.10 shows the effect of the length of the extended platform on the system

loss factor. As the length increases, the system loss factor also increases in a broadband region, not necessarily proportional to the increase in the length of the platform. Below the characteristic frequency, although the damping enhancement is observable, the tendency, however, is less systematic for different lengths of the platform. Nevertheless, the observation that the first system modal loss factors increases and the effective frequency is shifted to lower frequencies with the increasing platform length still holds. Again, the phenomenon strongly depends on the modal behavior of the structure. Therefore, the length of the platform should be properly selected to target particular application frequency range with additional consideration of the system dimension.
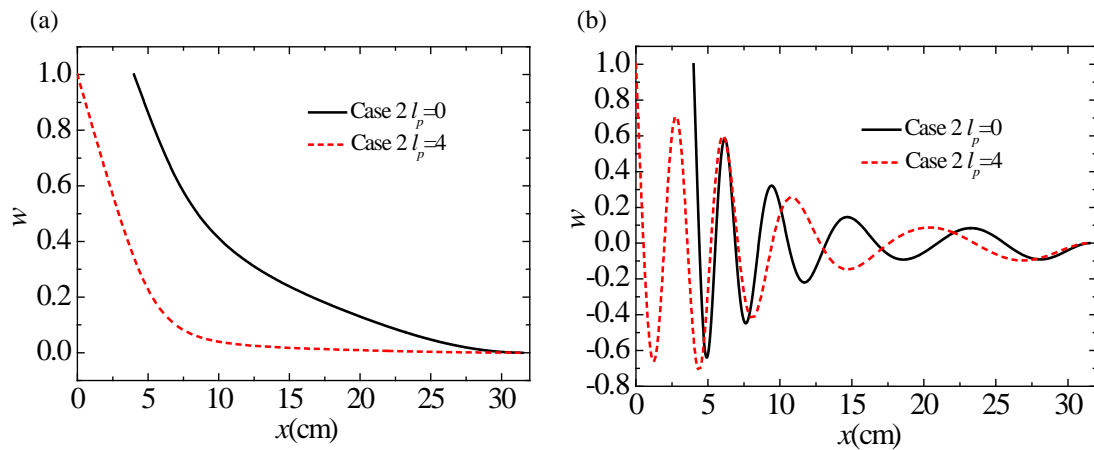
Fig. 4.9 Mode shape comparison for case 2 with and without extended platform: (a) first mode; (b) tenth mode.
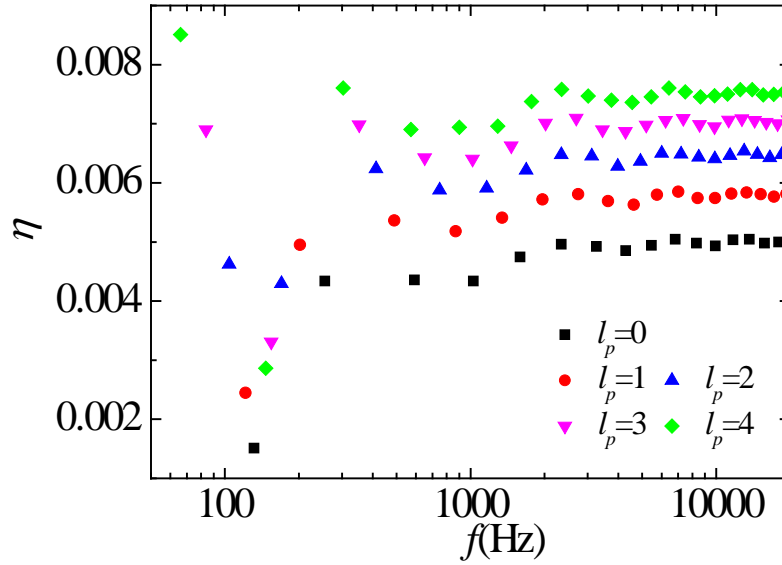
Fig. 4.10 System loss factor for case 2 with different lengths of the extended platform when damping layers with same length applied.

The effect of different thickness profile parameters is revealed in Fig. 4.11, which shows the influences of the length of the extended platform on the average system loss factor for case 2 and the corresponding damping enhancement compared with case 1, respectively. It can be seen that, irrespective of the profile parameters, the average system loss factor systematically increases as the length of platform increases. A larger power parameter m further helps enhancing the effect. The average system loss factor is lower for larger ε and shorter platform, but higher when the platform becomes longer. In terms of damping enhancement in case 2 compared with case 1, $\Delta\bar{\eta}$ also increases with m and ε. The decreasing trend of $\Delta\bar{\eta}$ with the length of the extended platform suggests that, although the damping being enhanced

for both ideal and modified thickness profiles with the use of extended platform, the modified thickness profile, however, allows achieving more significant improvement as compared to the ideal thickness profile for shorter platform. This could be an additional advantage for using modified profile, since an excessively long extended platform may not be feasible in practical applications.
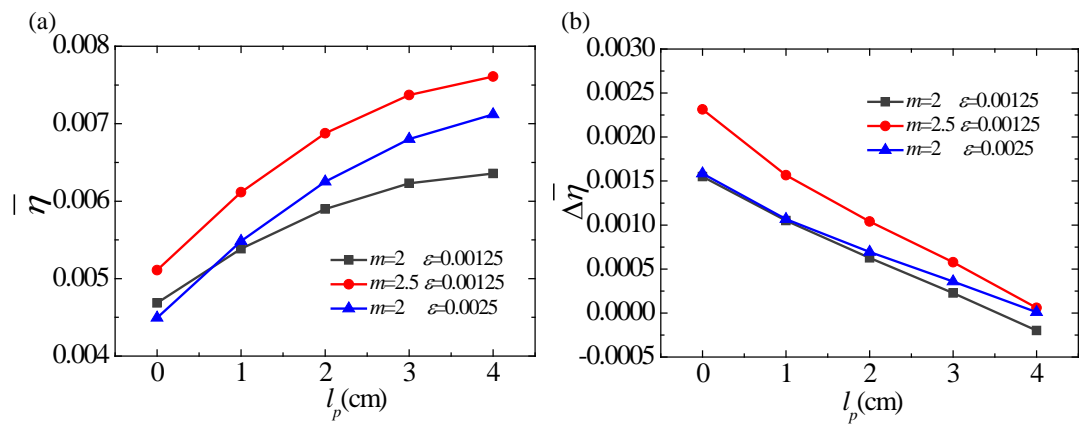
Fig. 4.11 (a) Average system loss factor in case 2 within broadband effective frequency range and (b) Damping increase compared with case 1 when damping layers with same length applied.

To further examine the effect of the extended platform at lower frequencies, the first system modal loss factor (η_1) and the frequency of the first peak f_1 on the energy ratio curve for different platform lengths and profile parameters are plotted in Fig. 4.12. For shorter platform length, η_1 seems to be insensitive to the profile parameters. With the increase in the platform length, however, η_1 rapidly increases before reaching a certain relatively stable level. Meanwhile, larger m and ε are beneficial. Fig. 4.12(b) shows that f_1 is also down-shifted more significantly for

larger *m* and *ε*, which confirms the favorable effect of the extended platform on expanding ABH effect further down to lower frequencies.
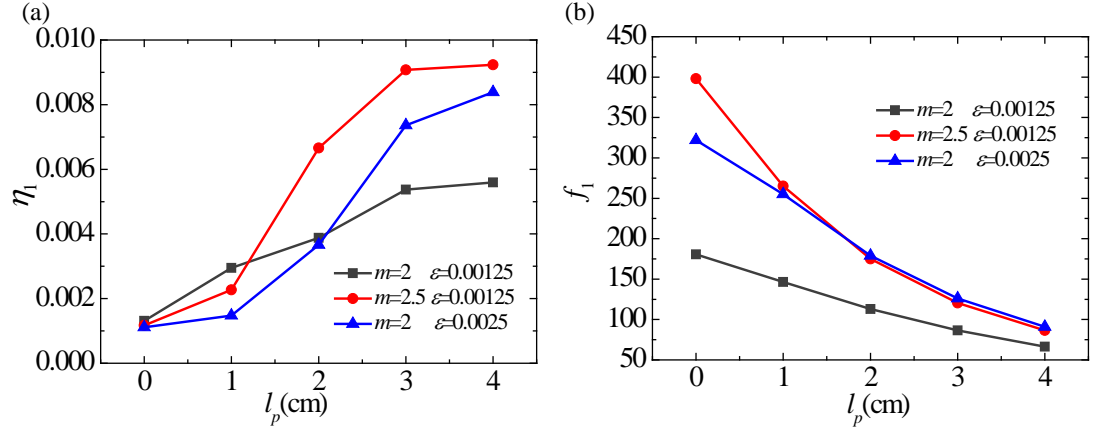
Fig. 4.12. (a) The first system modal loss factor and (b) The frequency of the first peak in the energy ratio curve Γ in case 2 when damping layers with same length applied.

4.3 Short summary

In this chapter, we investigate an Euler-Bernoulli beam with a modified thickness profile and extended platform using the previously developed wavelet-decomposed semi-analytical model based on Lagrange's equation. On the premise of the same minimum achievable truncation thickness, the vibration level of the uniform part of the beam, the energy distribution and the system loss factor with the modified thickness profile are systemically investigated and compared with its counterpart with conventional ABH profile when damping layers are applied. It is

shown that the ABH effect can be significantly enhanced through the use of the modified thickness profile in terms of vibration reduction of the uniform part, energy distribution and the system loss factor. The observed improvement on ABH effect can be explained using the geometrical acoustical theory, which indicates a reduced wave reflection coefficient as a result of the modified thickness profile irrespective of m and ε. The improvement in the ABH effect is more significant with larger power parameter m and smaller truncation thickness, with negligible influence of parameter ε.

The use of an extended platform brings about two positive effects: an enhancement of the overall system damping in a broad frequency band above the cut-on frequency; and an appreciable shift of the ABH effect towards low frequency. For the former, the system loss factors increases with the length of the extended platform, especially with a larger power index m. The effect of parameter ε, however, depends on the length of the extended platform. Therefore, an optimal configuration needs to be worked out in order to find the best combination among different parameters. For the latter, the extended platform can significantly enlarge the first peak of energy ratio and shift it to lower frequency, which provides the possibility of catering ABH effect for lower frequency applications. The tuning of this phenomenon, however, strongly depends on the modal behavior of the whole system, which again requires meticulous analyses using a simulation tool (as the one used in this work) to optimize the ABH performance for particular applications.

In conclusion, for a given truncation thickness, which can possibly be achieved by currently available manufacture technology or prescribed by practical limitation due to the structural strength consideration, an ABH wedge can be profiled and manufactured according the proposed modified thickness profile with an extended platform to prolong the ABH effect. By choosing appropriate parameters such as m, ε and the length of the platform, enhanced ABH effect can be achieved in a broad frequency range, including the possibility of performance tuning at lower frequencies.

Chapter 5 Beams with Multiple ABHs for Vibration Applications

Intensive ABH research has covered various aspects of both 1D and 2D structures in recent years. The effectiveness of using a single ABH element for attenuating bending vibrations has been demonstrated in various theoretical and experimental studies. Semi-infinite 1-D structures have been extensively investigated using models such as the geometrical acoustic approach [7, 12] and the impedance method [18]. These studies reveal insight into the dominant wave propagation phenomena, such as the reduction in the reflection coefficient of flexural waves when the frequency increases. For 1-D structures of finite size, the ABH effect has also been observed both theoretically and experimentally in chapters 2, 3, and 4. Meanwhile, the use of different thickness profiles was also exploited for both 1D [15, 37, 67] and 2D configurations [43].

The major flaw of a single ABH element is that, although ABH effects start to appear above a certain frequency when local ABH dynamics are cut-on, systematic broadband ABH effects can only be achieved above a much higher characteristic frequency as indicated in Chapter 4. Embedding multiple ABHs can, to some extent, improve the low frequency performance without increasing the ABH dimension [45], with applications extended for sound radiation [26]. Existing studies on multiple ABHs [26, 28-30, 45] are mostly based on experiment and the Finite Element

Method. These studies show the ABH effect on wave propagation characteristics. However, the possible accumulated ABH effect and wave filter effect induced by multiple ABHs were not chosen to be the main focus of the discussions. Meanwhile, given limited structural space for ABH part, the performance of the structure with different number and distribution of ABHs remains unknown. It is therefore important to compare this performance with the case containing only one ABH to optimize the design of the number and distribution of ABHs to maximum the ABH effect.

In this Chapter, we first investigate an Euler-Bernoulli beam containing multiple ABHs using the wavelet-decomposed energy method developed in Sec. 5.1. The system loss factors of the cases with single and multiple ABHs under the same length of ABH part are compared. The effects of parameters including the power index m, truncation thickness h_0, platform length l_p and the distribution of ABHs are also studied. Furthermore, special wave filter phenomenon in multiple ABHs structures is analyzed in terms of vibrational energy distributions and transmissions. Then, to illustrate and explain the physical phenomena arising from multiple ABHs, the wavelet-decomposed energy model is expanded to deal with an infinite periodic structure with ABHs in Sec. 5.2. The model is verified and the comparison between infinite and finite structures is made thereafter. Meanwhile, the ABH parameters are analyzed to achieve broader filter gaps. Much of the work has been published in Ref. [68]

5.1 Finite structures with multiple ABHs

5.1.1 Modelling procedure

The wavelet-decomposed model developed in Chapter 2 is used to investigate a structure of finite size with multiple ABHs, as shown in Fig. 5.1. The tapered ABH parts can be covered by thin damping layers. The thickness profile takes the form $h(x) = \varepsilon x^m + h_0$, as shown in Fig. 5.1(b). Artificial translational and rotational springs, of distributed stiffness K and Q, can be adjusted to achieve various boundary conditions. The damping of both the beam and the damping layer is taken into account within the complex Young's modulus E, $i.e.$, $E = E(1+j\eta)$, where η is the damping loss factor, to be assigned different values for the beam and the damping layer. The modelling procedure is almost the same as in Chapter 2, which is omitted here.
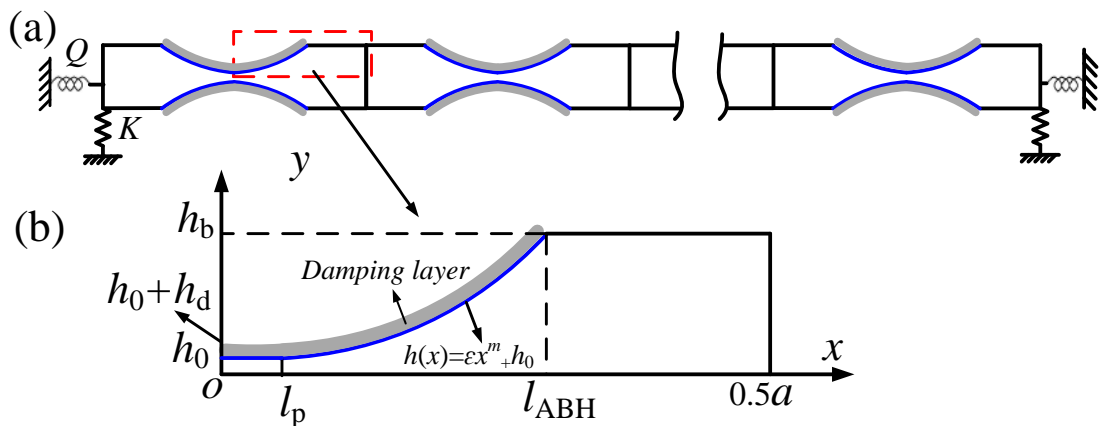
Fig. 5.1 Sketch of (a) an Euler-Bernoulli beam with multiple ABHs and (b) the thickness profile

5.1.2 Performance comparison between single and multiple ABHs

To compare the performance of structures with different numbers of ABHs under the same available space, consider three clamped beams with the same thickness and length, containing one, two, and three ABH elements, respectively. For each beam, the sum length of the ABH profile and extended platform keeps constant as well as the sum of the uniform part and the truncation thickness. The damping layers are applied over the ABH profile and extended platform also keep constant. The material and geometrical parameters are tabulated in Table 5.1.

Table 5.1 Material and geometrical parameters

	Beam	Damping layers
Material parameters	$E_b = 210$ GPa	$E_d = 5$ GPa
	$\rho_b = 7800$ kg/m^3	$\rho_d = 950$ kg/m^3
	$\eta_b = 0.001$	$\eta_d = 0.1$
Geometrical parameters	$h_b = 0.32$ cm	$h_0 = 0.02$ cm
	$h_d = 0.02$ cm	
	Sum($l_{\text{ABH}} + l_{\text{p}}$) = 24 cm	Sum(l_{Uni}) = 24 cm

Without loss of generality, we set the total length of the ABH profile as 16 cm and the extended platform as 8 cm, and compare the system loss factors of the three beams in Fig. 5.2 when the taper power m is 2. For beams with one, two, and three

94

ABH elements, the characteristic frequencies [67] are respectively approximate as 1050Hz, 4200Hz, and 9500Hz. As can be seen, above each characteristic frequency, the system loss factors for the beam itself increase systematically as compared with the bare beam without damping layers and reach to a stable level as expected. As long as three beams all reach their characteristic frequencies, the loss factors show little difference among beams embedded with different ABH elements. This is understandable because above the characteristic frequency, the wavelength is shorter than the characteristic ABH dimension; the wave slows down in ABH profile and can interact more effectively with the ABH element (including both the ABH portion and the extended platform). While in present situation, the whole length of the ABH part remains the same. Therefore, the overall performance at high frequencies is almost the same too. Below the characteristic frequency, the damping enhancement for the beams with different ABH elements is less systematic. However, when increasing the number of ABHs, the first system loss factor can reach a lower frequency with high value. This indicates that increasing the number of ABHs would help to enhance the low frequency performance of the structures with ABHs occupying the same beam length. When m equals to 3, the comparison is also given in Fig. 5.3. The observation is consistent with that with m being 2. Meanwhile, because of the positive role of m on the ABH effect, the overall system damping loss factors are slightly increased.
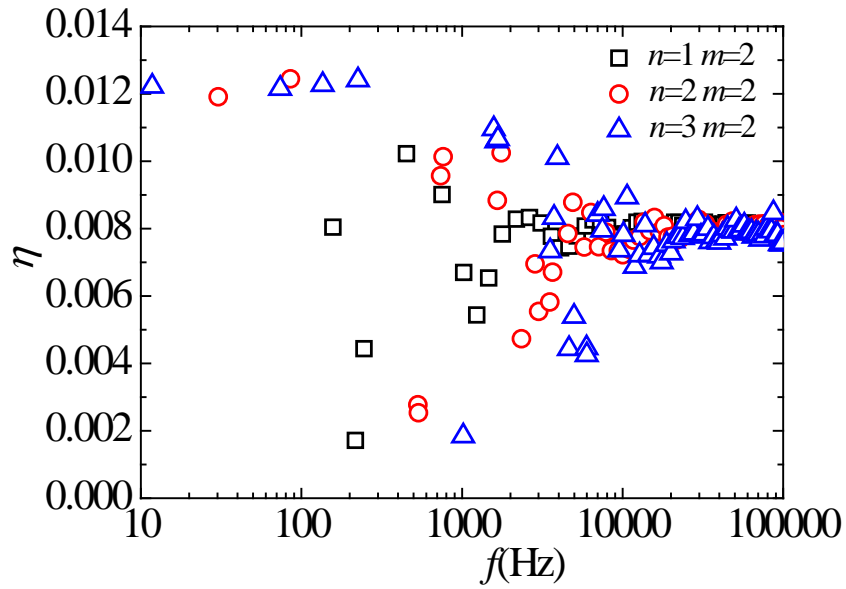
Fig. 5.2 System damping loss factors comparison for different number of ABHs when $m=2$.
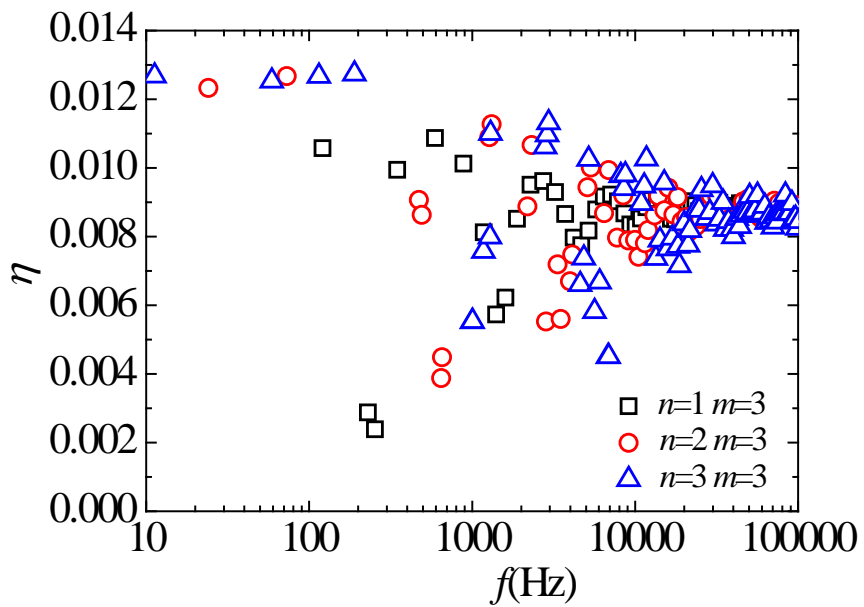
Fig. 5.3 System damping loss factors comparison for different number of ABHs when $m=3$

To further quantify the effect of the number of ABH elements, the system average damping loss factors before and after the characteristic frequency (9500 Hz) for different numbers of ABHs are compared with different truncation thicknesses h_0 in Fig. 5.4. It can be seen that the overall system damping loss factor significantly increases when the truncation thickness of the three beams gets smaller, which is consistent with the observation made in Chapter 3. For a larger m, the average system damping loss factors also increase. More importantly, with a larger number of ABH elements, the average loss factors in the relatively low frequency range (below 9500 Hz) also increase. On the contrary, the average loss factors above 9500 Hz slightly reduce in both cases when m is 2 and 3. Especially, when the truncation thickness is smaller, the corresponding increase of the average loss factors at low frequencies or the decrease at high frequencies is more obvious. The decrease of the average loss factors at high frequencies may result from the fact that although the wavelength is shorter than each characteristic ABH dimension above the characteristic frequency, the concentrated wave energy can be absorbed more effectively in each ABH element with a longer length, which is the case of the beam with fewer ABHs. Therefore, the average loss factor in beams with less ABHs is higher. Meanwhile, since the smaller of the truncation thickness, the more effective of the ABH effect, the resultant difference becomes more obvious for smaller truncation thickness.
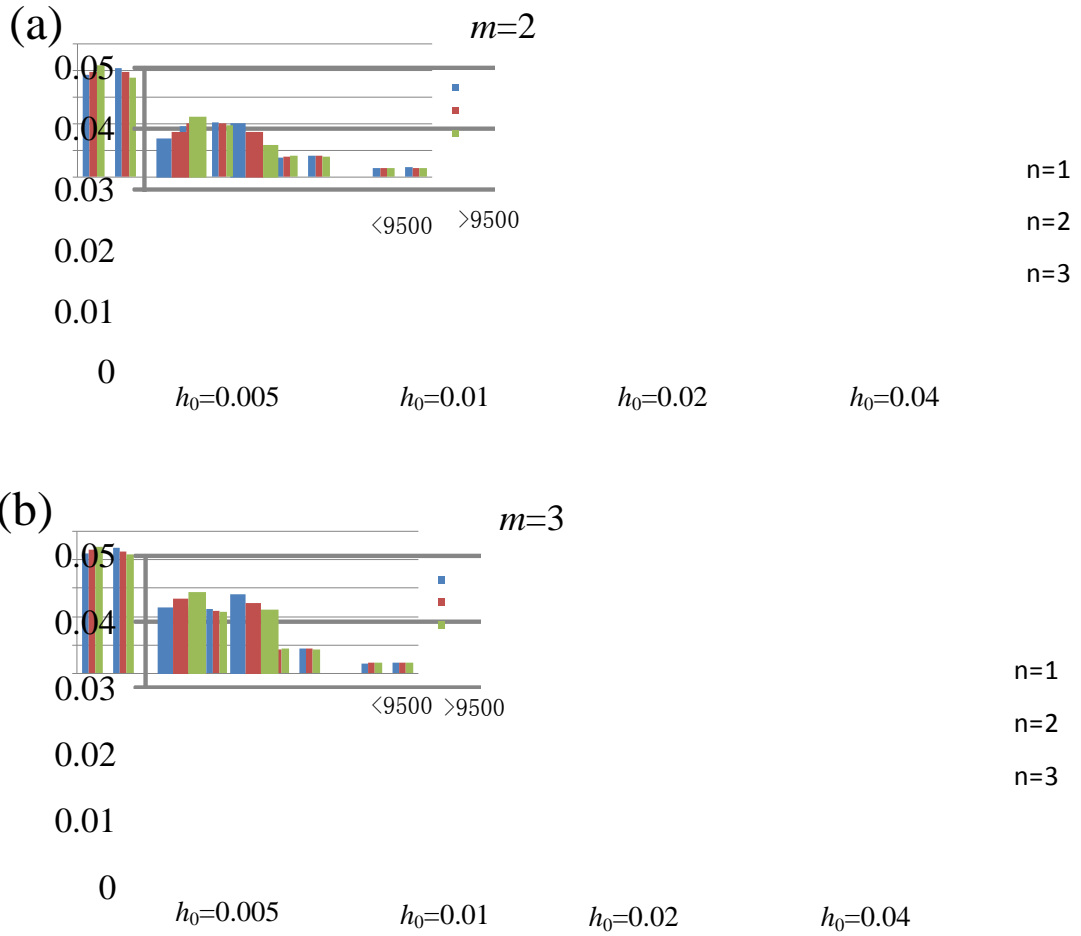
Fig. 5.4 Comparison of the system average damping loss factors before and after the characteristic frequency (9500 Hz) for different number of ABHs under different truncation thickness h_0 : (a) when $m=2$ and (b) when $m=3$.

The effect of the length of the extended platform on the average damping loss factors for different ABHs is also shown in Fig. 5.5. Similar observation can be seen that with more ABHs, the average loss factor reduces above the characteristic frequency while increase below it. As discussed in Chapter 4, increasing the length of the platform would increase the overall loss factors. Meanwhile, due to the same

reason stated above, a longer length of the platform provides more space to dissipate the concentrated wave. Therefore, the difference of the average damping loss factor above the characteristic frequency between different beams with different ABHs is reduced as the length of platform increases. For the average loss factors below the characteristic frequency, the difference seems to be more obvious.
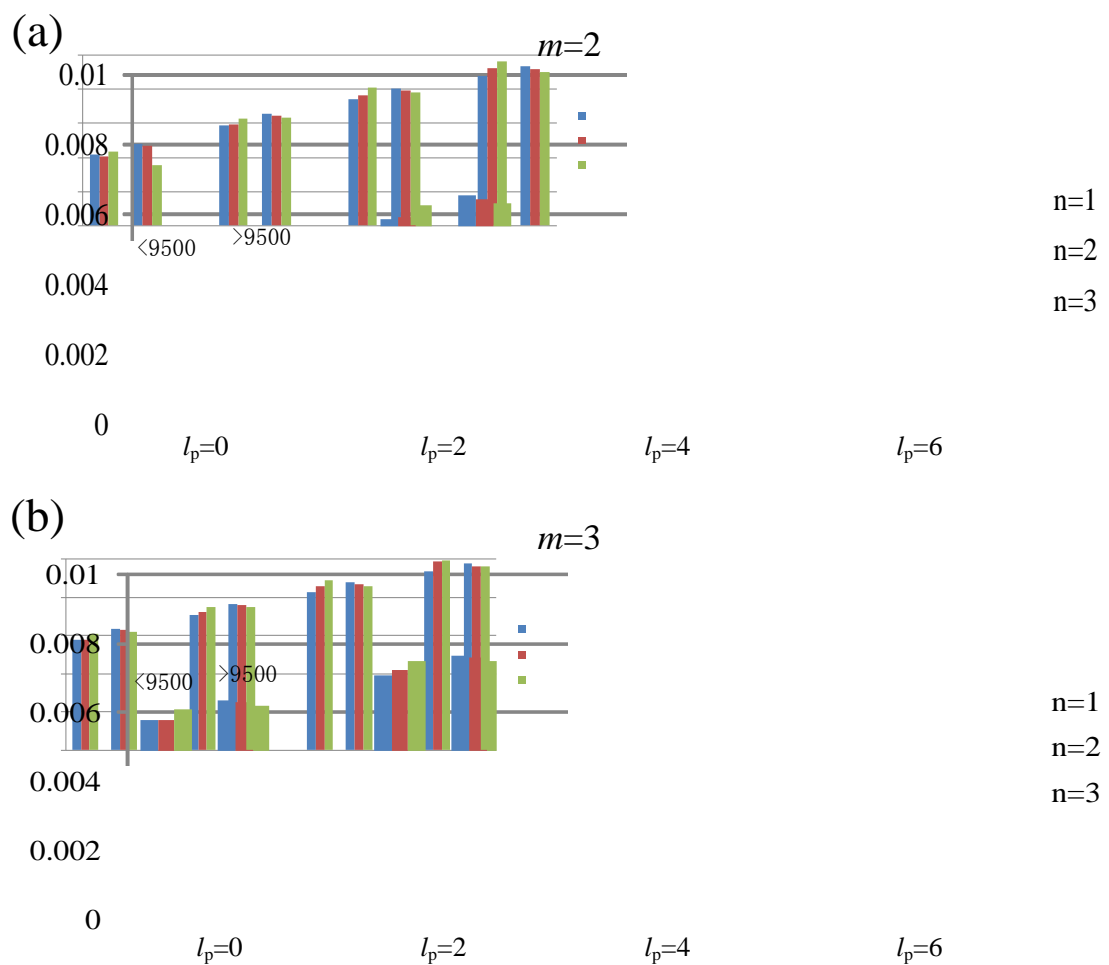
Fig. 5.5 Comparison of the system average damping loss factors before and after the characteristic frequency (9500 Hz) for different number of ABHs under different platform length l_p: (a) when $m=2$ and (b) when $m=3$.

Figure 5.6 shows the effect of the location of the ABH elements on the system

damping loss factors. Only two ABH elements are considered in the beam for the sake of simplicity. Above the characteristic frequency, the damping loss factor is almost the same for different locations of the two ABH elements. For lower frequency range, the loss factor strongly depends on the structural mode involved. Therefore, the average damping loss factors are compared in Fig. 5.7. Consistent with the results shown in Fig. 5.6, the average damping loss factors above the characteristic frequency can be barely seen. However, below the characteristic frequency, the average damping loss factors greatly reduces when the two ABH elements are connected together compared with other distribution cases, which should be avoided in the application.
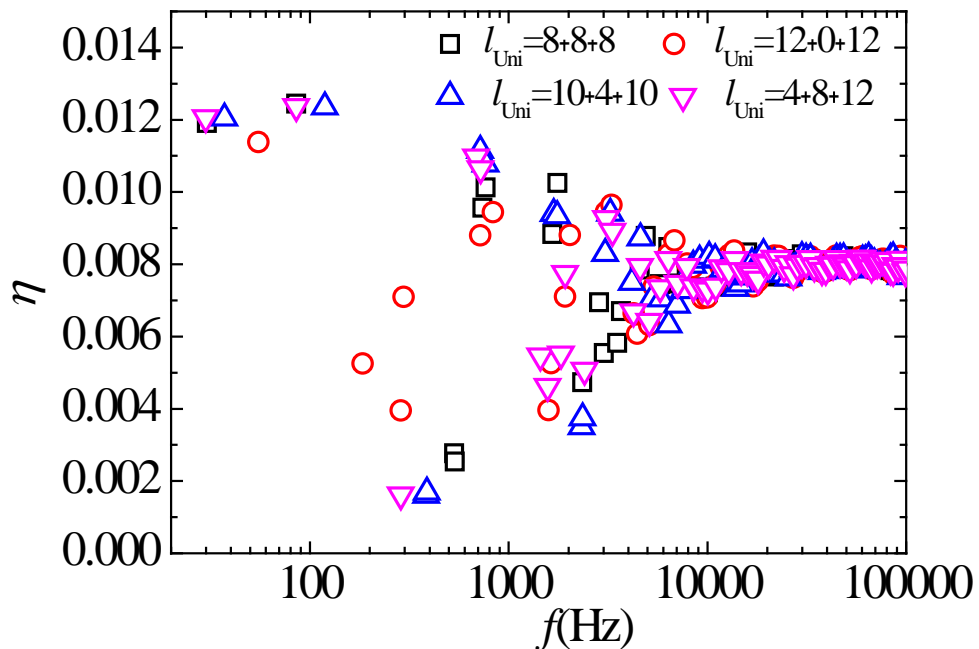
Fig. 5.6 System damping loss factors comparison for different layout of ABHs when

n=2 and *m*=2. The length of three uniform part separated by two ABH elements are used to identify the layout of the ABH elements, as shown in each symbol label.
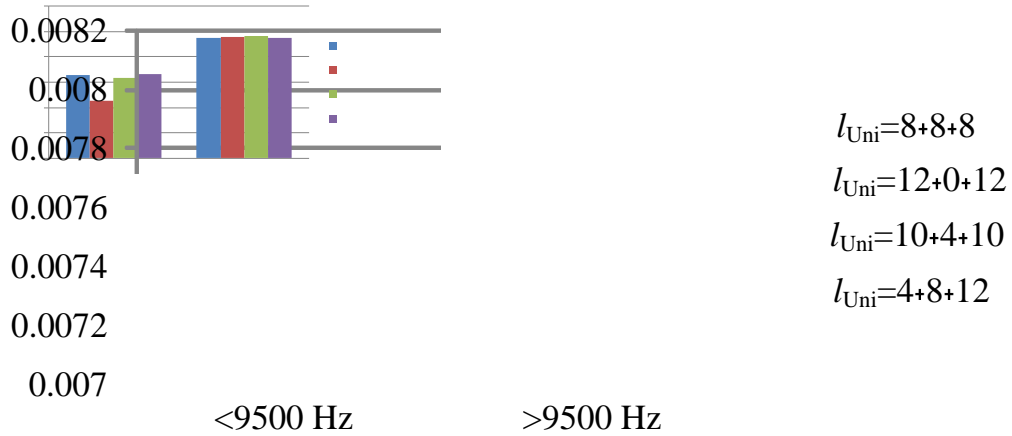
Fig. 5.7 Comparison of the system average loss factors before and after the characteristic frequency (9500 Hz) for different layout of ABHs when *m*=2.

In general, when the space for ABHs is constant and limited, for higher frequency, placing one ABH element rather than multiple ABH elements allows more effective damping; for mid-low frequency, increasing the number of the ABHs is benefit to enhance the overall damping performance. Meanwhile, a larger number of ABHs can reduce the effective frequency of the ABH effect. However, for particular frequency bands, the number of ABH elements should be carefully chosen by using the developed model because the increased damping effect is modal dependent. Besides, the layout of the ABH elements shows little effect on the overall performance of the ABH except for cases where ABH elements are connected together, which will impair the overall damping performance below the characteristic

101

frequency.

5.1.3 Multiple ABHs effect

In this section, to further investigate the possible multiple ABHs effect (for example the accumulated effect and wave filter effect), the ABH element are kept constant while the number is increased. As a numerical example, consider three free-free beams containing one, two, and three identical ABH elements, respectively. An entirely uniform beam, having the same thickness h_b and the same total length as the beam with three ABHs, is also included as a reference. For simplify, no extended platform is included in this section, namely l_p=0. The material and geometrical parameters are the same as in the Table 5.1 except for a being 8 cm and l_{ABH} being 2 cm. A unit excitation force is applied at the free end of the beam while the receiving point is placed at the other free end.

Figure 5.8 (a) compares the vibration transmission of the three ABH beams with that of the reference beam without damping layers. The vibration transmission is defined as $20\log\dfrac{w_{out}}{w_{in}}$, in which w_{in} is the input displacement at the excitation point and w_{out} is the output displacement at the receiving point. The vibration transmission of the beams with ABHs is significantly reduced in four broad frequency bands, 150-850 Hz, 2.1-8.8 kHz, 10.4-14.8 kHz, and 18.3-21.6 kHz, which can loosely be referred to as 'attenuation bands' (Comparisons of these attenuation

bands with the 'band gaps' used in infinite structures will be performed at a later stage). Meanwhile, transmission reduces quite significantly as the number of ABHs increases. The minimum transmission reaches nearly -60 dB when three ABH elements are present. This observation suggests that, compared with the uniform beam, ABH elements act as efficient vibration isolators at specific frequencies even in the absence of the damping layers. The transmission curves are compared again in Fig. 5.8 (b) for samples with damping layers applied over the ABH sections and the corresponding regions of the uniform reference beam. The damping layers show little influence on the attenuation bands in terms of both frequency distribution and attenuation intensity, which suggests that the observed vibration attenuation in the attenuation bands is not caused by the dissipation. However, energy concentration in the ABH section from the ABH effect leads to significantly reduced transmission of the beam with ABHs at the resonant frequencies, in agreement with the common understanding on the conventional ABH structures. As expected, this reduction is also increased with the number of ABH elements.
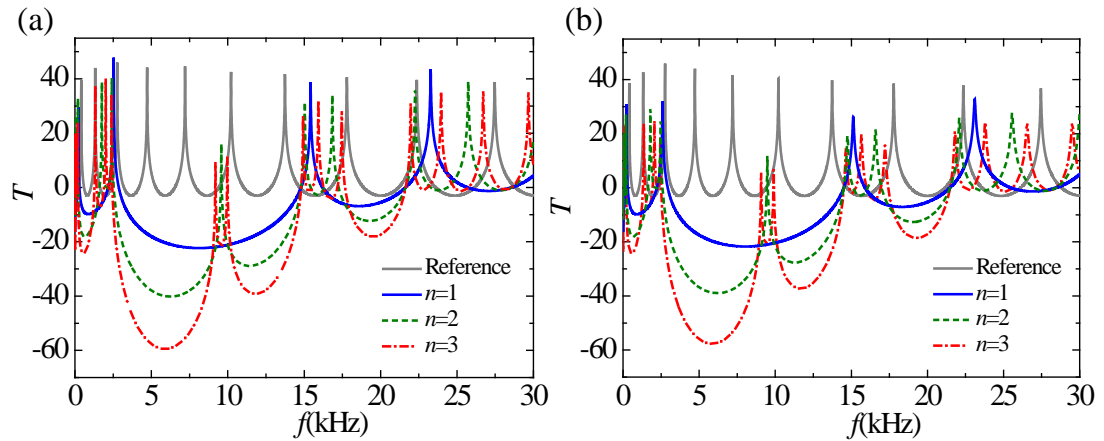
Fig. 5.8 Comparisons of vibration transmission involving beams with one, two, and three ABHs and the uniform reference beam. (a) with no damping layers applied and (b) with damping layers applied for h_d=0.02 cm

The displacement distribution at 5.8 kHz (roughly the trough of the second attenuation band) is compared in Fig. 5.9 for different beams with damping layers to examine what happens inside the attenuation bands. As can be seen, for the uniform reference beam, the vibration is fairly balanced along the entire beam span; with only one ABH element, the vibration is mainly concentrated on the ABH part while the vibration energy is attenuated to some extent at the receiving point of the uniform part. With additional ABH elements, the wave is further attenuated when passing through each ABH, resulting in negligible vibration towards the end of the uniform region for the beam with three ABH elements.
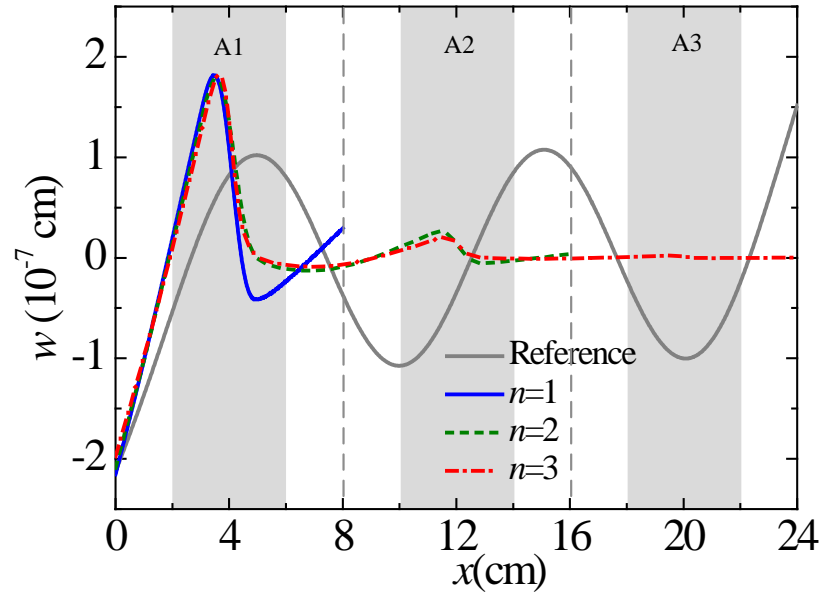
Fig. 5.9 Displacement distribution at 5.8 kHz for different beams with A1 denoting the ABH part closest to the point excitation.

Focusing now on the beam with three ABHs with damping layers, its energy and displacement distribution along the beam span is further illustrated in Fig. 5.10. Fig. 5.10(a) shows the energy ratio Γ ($\Gamma = 10\log\frac{<V^2>_{\mathrm{ABH}}}{<V^2>_{\mathrm{Unif}}}$) between each ABH part and the uniform part in terms of the averaged quadratic velocity with A1 denoting the ABH part closest to the force input. It can be seen that the energy is mainly trapped in the first ABH portion, adjacent to the force excitation, while less and less energy propagates to the subsequent ABH elements within the attenuation bands, as shown in Fig. 5.8. At other frequencies, however, the energy distribution among different ABHs is fairly balanced among different portions of the beam. This phenomenon can be substantiated by the displacement distribution at two

representative frequencies as shown in Fig. 5.10 (b). At 5.8 kHz in the second attenuation band with the lowest transmission (as also shown in Fig. 5.9), the vibration level is significantly suppressed after the wave passes through the first ABH, part A1, and the remaining vibration is almost negligible, especially for the last uniform part past the third ABH element, A3. However, at 25 kHz beyond the fourth attenuation bands, the wave is compressed within the three ABH regions with the vibration amplitude greatly amplified compared with that of the remaining uniform part. Clearly, the vibration of the uniform part is reduced because of the ABH effect, but the displacement level within each ABH area remains comparable.

In conclusion, numerical simulations show the existence of the attenuation bands, within which significant wave attenuation can be achieved using a small number of ABH elements. Apparently, they appear at relatively low frequencies, typically before the so-called characteristic frequency f_{cha} as stated in Chapter 4. Above this frequency, the incoming wavelength starts to be equal to or less than the geometrical characteristic dimension of the ABH element, which is 16731 Hz in the present case. This frequency range can be loosely called mid-to-high frequencies. Contrary to the structure with a single ABH element where waves are systematically attenuated only after the characteristic frequency [67], the structure with multiple ABHs brings new perspective to the wave attenuation.
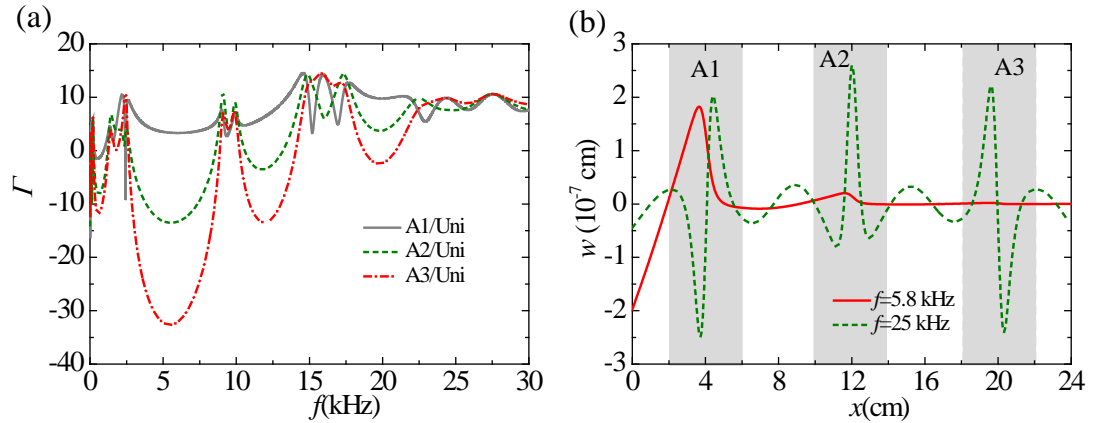
Fig. 5.10 (a) Energy ratio between the ABH part and the uniform part, with A1 denoting the ABH part closest to the excitation point, and (b) displacement distribution at 5.8 kHz and 25 kHz. The shadow areas denote the three ABH regions.

5.2 Infinite structures with periodic ABHs

To better explain the physical phenomena observed from the above analyses with multiple ABHs, infinite structures with periodic ABHs, forming so-called Phononic Crystals (PCs), are investigated. The possible band gaps existing in PCs may provide new impetus to revisit the above issue.

5.2.1 Brief introduction of Phononic Crystals

Phononic Crystals (PCs) [69] are artificial media consisting of periodic materials or components with the ability to achieve unusual wave propagation characteristics, such as waves filtering [70, 71], negative refraction [72-74], and band gaps [75-77] etc. As one of the most attractive physical properties of the PCs, band

107

gaps means the frequency bands in which elastic wave cannot propagate, thus showing great potentials for applications such as vibration control, wave manipulation and sound absorptions etc. Out of band gaps, the wave can propagate without attenuation when ignoring the material damping, which thus is referred to as passbands. The band gaps are usually exhibited in band structures, namely the dispersion curves between the eigen-frequency and the wave vector k. Because of both the materials and geometric periodic properties in PCs, the Bloch theorem reveals that the eigen-frequency and the eigen-mode also show the same periodic properties. To find the band gaps existing in PCs, we only need to find the dispersion curves in the first Brillouin zone [78]. In band structures, the frequency bands where no any dispersion curves exists are called band gaps while the remaining bands are called passbands. Theoretically, band structures only apply to ideally infinite periodic structures. For practical applications, periodic structures can only be finite, where the band gaps would exhibit a quick wave energy attenuation after passing through each unit cell. In this situation, a transmission coefficient is usually used to define the band gap characteristics. The frequency bands with extremely low transmission coefficient usually correspond to the band gaps. Meanwhile, the transmission coefficient will further reduce as the number of cells increases.

Band gaps can be generated mainly through two physical mechanisms: Bragg scattering [79-82] or local resonances [83-91]. The former are usually formed by placing scatterers periodically into the matrix structures. For one-dimensional

phononic beams, this can be achieved by periodically connected two components A and B with different material properties (Young's modulus and density) and cross sections [82, 92], as shown in Fig. 5.11(a). To ensure destructive interferences, the difference between the material properties and cross sections should be large enough to generate band gaps. Meanwhile, the band gaps can be only obtained in the frequency bands where the wavelength scales is comparable with the lattice constant [78]. Therefore, to attenuate low frequency and long wavelength waves, the unit cell needs to be prohibitively large. Meanwhile, a large number of elements are needed to achieve broad band gaps. These limitations can be overcome using locally resonant band gaps by attaching local resonators [81, 93], with typical one-dimensional phononic beams as shown in Fig. 5.11(b). The band gaps are more dependent on the local resonances of the scatterers rather than the periodic elements arrangement. Therefore, the band gaps can reach relatively low frequency bands without large scale of lattice constant. However, as shown in Fig. 5.11(b), since the resonators usually contain single-degree-of-freedom, the gaps are narrow, near the resonant frequencies of the resonators. These two types of band gaps are difficult to conciliate. In addition, the demanding fabrication process and numerous interfaces required by conventional PCs also hamper the practical applications of the PCs.
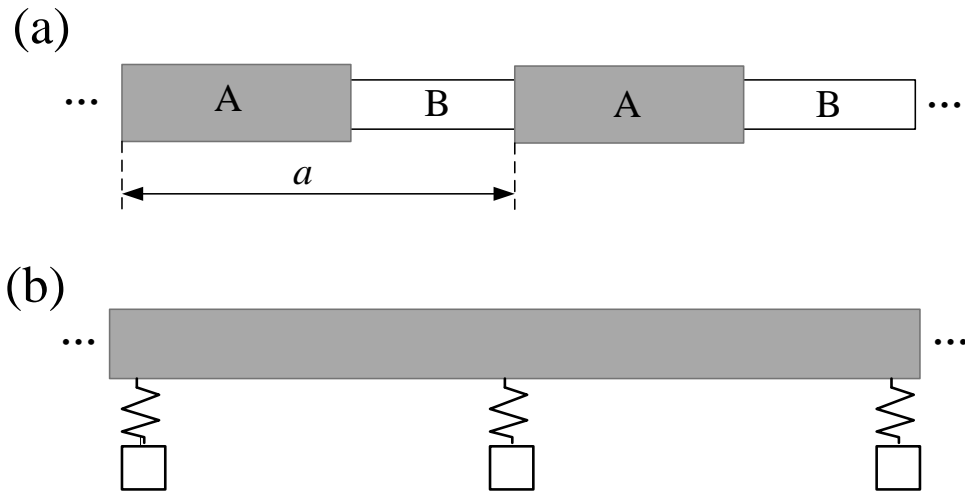
Fig. 5.11 sketch of two main typical types of phononic beams: (a) Bragg scattering mechanism and (b) locally resonant mechanism.

The ABH effect may offer a new perspective to resolve the aforementioned problem. In an idealized ABH structure, the phase and group velocities of the flexural waves gradually reduce to zero at the tip of the taper, thus annulling wave reflection. When this happens, the tapered ABH becomes an ideal energy absorber because of the high energy concentration and trapping. Despite the inevitable truncated thickness of the structures in practice, considerable ABH effect can still be observed with /without the use of a damping layer coated over the ABH region [42, 43, 53]. An interesting question is whether broad band gaps could be achieved at low frequencies through ABH effects by using a small number of ABH elements without attaching additional elements and creating multiple interfaces. If achievable, how can simulation and design serve to predict this behavior. To the best of our knowledge, there is only one paper dealing with an infinite 2D ABH lattice [50]. The work

110

clearly shows the ABH cells can be used to generate unique dispersion properties, such as negative group refraction index, zero group velocity in the fundamental modes, and birefraction, etc. Applications of ABH-like profiles in various meta-surfaces are also attempted in the realization of anomalous refraction, focal lenses and phase masks [51]. However, due to the complex wave travel paths in a 2D system, whether absolute band gaps exist still remains unknown. If any, the band gaps could also be quite narrow, specific to certain types of wave modes. Owing to the relatively simple wave travel path in 1D structures, it is interesting to revisit this issue in 1D configuration, which may explain the physical phenomena observed in Set. 5.1.3.

5.2.2 Modelling procedure

The developed wavelet-decomposed energy method is expanded to investigate an infinite lattice with periodic ABH cells, as shown in Fig. 5.12.
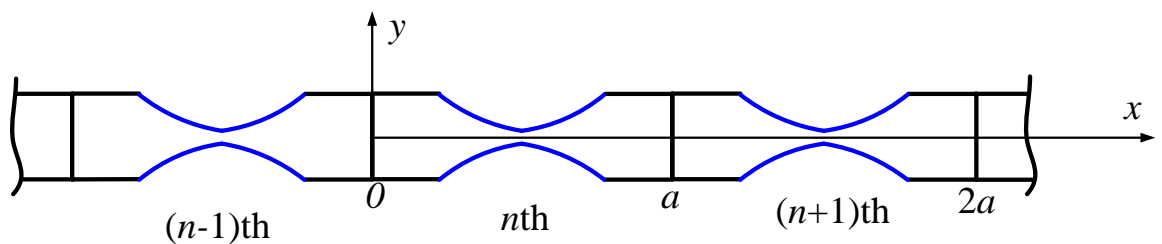
Fig. 5.12 Sketch of an infinite Euler-Bernoulli beam with periodic ABH cells with a lattice constant a.

The flexural displacement w is again expanded using Mexican Hat Wavelets as

in Eq. (5.1). The Lagrangian of the system is written as the sum of Lagrangians of every unit cell

$$L = \sum_{n=-\infty}^{+\infty} L_n = \sum_{n=-\infty}^{+\infty} E_{nk} - E_{np} \tag{5.4}$$

where E_{nk} and E_{np} are, respectively, the kinetic energy and the potential energy of the nth unit-cell, expressed as

$$E_{nk} = \frac{1}{2}\int\rho\left(\frac{\partial w_n(x)}{\partial t}\right)^2 dV , \quad E_{np} = \frac{1}{2}\int EI(x)\left(\frac{\partial^2 w_n(x)}{\partial x^2}\right)^2 dx \tag{5.5}$$

Considering periodic boundary conditions, the displacement and its second derivative between the nth and the $(n+1)$th unit-cells should satisfy the following relationship

$$w_{n+1}(x+a) = e^{jka}w_n(x) \tag{5.6}$$

$$w''_{n+1}(x+a) = e^{jka}w''_n(x) \tag{5.7}$$

where k is the wave vector and a the lattice constant.

By substituting Eqs. (5.6) and (5.7) into Eq. (5.5), the relationship $L_{n+1} = e^{2jka}L_n$ is obtained. Similarly, the Lagrangian of any $(n+q)$th unit-cell is obtained by $L_{n+q} = e^{2qjka}L_n$ with q being any integer. Thus Eq. (5.4) can be rewritten as

$$L = \sum_{n=-\infty}^{+\infty} L_n = L_n \sum_{q=-\infty}^{+\infty} e^{2qjka} \tag{5.8}$$

Therefore, the extremalization of the Hamiltonian function of the entire infinite system can mathematically be expressed in terms of the Lagrangians of one unit-cell as follows

112

$$\frac{d}{dt}\left(\frac{\partial L_n}{\partial \dot{a}_{i,s}(t)}\right) - \frac{\partial L_n}{\partial a_{i,s}(t)} = 0 \tag{5.9}$$

In other words, solving the Lagrange's equations of one-unit cell leads to the result for the whole system. Meanwhile, this set of Lagrange's equations has a very similar form as the one established in Sec. 5.1 for one ABH element. The only difference is that this single unit-cell is boundary free with artificial spring stiffnesses K and Q being set to zero, and satisfies the periodic boundary conditions in terms of displacement, rotation angle, bending moment, and shear force as follows

$$w_n(a) = e^{jka}w_n(0) \tag{5.10}$$

$$w_n'(a) = e^{jka}w_n'(0) \tag{5.11}$$

$$w_n''(a) = e^{jka}w_n''(0) \tag{5.12}$$

$$w_n'''(a) = -e^{jka}w_n'''(0) \tag{5.13}$$

The displacement w can be rewritten as $w(x,t) = \sum_{i=0}^{m}\sum_{s} a_{i,s}(t)\varphi_{i,s}(x) = \sum_{i=1}^{n} a_i\varphi_i(x)$.

Taking the periodic boundary condition Eq. (5.10) into account, one can get

$$\sum_{i=1}^{n}\left(\varphi_i(a) - e^{jka}\varphi_i(0)\right)a_i = 0 \tag{5.14}$$

$$a_n = \sum_{i=1}^{n-1}\lambda_i\, a_i \tag{5.15}$$

with $\lambda_i^m = \dfrac{A_i^m}{A_n^m}$ and $A_i^m = \varphi_i^m(a) - e^{jka}\varphi_i^m(0)$. Here, the superscript m denotes the derivative order. The displacement can then be re-expressed as

$$w(x,t) = \sum_{i=1}^{n-1}\left[\varphi_i(x) - \lambda_i\varphi_n(x)\right]a_i \tag{5.16}$$

113

Considering additional periodic boundary condition Eq. (5.11), we can get a_{n-1} and the displacement similarly as

$$a_{n-1} = \sum_{i=1}^{n-2} \left(\frac{\lambda_i' - \lambda_i}{-\lambda_{n-1}' + \lambda_{n-1}} \right) a_i \tag{5.17}$$

$$w(x,t) = \sum_{i=1}^{n-2} \left\{ \varphi_i(x) + \frac{\lambda_i' - \lambda_i}{-\lambda_{n-1}' + \lambda_{n-1}} \varphi_{n-1}(x) + \left[\frac{\lambda_i' - \lambda_i}{\lambda_{n-1}' - \lambda_{n-1}} \lambda_{n-1} - \lambda_i \right] \varphi_n(x) \right\} a_i \tag{5.18}$$

With further consideration of the other two periodic boundary conditions, Eqs. (5.12) and (5.13), the displacement can be accordingly rewritten as detailed in Appendix A. Submitting the displacement expression into Eq. (9), one can get a matrix equation similar to Eq. (3) in the harmonic regime. For each given value of wave vector k, the corresponding eigen-frequencies can be determined from the matrix equation. This allows us to obtain the dispersion curves of the lattice, from which band characteristics of the structure can be revealed.

5.2.3 Model verification and mechanism exploration

Using the same material and ABH parameters as in Sec. 5.1.3, infinite periodic structures are investigated hereafter to explain the physical phenomena previously observed on the finite structures with multiple ABHs.

In Fig. 5.13 we compare the dispersion curves obtained using the present model under different periodic boundary conditions with those from the FEM results using COMSOL Multiphysics 5.2. For the FEM, one 2-D unit-cell is developed with a

114

sufficient mesh with free tetrahedral and the Floquet periodic boundary condition is imposed at the edges of the unit-cell. A reduced frequency f_R, defined as $f_R = fa/c$, is also introduced as a reference, with c being the wave velocity of the uniform beam (with a length of a). As can be seen, the results from the present model with two periodic boundary conditions, displacement w and rotation angle w', match very well with the results from the FEM especially in the mid-low frequency range. The differences at the high frequencies are mainly attributable to neglect of the shear and torsional effect in the present method. Note that using the additional periodic boundary conditions of w'' and w''' brings barely noticeable changes to the results. This indicates that the two periodic boundary conditions on the displacement and rotation angle are sufficient to describe the structural periodicity as well as the band structures. Meanwhile, five band gaps are shown to exist below 30 kHz. The first three are relatively flat, showing typical characteristics of locally resonant band gaps. The bandwidth versus the central frequency of the band, *i.e.* $\dfrac{f_{R\_upper} - f_{R\_lower}}{\left(f_{R\_upper} + f_{R\_lower}\right)/2}$, is used to describe the relative bandwidth. The relative bandwidths of the first three band gaps are 1.38, 1.21, 0.35, respectively, which are very broad compared with the conventional locally resonant bandwidths.
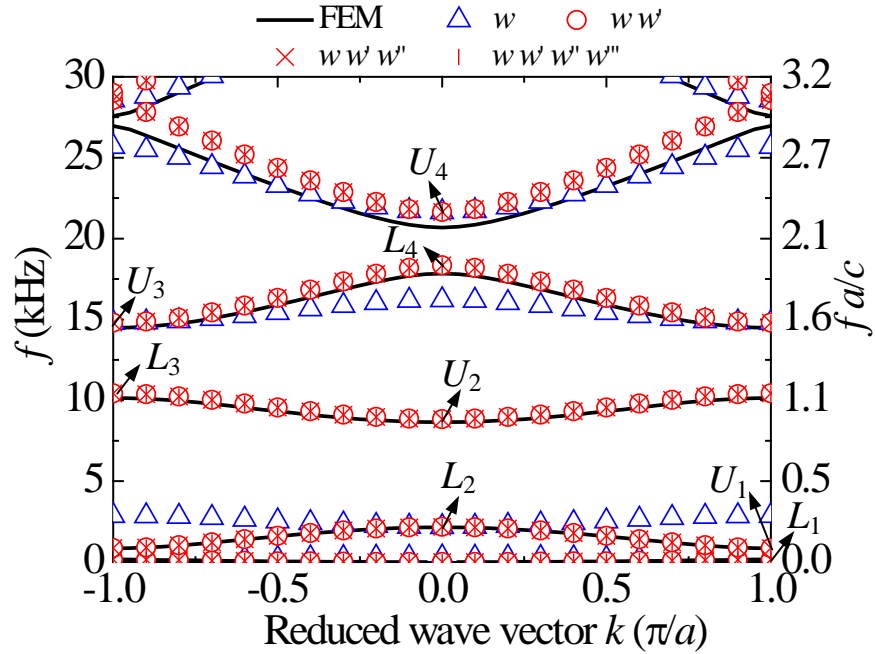
Fig. 5.13 Dispersion curves. Comparison between the results from the present infinite periodic model with different periodic boundary conditions and from the FEM. $f_R = fa/c$ is the reduced frequency with c being the wave velocity of the uniform beam having length a.

The observed phenomenon can be explained by the theory elaborated in Mead [94, 95]. In symmetric structures, all coupling coordinates between any two neighboring unit-cells can be divided into two types: the first type (type I coordinate) has the same sign and magnitudes, whereas the second (type II coordinate) has opposite signs and equal magnitudes for a symmetric vibration mode. It was theoretically proven that the bounding frequencies of the passbands can be identified with the natural frequencies of a single periodic element with two classes of boundary conditions – type I coordinate locked and type II free, or oppositely, type I

free and type II locked. Specifically, the displacement and the rotational slope belong to I and II coordinates, respectively. Therefore, in the present case, the aforementioned periodic boundary condition in terms of displacement and rotational slope can fully determine the band structures. When predicting the band gaps using one periodic element, this corresponds to simply-supported or sliding-sliding boundary conditions, which can be achieved by setting K or Q to zero.

The above analyses can be further validated by comparing the mode shapes between the bounding frequencies of the band gaps (labeled in Fig. 5.13) and the resonant frequencies of a single element, as shown in Fig. 5.14. The mode shapes, as well as the resonant frequencies (not shown here), from the single element match perfectly with those of the infinite beam. We highlight that, with the help of the previously developed finite model, one can obtain band structure information by only analyzing a single element rather than the entire infinite periodic structure. This greatly saves calculation time and provides a simple way to predict, and eventually optimize, band structures based on a single element. Looking back at the mode shapes of the unit-cell, vibration mainly concentrates on the ABH part with reduced wavelengths, as shown in Fig. 5.14. The ABH effect promotes wave accumulation with decreasing structural thickness and, consequently, the wave amplitude is amplified. Ideally, if the thickness of the ABH approaches zero, no wave will be reflected back, such that an ABH element could be an ideal local resonator containing multiple localized frequencies for the full frequency band. The inevitable

117

truncation thickness however generates wave reflections, albeit weak in practice, partly impairing local resonance effects. When the ABH part dominates the vibration of the unit-cell while the uniform part is weakly activated, locally resonant modes and band gaps appear, exemplified by the first and third modes and band gaps shown in Fig. 5.14 and Fig. 5.13. Conventional methods to achieve locally resonant band gaps use single-degree-of-freedom spring mass resonators, which are only effective near their resonant frequencies within a relatively narrow band gap. In present case, however, the ABH part acts as a continuous local resonator with multiple degrees of freedom, thus generating multiple broad locally resonant band gaps. The local resonance is gradually weakened when the uniform part is activated with increasing frequency, as shown in the mode shape of band gap 4 in Fig. 5.14.
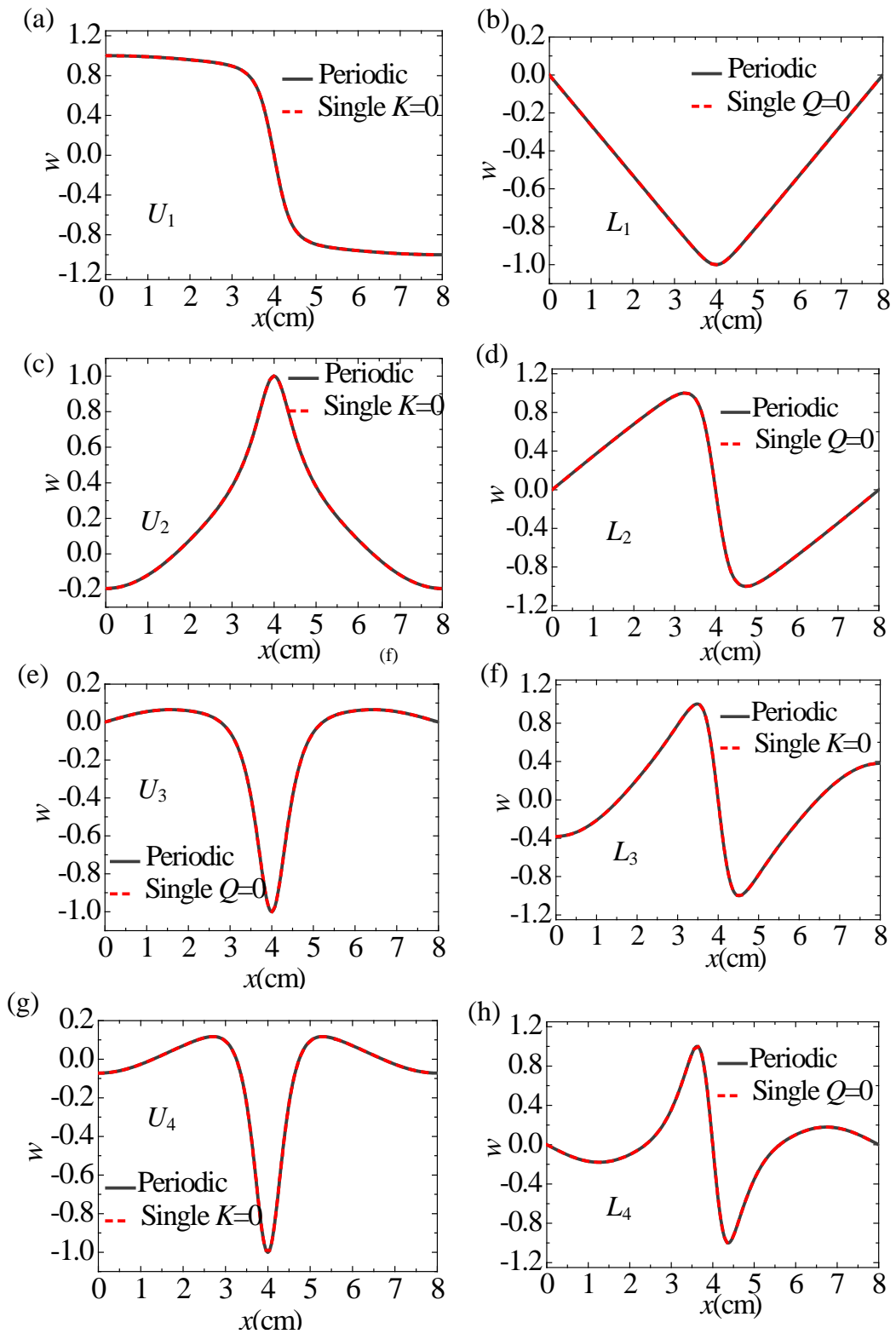
Fig. 5.14 Mode shape comparisons between the bounding frequencies of the band

gaps and the resonant frequencies of a single element: the upper row relates to the

upper bounding frequencies while the lower row is the lower bounding frequencies of each band gap.

5.2.4 Comparison with finite structures

To demonstrate the correlation between the behavior of the finite structure and that of the infinite periodic structure, the dispersion curves of the infinite periodic beam and the vibration transmission of the finite beam with three ABHs are re-plotted and compared in Fig. 5.15. The distribution of the transmission attenuation bands is in good agreement with the band gaps. Moreover, only three ABH elements are needed to create attenuation bands, as a result of the dominant role played by the local resonant mechanism of the ABH elements. Contrary to Bragg scattering, which strongly depends on the periodicity of the elements, the locally resonant effect relies on the locally resonant characteristics of the unit-cells more than the periodicity.[24] Consequently, the attenuation bands obtained here are also due to the locally resonant characteristics of the unit cells rather than the periodicity of the elements in the beam structures.
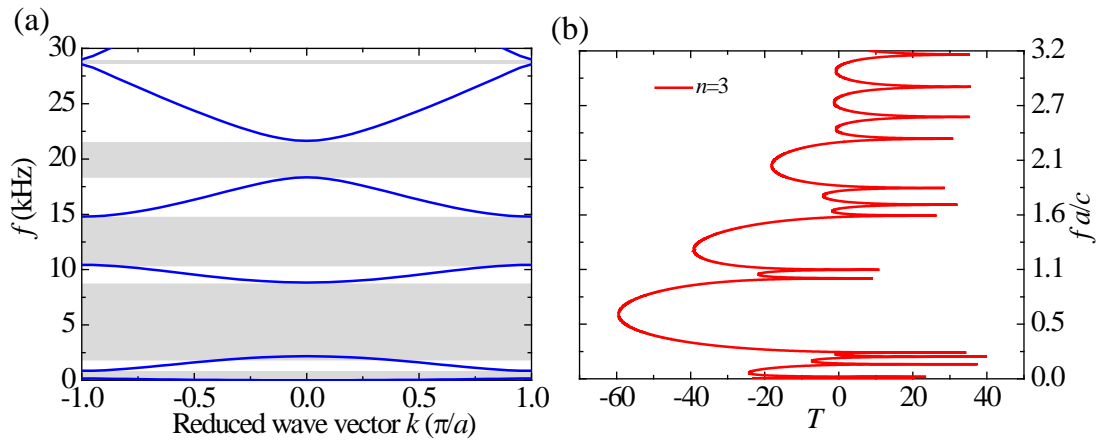
Fig. 5.15 (a) Dispersion curves of the infinite periodic beam; (b) transmission of finite beam with three ABH elements

In infinite periodic beams, band gaps are the frequency bands within which waves cannot propagate. In finite beams, however, it is relevant to understand what happens in the attenuation bands and where the vibration energies go if they are not absorbed by the added damping as observed in Fig. 5.8. To answer this question, the driving point mobilities, *i.e.* the ratio between the velocity of the input force point over the input force, in a finite beam with three ABH elements and the uniform reference beam are compared in Fig. 5.16. As can be seen, the driving point mobility of the beam with ABHs shows no resonant peaks in the attenuation bands and has quite low amplitude compared with that of the uniform beam. Since the input force is a unit force, the driving point mobilities can also reflect the level of the input energy. Therefore, in the attenuation bands, the input energy in the beam with ABH elements is much lower than that of the uniform beam because of the structural inherent properties. In another word, the special design of the beam hampers the vibration

energy input leading to the significant reduction of the vibration level of the structure.
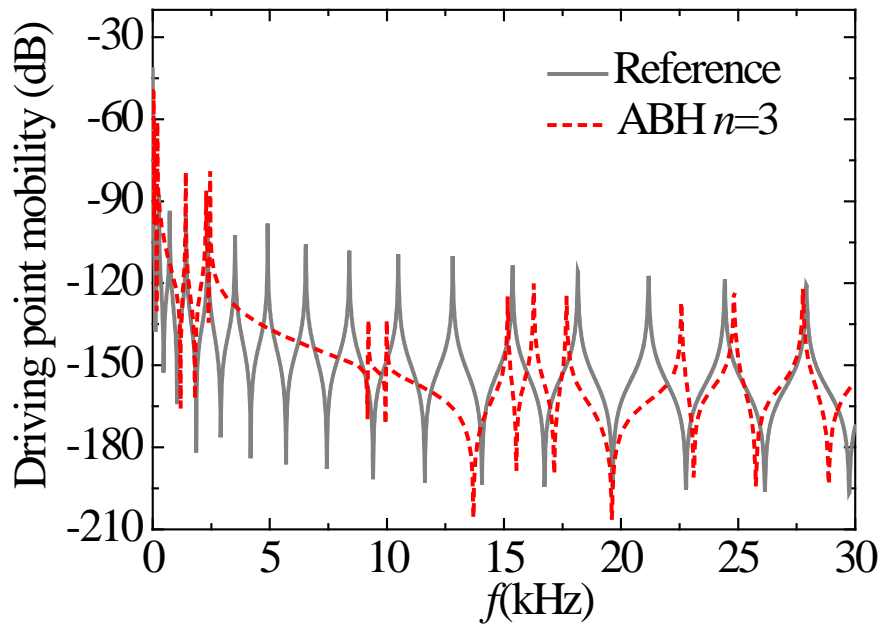
Fig. 5.16 Driving point mobility comparisons between the finite beam with three ABH elements and the uniform reference beam when no damping layers are applied.

5.2.5 Parametric analyses

Since the band gaps mainly depend on the local resonant of the ABHs, it is important to investigate effects of the geometrical parameters of the ABH taper, such as the power index m , the truncation thickness h_0, the length of the extended platform on the band gaps.

Figure 5.17 illustrates the first four band gaps for different power indices m. As one can see, increasing m would decrease the lower and upper boundary of band gaps

overall. Meanwhile, in most cases, the bandwidth at low frequencies also increases with larger m. The passbands also become narrower with increasing m, which leads to flatter band gaps on the dispersion curves and better local resonant characteristics. This can be understood in light of the positive effect of m on the ABH effect. It is relevant to note that, with an excessively large m, the smoothness criteria would no longer be satisfied [7, 16], and would possibly generate wave scattering, impairing the ABH effect. As a result, the local resonance effect may also be weakened and so would the locally resonant band gaps.
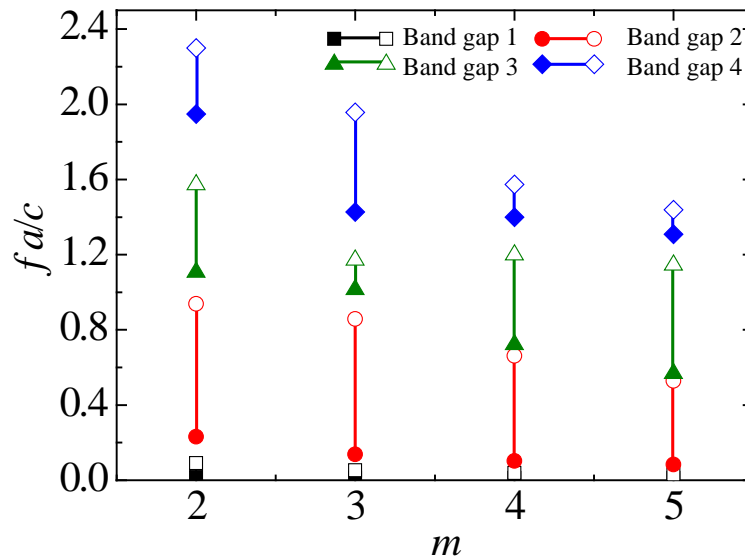
Fig. 5.17 Effect of the power index m on the band gaps: the solid symbols denote the lower boundaries of the band gaps, the open symbols denote the upper boundaries, and the solid line between symbols indicates the bandwidth.

Fig. 5.18 illustrates how the truncation thickness h_0 affects the band gaps. Nearly every band gap becomes wider as h_0 decreases, along with a significant

reduction in the passbands. This can be directly attributed to the enhanced ABH effect. If further decreases in the truncation thickness h_0 are allowed, even broader band gaps can theoretically be achieved, although the extremely thin thickness is most likely prohibited by manufacturing difficulties and ensuing structural strength problems.
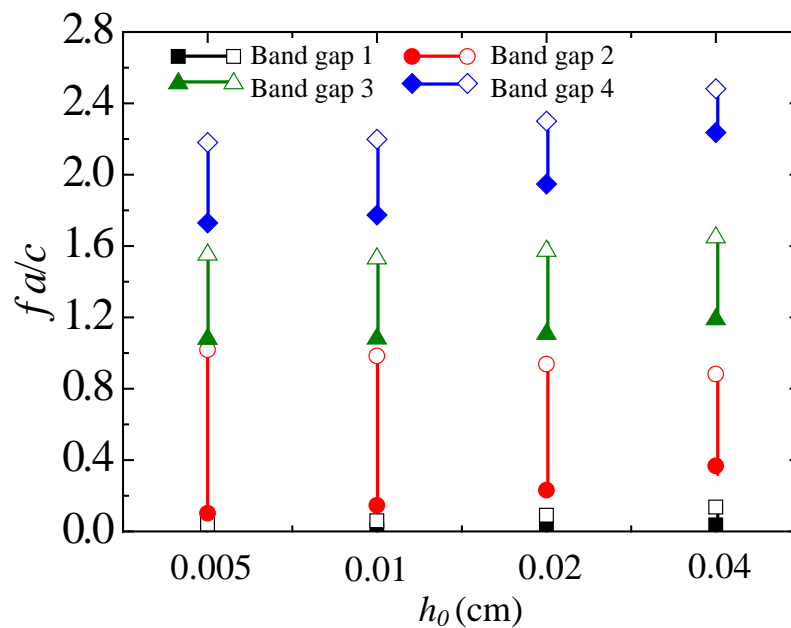
Fig. 5.18 Effect of the truncation thickness h_0 on the band gaps: the solid symbols denote the lower boundaries of band gaps, the open symbols denote the upper boundaries, and the solid line between symbols indicates the bandwidth.

Keeping the ABH profile and lattice constant as the same, the effect of the normalized length of extended platform l_p/a on the band gaps is also shown in Fig. 5.19. It can be seen that lengthening the extended platform would significantly lower the band gaps. This is consistent with the effect of extended platform on lowering the

ABH effect. The bandwidth of passbands between each band gaps reduces. However, the bandwidth of band gaps also reduces overall. Therefore, for particular intended application frequency bands, the structure needs to be carefully designed based on the present model.
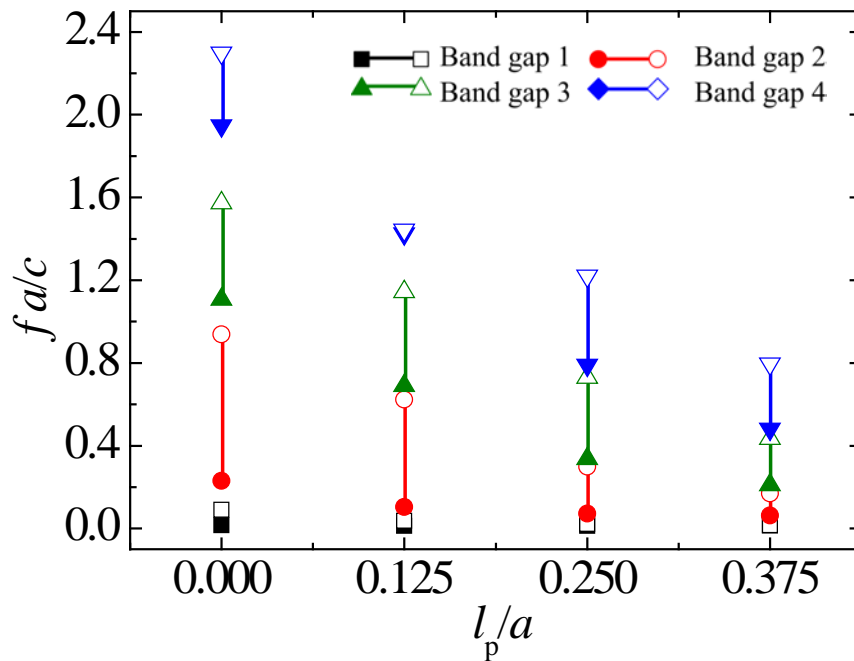
Fig. 5.19 Effect of the normalized length of extended platform l_p/a on the band gaps: the solid symbols denote the lower boundaries of band gaps, the open symbols denote the upper boundaries, and the solid line between symbols indicates the bandwidth.

Meanwhile, when the ABH profile is kept constant, the effect of the lattice constant a on the band gaps is also shown in Fig. 5.20. As can be seen, increasing the lattice constant would widen the normalized bandwidth of the band gaps overall. Meanwhile, the upper and lower frequencies of the band gaps would also increase

overall. Note that the frequency in vertical axis is normalized with the wave length (c/a), which is positive related with the lattice constant a. Therefore, the actual frequency and bandwidth decrease with the increasing of the lattice constant, which is consistent with the conventional PCs suggested.
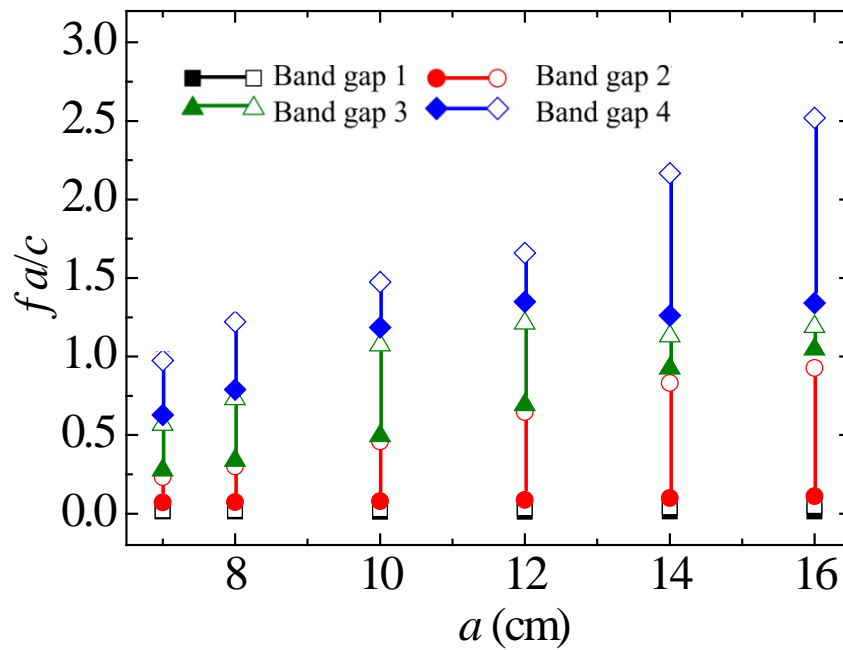
Fig. 5.20 Effect of the lattice constant a on the band gaps: the solid symbols denote the lower boundaries of band gaps, the open symbols denote the upper boundaries, and the solid line between symbols indicates the bandwidth.

Finally, the way that the abovementioned parameters affect the band structures and the corresponding attenuation performance in finite structure is examined. As an example, consider infinite periodic and finite periodic beams, both containing identical ABH elements with $m=2$, $a=8$ cm, $l_p=0$ and $h_0=0.005$ cm. The dispersion

curves of the infinite beam and the transmission of the finite beams with different ABH elements are compared in Fig. 5.21. For the infinite beam, extremely broad band gaps can be observed, covering nearly the entire frequency band below 20 kHz with only a few narrow passbands. For the finite beams, corresponding attenuation bands are also observed. It is interesting to note that transmission attenuation gaps start to appear with only one ABH element because of the locally resonant effect. With three periodic elements, the transmission can be as low as -120 dB, leading to a significant broadband and low frequency vibration attenuation by using only a few elements without any add-on resonators or creating geometrical or material discontinuous like conventional lattices. It is relevant to mention that this happens because of the sequential wave travel path across the ABH cells in 1-D beam structures.
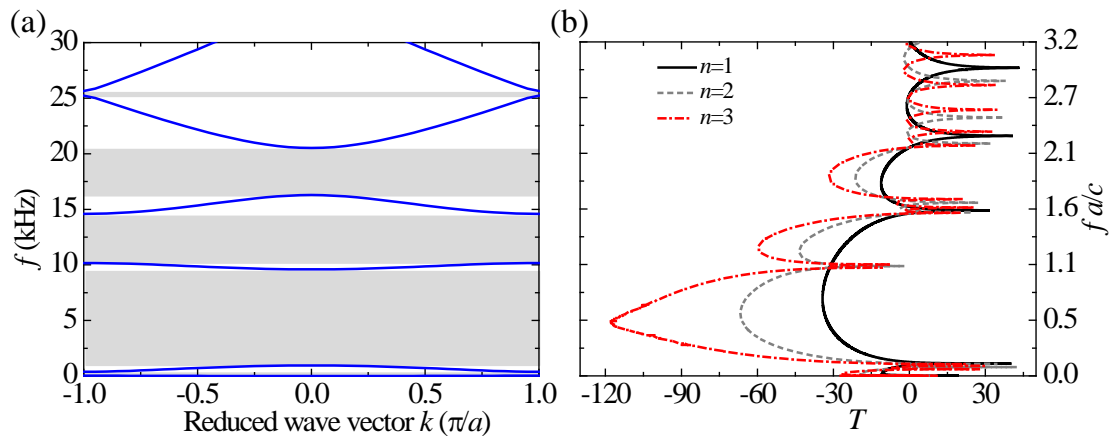
Fig. 5.21 (a) Dispersion curves of an infinite periodic beam, and (b) the corresponding transmission of finite beams with different ABH elements for $m=2$, $a=8$ cm, $l_p=0$ and $h_0=0.005$ cm

5.3 Short summary

In this Chapter, an Euler-Bernoulli beam containing multiple ABHs is studied based on the developed wavelet-decomposed energy method. On one hand, the effect of different number of ABH elements is investigated when the space for ABHs is constant and limited. The results show that more ABH elements help to lower down the effective frequency of the ABH effect and enhance the overall damping performance at mid-low frequencies. For particular low frequency bands, the number of ABH elements should be carefully chosen by using the developed model because the increased damping effect is modal dependent. However, for higher frequency, placing one ABH element rather than multiple ABH elements is beneficial for more effective damping. Besides, the layout of the ABH elements shows little effect on the overall performance of the ABH effect except for cases where ABH elements are connected together, which will lower down the overall damping performance below the characteristic frequency.

On the other hand, broadband attenuation bands and wave suppression phenomena are observed at relatively low frequencies below the so-called characteristic frequency. To explain the underlying physical phenomena, the wavelet-decomposed energy model is further extended to investigate infinite structures with ABH unit cells. The periodic boundary conditions in terms of displacement and rotational slope are shown to be sufficient to describe the structural

periodicity and the corresponding band structures numerically and analytically. Using this model, the frequency bounds of the band gaps can be predicted solely based on the resonant frequencies of a single cell with simply-supported or sliding-sliding boundary conditions. Therefore, the band structures can be easily obtained using the proposed finite model without calculating the dispersion curves of corresponding infinite structures. Numerical results show that the observed attenuation bands correspond to the band gaps of the corresponding infinite structures with the same ABH elements. Analyses on eigenmodes show that the band gaps can be attributed to the local resonances of the ABH elements as a result of the ABH effect. Therefore, increasing the taper power index m within the smoothness criteria, or reducing the truncation thickness h_0 within the allowable practical range, would help generate broader and lower-frequency band gaps. Meanwhile, extending platform can also lower the band gaps. For 1D structures of finite size, significant wave attenuation phenomenon occurs because of the enhanced locally resonant effect of multiple ABH cells. Because of the unique wave propagation feature of the 1D structures, waves pass through each ABH cell, collectively forming a more efficient broadband absorber as long as the ABH cell is cut-on to be effective, even at a relatively low frequency.

As to the structure itself, this Chapter proposes a new type of beam structure to achieve broad attenuation bands in the relatively low frequency region. Contrary to the conventional resonant lattices, only a very few ABH elements are needed with no

additional resonator attachment or multiple geometric or material discontinuities. These appealing features may offer great potential for applications such as vibration isolator and wave filter designs in beam structures.

As to the model itself, because of the remarkable flexibility and unique features offered by wavelets, the wavelet-decomposed energy model can be expanded to deal with infinite periodic structures. It provides efficient platform to solve problems with rapid space-varying wavelengths or structures with severe geometric or material inhomogeneity in conventional PCs.

Chapter 6 Beams with Periodic ABHs for Vibration Applications

Owing to the Bragg scattering or local resonance mechanisms, band gaps in conventional PCs are attractive for applications such as vibration control, wave manipulation and sound absorptions. Their practical implementations, however, are hampered by several factors, among which the large number of cells required and their impractically large size to ensure the appearance of stopbands at reasonably low frequencies are on the top of the list. The combined use of the Bragg scattering and locally resonant effects can, in principle, result in wider and lower-frequency band gaps. The improvement obtained, however, is somehow limited to a certain frequency range in the cases reported in the open literatures [96-99]. Although topology optimization is also attempted to achieve broader band gaps, the optimized unit cells usually have complex geometry which is difficult to fabricate [100-103]. In a different prospective, most PCs are usually tied with the inherent structural weakness due to the multiple structural interfaces, which are needed to create structural impedance changes. Therefore, the search for PCs with broad band gaps in both low and mid-high frequency range whilst ensuring acceptable structural properties without attaching additional elements and multiple interfaces becomes important.

As shown in the previous Chapter, an Euler-Bernoulli beam embedding ABH

features can generate locally resonant band gaps. The observed band gaps, albeit much broader than conventional local resonant band gaps, are limited to relatively low frequency range. Besides, the structure still inherits the existing structural weakness problems due to the extremely thin truncation thickness of the conventional ABH cells. In the present Chapter, we propose a new type of PCs, by capitalizing on the unique ABH features and by exploring the dual benefit of the locally resonant and Bragg scattering effect. In the proposed design, ABH profiles are carved inside of a uniform unit cells to create locally resonant band gaps whilst ensuring good structural stiffness/strength. Meanwhile, to produce the effective coupling between the Bragg scattering and local resonances, a crosspiece connecting the two branches of the ABH indentation (referred to as strengthening stud) is added in the hollowed ABH area. This allows the generation of ultrawide band gaps nearly over the entire frequency range without complex geometry and add-on attachment from the outside of the structure. The band structures of the proposed phononic beams (with and without studs) and their generation mechanism are first analyzed and compared in Sec. 6.1 and 6.2. Key parameters, *i.e.* the stud length and the parameters of ABHs, are investigated in Sec. 6.3 in views of possible tuning of the band gaps. Experiments using only three ABH cells, are then carried out in Sec. 6.4 to validate the numerically observed band gaps. Finally, conclusions are drawn. Much of work presented in this Chapter has been included in Ref. [104]

6.1 Finite element model

The proposed phononic beam consists of a uniform beam lattice with its inside being carved by a double-leaf ABH profiles, whose thickness variation is described as $h(x) = \varepsilon x^m + h_0$ [67]. The unit cell design and geometrical parameters are shown in

Fig. 6.1. The design ensures the structural integrity on the lattice surface and relatively high structural stiffness and strength, empowering the beams with reasonable transverse load-bearing capability. In the analyses, the unit cell length a = 0.12 m and the beam thickness h_b = 0.0064 m. Each ABH branch takes the form of $h(x) = 3x^2 + 0.0005$ with a truncation thickness h_0 = 0.0005 m and the length l is set to be 0.03 m. The unit cell is made of steel with a mass density of 7800 kg/m^3, Young's modulus of 210 Gpa, and Poisson's ratio of 0.3. The band structures are calculated using finite element software COMSOL Multiphysics v5.2. Because of the non-uniform profile, 2D unit cells are modeled through sufficiently dense mesh with triangular elements in Solid Mechanics Module. The Floquet periodic boundary condition is imposed at the edges of the unit cell and a parametric sweep is applied over the reduced wave vector k. Note that only flexural waves are considered.
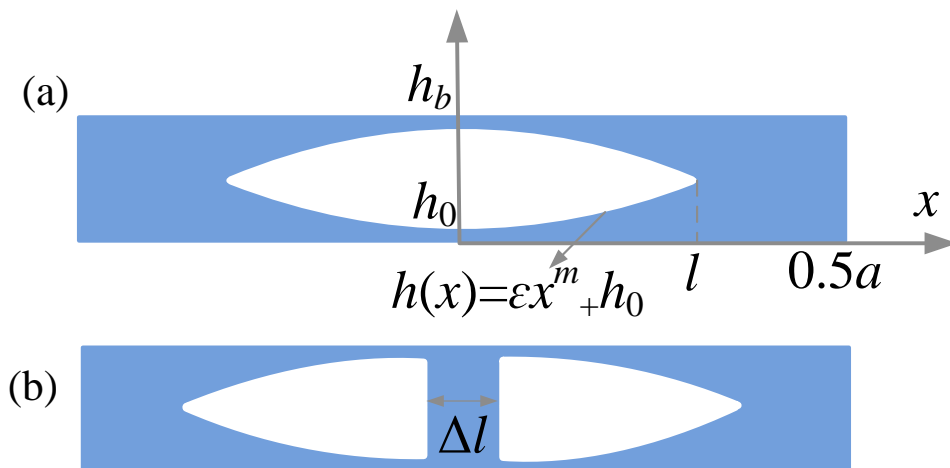
Fig. 6.1 Unit cells of the proposed phononic beams with the same lattice constant a and beam thickness h_b: (a) carved inside according to $h(x) = \varepsilon x^m + h_0$ with a length l

and a truncation thickness h_0; (b) the same symmetrical tapered profiles are embedded and connected by a strengthening stud of length Δl.

6.2 Band structures of the periodic beams

Phononic beams without the strengthening stud ($\Delta l = 0$) are first considered with their band structures depicted in circles in Fig.6.2. A non-dimensional frequency, $f_R = fa/c$, is included in the right vertical coordinate as a reference with c being the flexural wave velocity in the uniform part (Note other frequency terms used in the following discussion are also normalized with c/a). The first two broad band gaps are obtained with the normalized bandwidth $\Delta f / f_c = 86.3$ % and 110% respectively, where Δf is the bandwidth and f_c is the center frequency of the gap. These two band gaps are rather flat, which means that the slope of the dispersion curves is almost zero. In this case, the group velocity of the wave also approaches zero, indicating that the waves stop propagating and are contained to a confined region，which is consistent with the typical characteristics induced by local resonances. Representative mode shapes are depicted in Fig. 6.3. For the mode indicated by A, the vibration mainly concentrates on the ABH part with negligible motion in the uniform part of the cell. This can be attributed to the unique energy focalization feature of the ABH phenomenon. The gradual thickness changes in the ABH indentation produce strong energy focalization as a result of the gradual

slowing-down of the incoming wave speed toward the indentation center. This is manifested by a compression of the bending waves with a reducing wavelength and increasing vibration amplitude. As a result, this highly dynamic region generates energetic locally resonant modes which are responsible for the band gaps in the low frequency region, similar to the case of conventional ABH configurations [68]. Moreover, the ABH part acts as continuous local resonators with multiple degrees of freedoms, thus generating multiple locally resonant and broad bandgaps, different from the conventional narrow local band gaps induced by single-degree-of-freedom spring mass resonators. However, the local resonance effect is gradually impaired when the uniform part is activated as the frequency increases, exemplified by modes B and C shown in Fig. 6.3. As a result, the band gaps become narrower at higher frequencies, typically with the normalized bandwidth below 10% (Fig. 6.2).

To further enlarge and extend the band gaps to the mid-to-high frequency region, a strengthening stud of length $\Delta l = 0.01\,\mathrm{m}$ is added as sketched in Fig. 6.1 (b). The corresponding band structures are also given in Fig. 6.2 in solid lines for comparison with the case without the stud ($\Delta l = 0$). As can be seen, whilst retaining the band gaps at low frequencies, nearly all the mid-to-high frequency ranges (typically when $f_R > 1$) are covered by wide and flat band gaps, with normalized bandwidth ranging from 15% to 32%. The displacement field of the selected modes in Fig. 6.3 is similar to the case without the studs; namely, ABH-induced local resonances dominate the low frequency region (see mode D) but are weakened at mid-to-high frequencies (see

135

modes E and F). The difference is that the strengthening stud causes a large impedance mismatch with the thin ABH indentation tip, which ensures the generation of the Bragg scattering at mid-to-high frequencies. Owing to the strong energy concentration within the indentation area, high intensity waves are reflected with an accelerating velocity (due to the increase in the structural thickness this time) when reaching the studs. The combination of local resonance and Bragg scattering effect produces these broad band gaps. In practice, the large deformation within the ABH indentation may introduce nonlinear effects, which can generate the coupling between the linear eigenmodes and the energy transfer from low frequencies to high frequencies [66]. It can be expected that the high frequency band gaps could be enhanced because of the enhanced energy focalization and subsequently stronger interference created by the connecting studs.
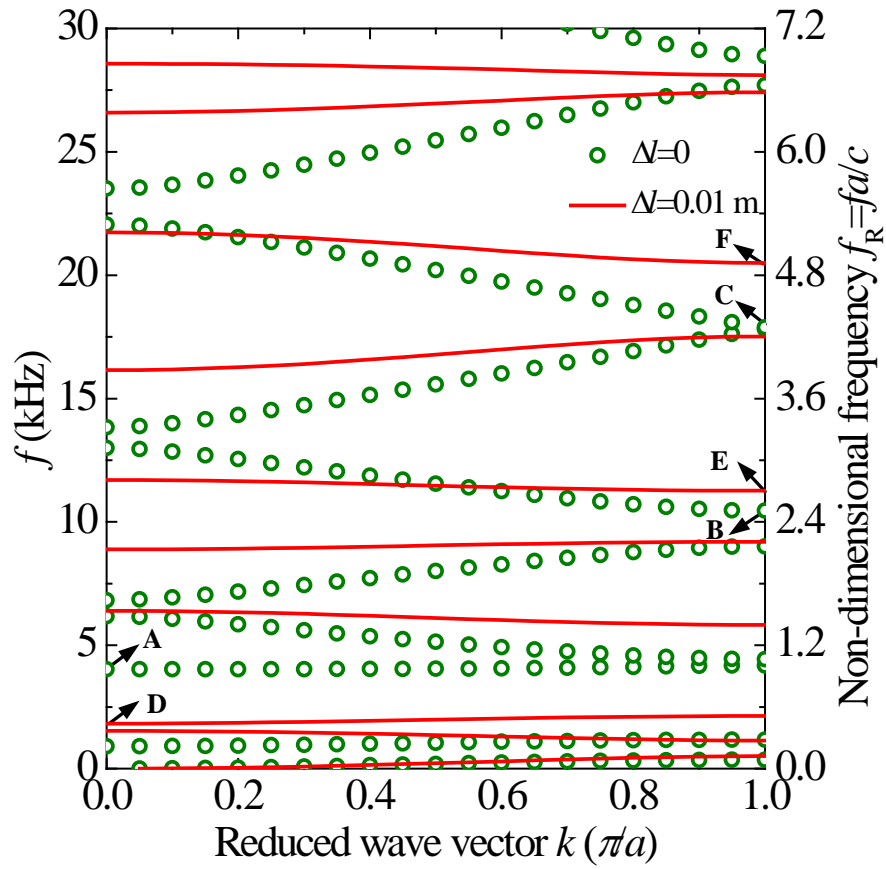
Fig. 6.2 Band structures for the phononic beams with ABH cells. Circles: without strengthening studs ($\Delta l = 0$); lines: with studs ($\Delta l = 0.01$m).
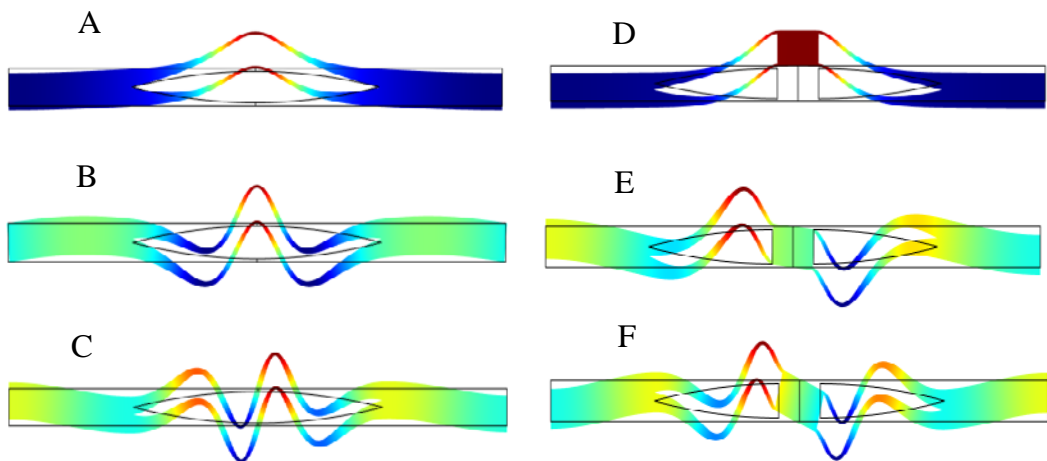
Fig. 6.3 Displacement field of typical modes marked by A-F in the band structure

curves in Fig. 6.2

6.3 Parameters analyses

In views of performance tuning or eventually optimization, the influence of the length Δl on the band structures is investigated first. Figure 6.4 plots the normalized band gaps for different normalized stud lengths $\Delta l / a$. It can be seen that the band gaps in the mid-to-high frequency range are drastically enlarged with even an extremely short stud length ($\Delta l / a = 1/60$ for example). Further increasing $\Delta l / a$ would allow the tuning of the band gaps, in both their central frequency and the associated bandwidth. It can be seen that when $\Delta l / a = 1/4$, a significant portion of the frequency range is filled with band gaps. To quantify the frequency coverage of the band gaps, the ratio between the sum of the bandwidth of all band gaps, $\sum \Delta f$, and the entire normalized frequency range, f_s, is calculated, with results compared in Fig. 6.5 for different normalized stud lengths. It confirms again that the addition of the stud, albeit very short, brings about immediate benefit to the enlargement of the band gaps. Further increasing the stud length, although still beneficial, only offers gradual improvement.
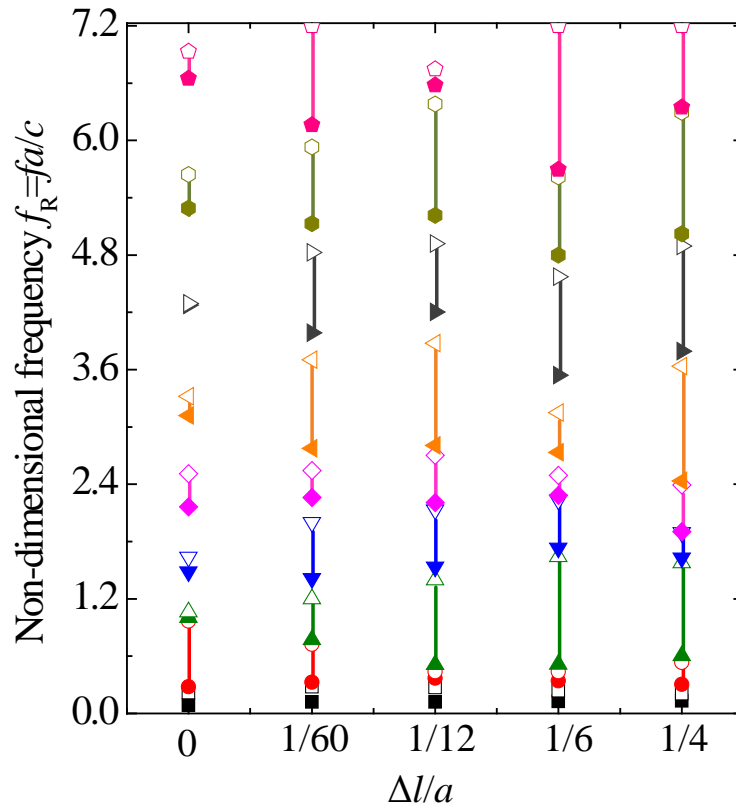
Fig. 6.4 Band gaps *vs.* normalized stud length $\Delta l / a$. Solid and open symbols denote the lower and upper boundaries of the band gaps, respectively; lines between symbols represent the bandwidth of different band gaps (identified using different colors and symbols)
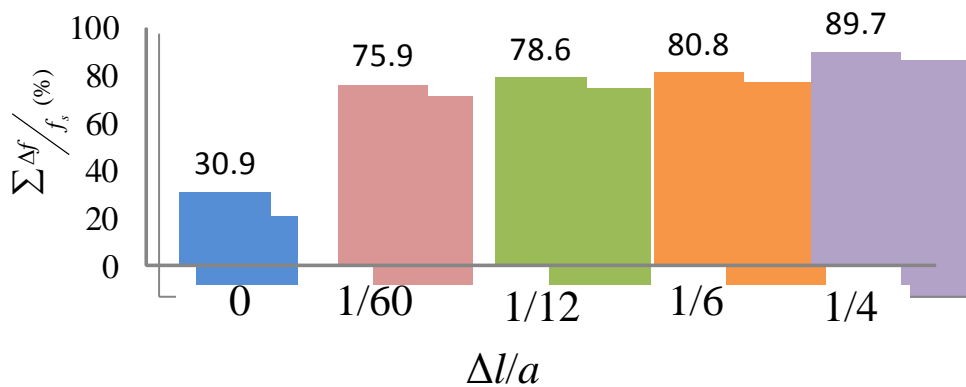
Fig. 6.5 Ratio between the sum of bandwidths of band gaps and the entire frequency

range $\sum\Delta f \big/ f_s$, where f_s equals to 7.2 in the present study.

Since the locally resonant and Bragg scattering effect are closely related to the ABH effect as mentioned above, it is important to investigate how the ABH parameters affect the band gaps so that the structures can be tactically designed to create band gaps pertinent to particular applications. Figure 6.6 shows the effect of the taper power index m on the band gaps. As can be seen, increasing m would lower the band gaps overall into lower frequency bands. Meanwhile, because of the positive effect of m on the ABH effect, the bandwidth of band gaps at low frequency are broader due to the improved local resonant of the ABH part. The enhanced energy focalization also helps to enhance the Bragg scattering effect at mid-high frequency. Therefore, the frequency coverage of band gaps is also increased. Keep in mind, however, that the taper power index m cannot be extremely large at the expenses of violating the smoothness criterion, which will generate additional reflection and thus reduce the ABH effect and the accompanying band gaps.
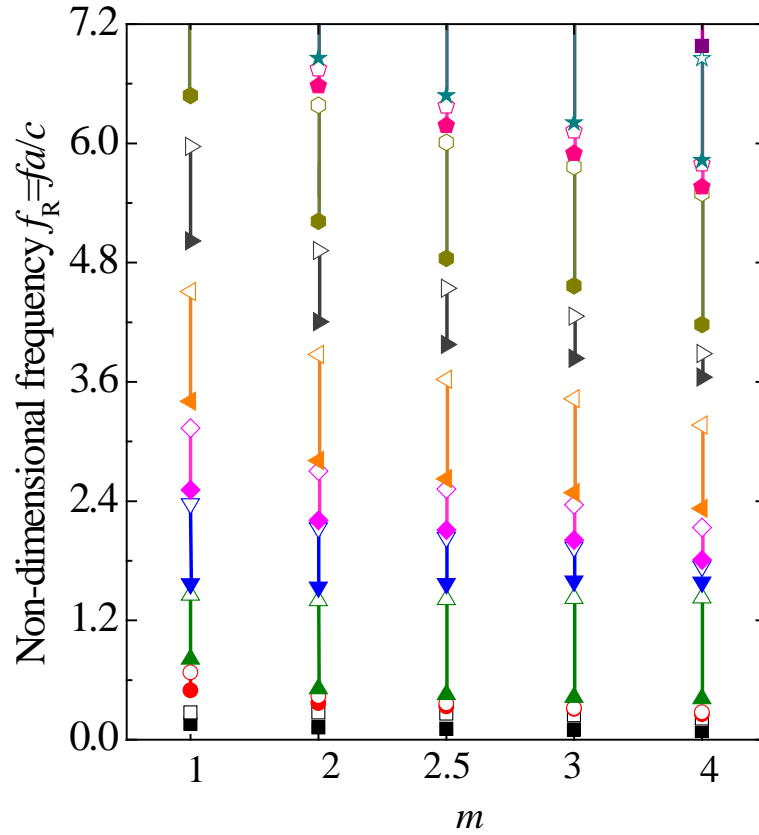
Fig. 6.6 Effect of taper power *m* on band gaps. Solid and open symbols denote the lower and upper boundaries of the band gaps, respectively; lines between symbols represent the bandwidth of different band gaps (identified using different colors and symbols)

Figure 6.7 shows the effect of the normalized truncation thickness h_0/h_b on the band gaps. It can be seen that reducing the truncation thickness not only lowers the band gaps overall but also significantly increases the frequency coverage of the band gaps. As we know, when the truncation thickness is approaching to zero, there will be no wave reflection and the ABH part would be an ideal absorber. Therefore, the ABH part with a reduced truncation thickness would act as ideal local resonators, thus

generating broader low frequency band gaps. Meanwhile, the reduced truncation

thickness would also lead to larger impedance mismatch with the strengthening stud.

Consequently, Bragg scattering can further be strengthened to create even broader

band gaps at the mid-to-high frequencies.
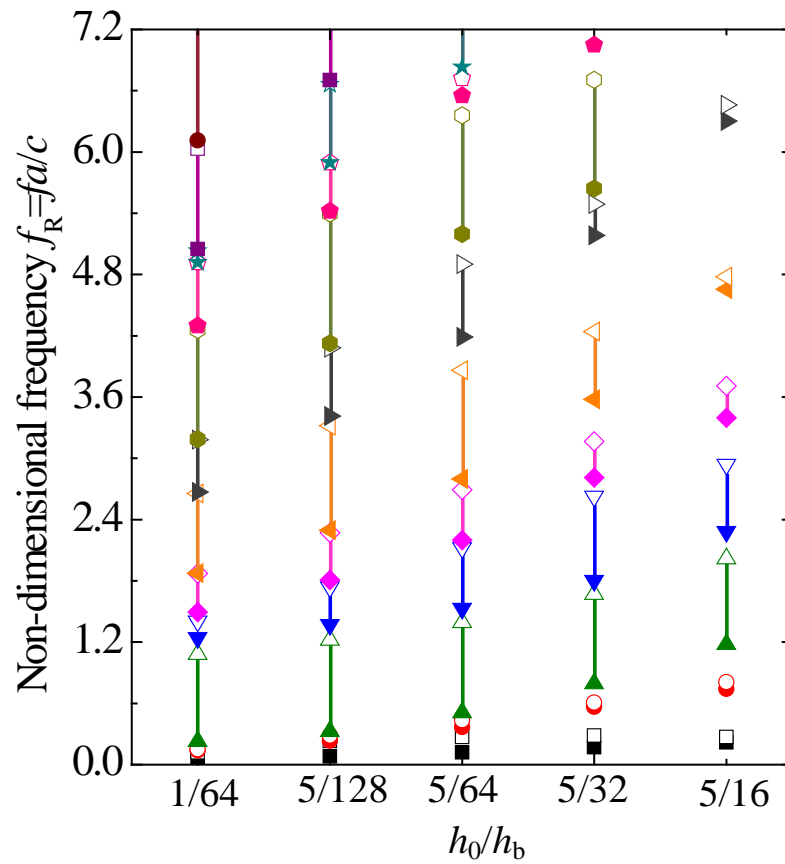
Fig. 6.7 Effect of normalized truncation thickness h_0 / h_b on band gaps. Solid and open

symbols denote the lower and upper boundaries of the band gaps, respectively; lines

between symbols represent the bandwidth of different band gaps (identified using

different colors and symbols)

The effect of the lattice constant a on the band gaps is also shown in Fig. 6.8.

The overall normalized frequency coverage of the band gaps shows little difference when different lattice constants are used. However, both the upper and lower frequencies of each band gap increase systematically. As stated in Chapter 5, the frequency in the vertical axis is normalized with the wave length (c/a), positively related with the lattice constant a. Therefore, the actual frequency decreases with the increase of the lattice constant. To obtain band gaps at lower frequencies, a larger value of both the lattice constant and the taper power m but a smaller truncation thickness should be used.
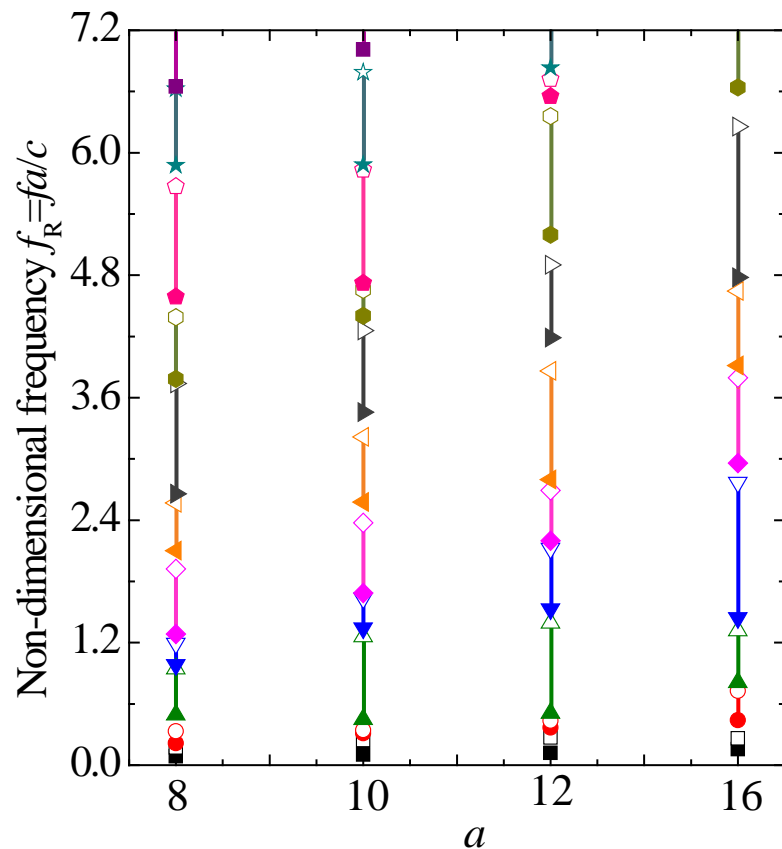
Fig. 6.8 Effect of lattice constant a on band gaps. Solid and open symbols denote the lower and upper boundaries of the band gaps, respectively; lines between symbols

represent the bandwidth of different band gaps (identified using different colors and symbols)

As an example, Fig. 6.9 shows the band structures of a phononic beam with the same geometrical parameters as those used in Fig. 6.2, but with the truncation thickness of the ABH indentation being reduced by half, *i.e.* $h_0 = 0.00025\,\mathrm{m}$. As can be seen, flat and broad band gaps cover nearly the entire frequency range, owing to the enhanced effect from both local resonances and Bragg scattering. The bandwidth percentage $\sum \Delta f \big/ f_s$ increases up to 92%, as compared to 78.6% when $h_0 = 0.0005\,\mathrm{m}$.
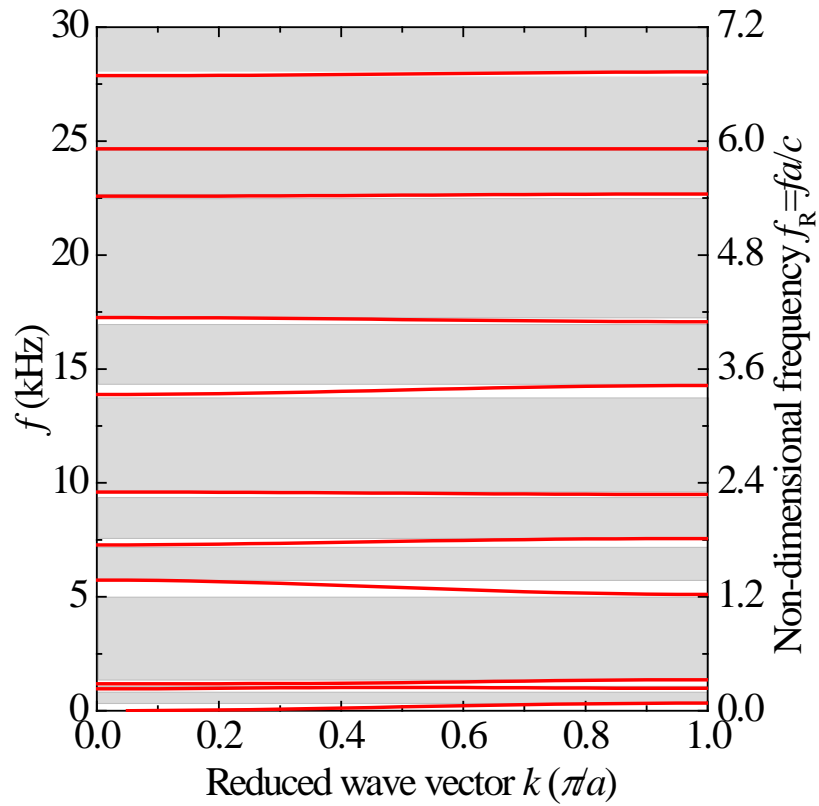
Fig. 6.9 Band structures for the phononic beams with $h_0 = 0.00025\,\mathrm{m}$. All other

geometrical parameters are the same as those used in Fig. 2 ($\Delta l = 0.01\text{m}$). The grey areas donate band gaps.

In viewing of the ultrawide band gaps generated by the proposed beams with double-leaf ABH indentations, we examine whether similar phononic beams with inside carved by uniform thickness indentations, as shown in Fig. 6.10, can also produce similar ultrawide band gaps. To be comparable, the areas of indentations and other geometrical parameters in both phononic beams are kept the same. Therefore, when the truncation thickness h_0 equals to 0.0005 m in the ABH case, the thickness h_u of the uniform indentations should be 0.0014 m. The band structures of the two cases are compared in Fig. 6.11. It can be seen that, although the beams with uniform indentations can also generate multiple band gaps in the frequency ranges, the band gaps are quite narrow compared with those existing in the proposed beams with ABH indentations, especially at mid-high frequencies.
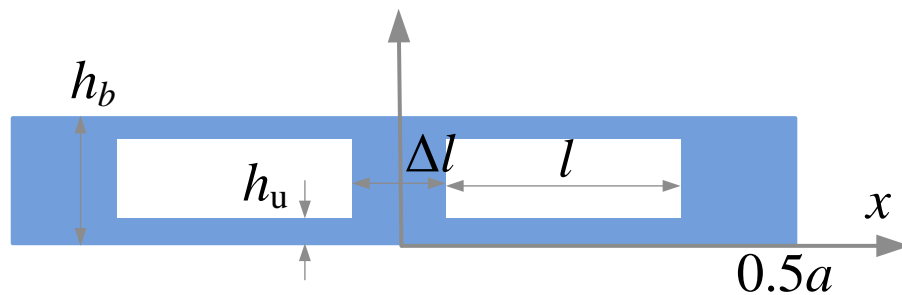
Fig. 6.10 Unit cell of the phononic beams with inside carved by uniform thickness h_u with a length l.

To quantify the difference between the two cases, Fig. 6.12 compares the normalized bandwidth of the first band gap and the entire bandwidth coverage. The results show that, regardless of the bandwidth of the first band gap or the whole bandwidth coverage, the performance of the proposed beams with ABH indentations overwhelmingly outperforms that of the beams with uniform indentations. This is understandable because at low frequencies, the energy focalization from the ABH effect helps to generate wider locally resonant band gaps; at mid-high frequencies, the Bragg scattering effect can be enhanced by the energy focalization from the ABH effect on one hand, and by the larger impedance mismatch due to the thinner truncation thickness h_0 compared with h_u on the other hand. Therefore, the proposed beams with double-leaf ABH indentations can achieve much wider band gaps over the whole frequency range in comparison with the beams with uniform indentations.
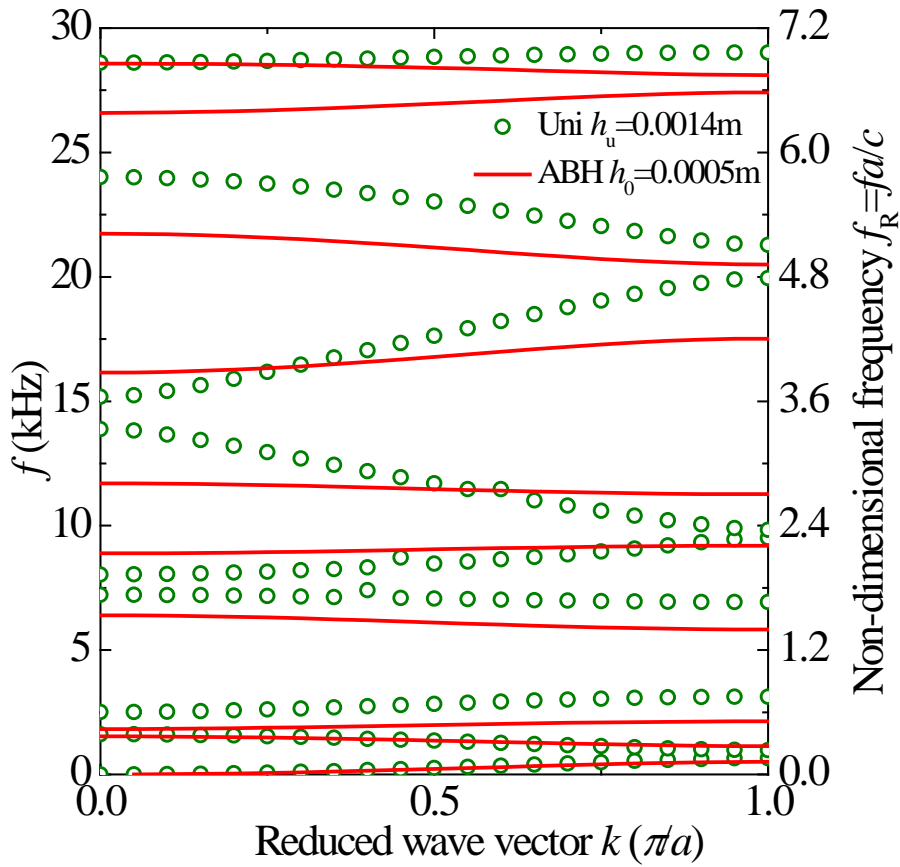
Fig. 6.11 Band structure comparisons between the phononic beams with ABH indentations and the phononic beams with uniform indentations. The areas of the indentations in the two cases are kept the same.

6.4 Experimental validations

Experiments were carried out to confirm and validate the numerically observed band structures on one hand, and to investigate the possibility of using a small number of ABH cells for vibration energy attenuation on the other hand. To this end,

four finite beams consisting of one and three cells respectively with the same geometrical and material parameters used in Fig. 6.2 were fabricated. A uniform beam with the same length of three cells was also included as a reference, as shown in Fig. 6.13(a). The width of all beams is the same (0.01m). Flexural vibration responses of the beams when subjected to a unit point excitation force were analysed. The experiment setup is shown in Fig. 6.13(b). The beams were supported with two thin strings to mimic free boundaries. A periodic chirp signal from 0 to 20 kHz was applied at one end of the beams through an electromagnetic shaker, with the excitation force measured by a force transducer (B&K 8200) and amplified by a charge amplifier (B&K 2635). A Polytec scanning laser vibrometer was used to scan the whole beams for the response measurement.
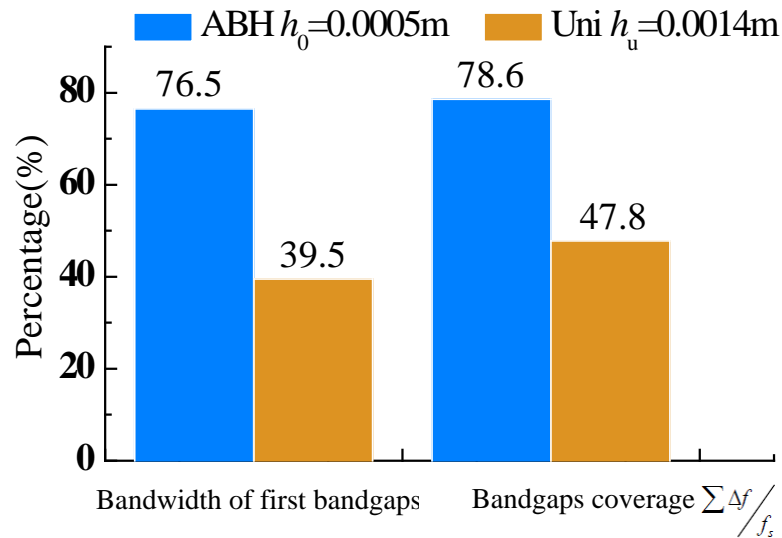
Fig. 6.12 Comparisons of the normalized bandwidths of the first band gap and the band gap coverage between the phononic beams with ABH indentations and the

phononic beams with uniform indentations.

(a)

(b)
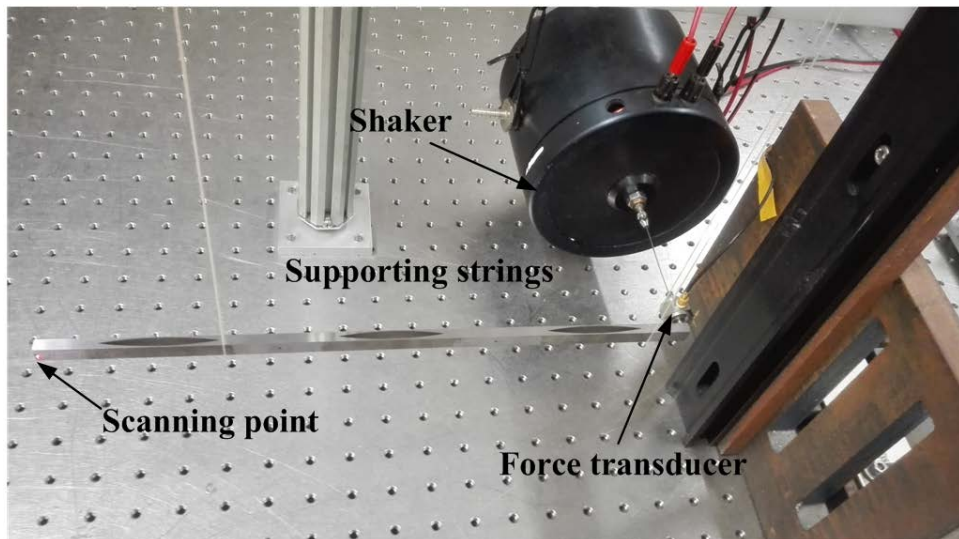
Fig. 6.13 (a) a uniform beam and four ABH beams containing one and three cells respectively, with the same material and geometrical parameters as those used in Fig. 6.2; (b) Experiment setup.

For reference, the displacement transmission, defined as $20\log w_{out}/w_{in}$ (w_{out} and w_{in} are respectively the output and input of displacement), from experiments and numerical simulations of the uniform beam is given in Fig. 6.14. The experimental results agree well with the numerical results in terms of both the resonant frequencies

and the amplitudes. Only few additional peaks are observed because of the torsional

waves, induced by the slight deviation of excitation force from the central axis of the

beam. Lacking of particular treatment, the uniform beam exhibits no particular wave

filtering ability, exemplified by the transmission almost larger than zero.
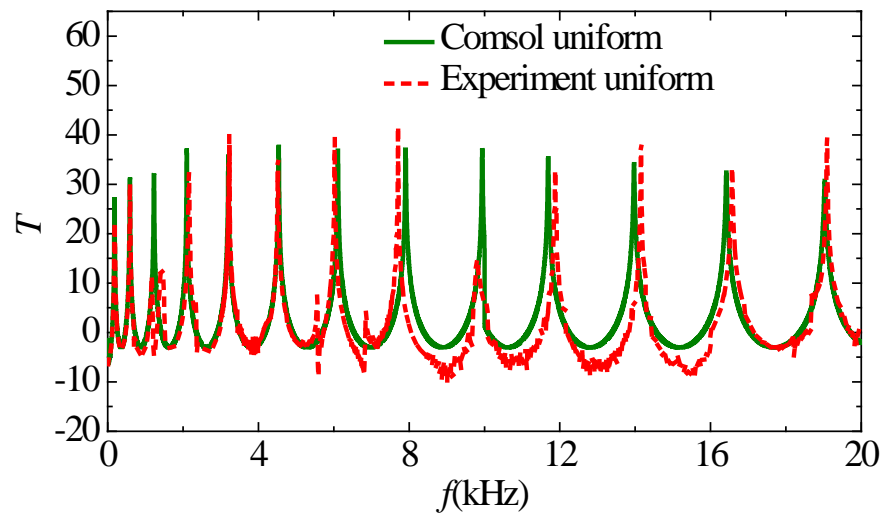
Fig. 6.14 Displacement transmission comparison between the numerical results (grey

and dark solid lines) and experiment results (green dashed and red dotted lines) for

the uniform beam.

Figure 6.15 shows the displacement transmission comparison between the beam

without the stud $\Delta l = 0$ and the beam with stud $\Delta l = 0.01\,\mathrm{m}$ when one cell is included.

The experimental results agree reasonably well with the numerical results with only a

few additional spikes due to the same reason explained above. For the beam without

stud as shown in Fig. 6.15(a), two narrow attenuation gaps, albeit very narrow, exist

below 5 kHz, which roughly match the band gaps illustrated in Fig. 6.2. When a stud

is added, the displacement transmission in Fig. 6.15(b) shows extremely broader attenuation gaps from 3 kHz to 16 kHz with an attenuation level amounting to 20 dB, which also roughly agree with the predicted band gaps. Meanwhile, the attenuation gaps observed in the beams with only one cell confirm that the band gaps are induced by locally resonant effect, which mainly depends on the local resonator properties rather than the periodic properties.
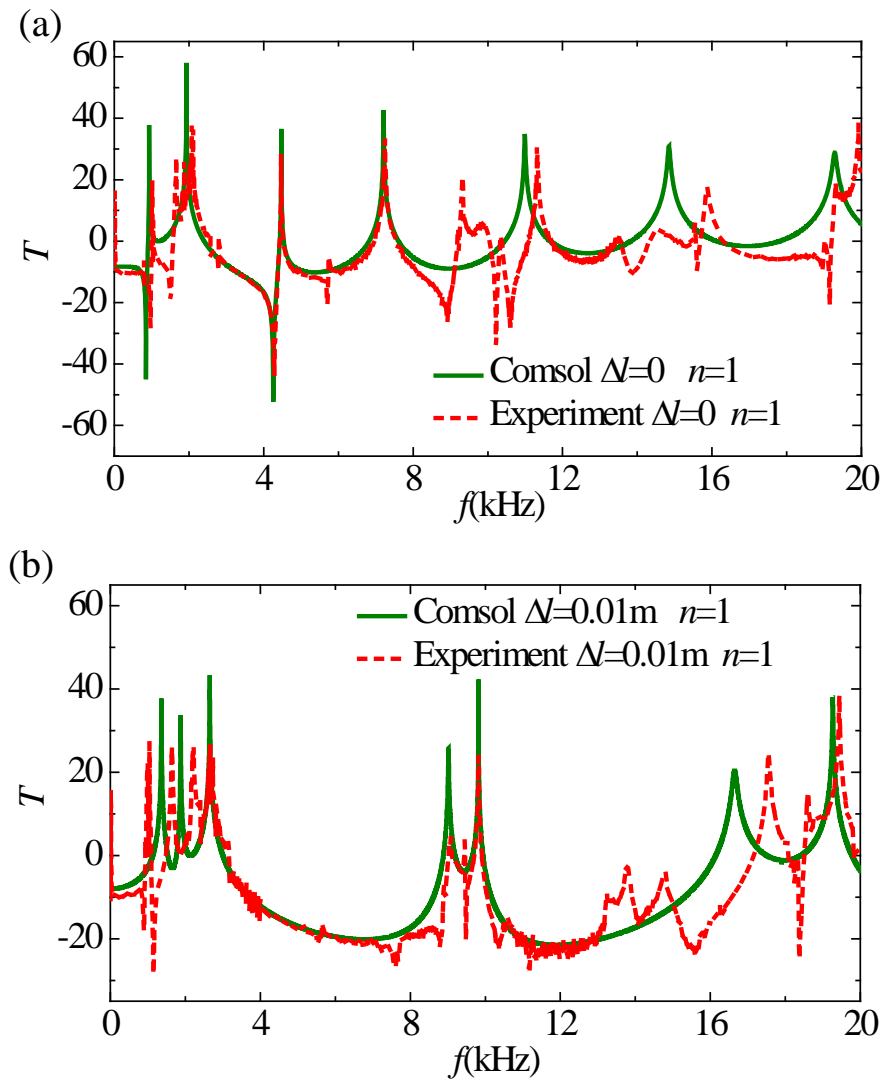
Fig. 6.15 Displacement transmission comparison between the numerical results

(green lines) and experiment results (red dotted lines): (a) the beam with $\Delta l = 0$ and (b) the beam with $\Delta l = 0.01\,\mathrm{m}$ when one cell is included.

When three cells are incorporated, the displacement transmission comparison is again shown in Fig. 6.16. Once again, experimental results agree well with numerical ones in terms of both the location and width of the attenuation bands. Differences in the deep trough areas are due to the torsional waves as stated before, which emerge when flexural waves became significantly weak within the band gaps. For the same reason, signals became noisier within the attenuation gaps. From Fig. 6.16(a), we can see several obvious attenuation gaps below 5 kHz, which are in good agreement with the observed band gaps in Fig. 6.2. Without the strengthening studs, the attenuation gaps barely exist apart from the low frequency region. When three strengthening studs with a length $\Delta l = 0.01\,\mathrm{m}$ were added, Fig. 6.16(b) shows several attenuation gaps, which agree with the numerically predicted band gaps shown in Fig. 6.2. These attenuation bands cover a very large portion of the frequency range, generating transmission attenuation up to nearly 60 dB. With three cells, the attenuation has been significantly strengthened compared with the case with only cell. It is relevant to note that, as a side benefit of the ABH effect, the levels of the transmission peaks are also reduced compared with the uniform beam at mid-to-high frequencies.
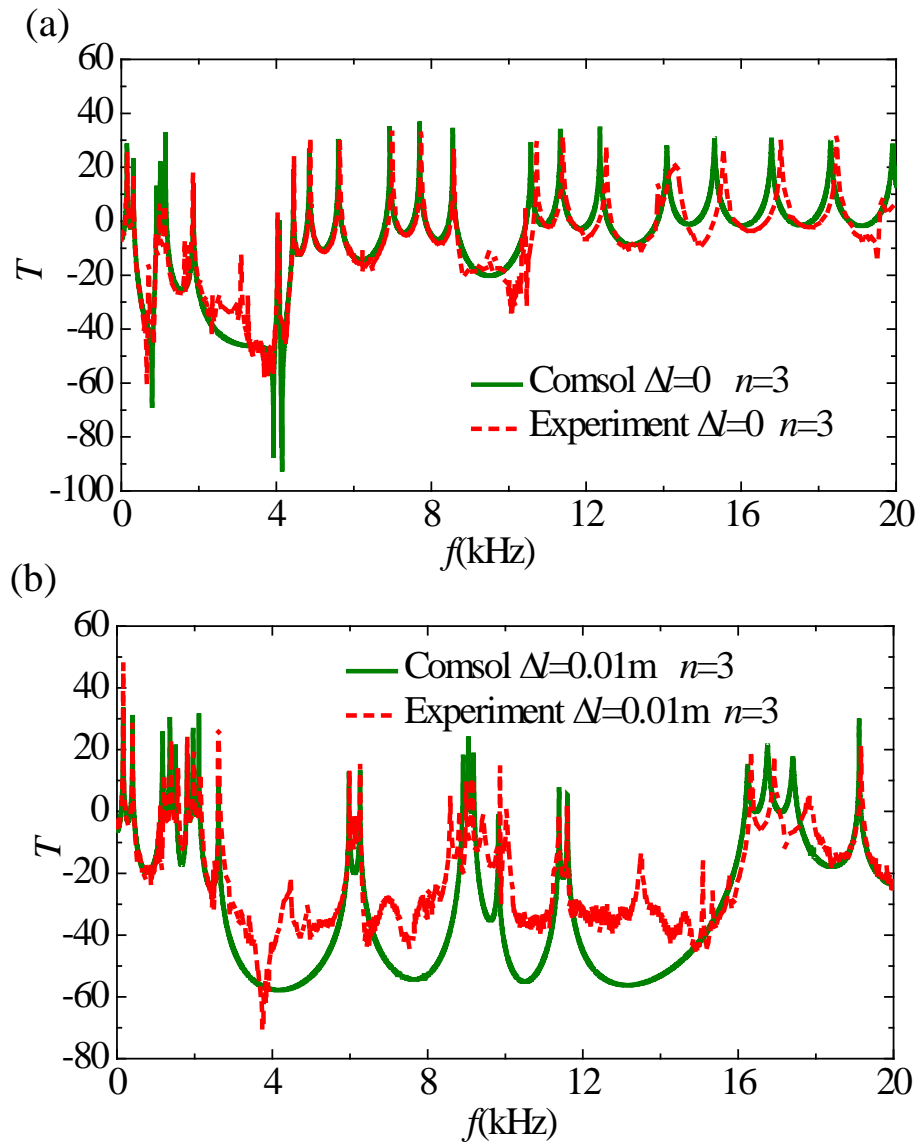
Fig. 6.16 Displacement transmission comparison between the numerical results
(green lines) and experiment results (red dotted lines): (a) the beam with $\Delta l = 0$ and
(b) the beam with $\Delta l = 0.01\,\mathrm{m}$ when three cells are included.

Above comparisons show that, with only a few cells, the proposed phononic
beams exhibit remarkable wave attenuation ability. The displacement distribution at
two chosen frequencies within the attenuation bands (in the three-cell case) are

plotted in Fig. 6.17 to further reveal the vibration attenuation effect. For both beams with ABHs, the measured displacement matches well with the numerically calculated one. It can be seen that the vibration is drastically reduced as the wave propagates through cells in both cases. With the strengthening studs, the vibration reduction is more significant compared with its counterpart without studs, in agreement with numerical analyses.
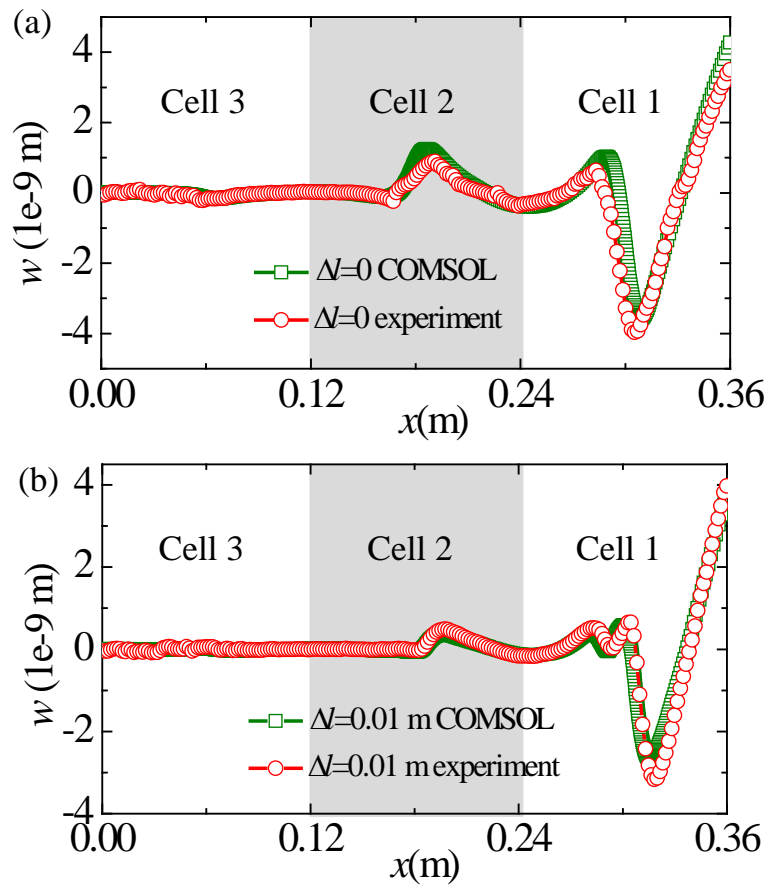
Fig. 6.17 Displacement distribution of (a) the beam with $\Delta l = 0$ for f=3506 Hz and (b) the beam with $\Delta l = 0.01\,\mathrm{m}$ for f=4280 Hz. Different highlighted-color areas present different cells with cell 1 nearest to the excitation end.

6.5 Summary

In this Chapter, we propose a new type of phononic beams with embedded double-leaf ABH indentations. The band structures and their generation mechanism are analyzed and compared through finite element analyses. Key parameters related to the ABH effect and the lengths of the strengthening studs are investigated for the possible tuning of the band gaps in terms of both bandwidth and distribution. Experiments are conducted to confirm and validate the numerically predicted phenomena. The main conclusions are summarized as follows.

The proposed phononic beams with double-leaf acoustic black hole (ABH) indentation carved inside a uniform unit cell are shown to exhibit remarkable band gap properties. The unique energy focalization feature of the ABH effect offers the dual benefit: effective and energetic local resonant modes at relatively low frequencies and intensive wave interferences to generate Bragg scattering when the strengthening studs are added. As a result, the two effects are combined to produce ultrawide band gaps. The impedance mismatch between the stud and the thin ABH indentation, responsible for the generation of the Bragg scattering, can be tuned by changing various parameters related to the ABH indentations and the strengthening studs. Increasing the length of the stud or reducing the residual thickness of ABH indentation allows a significant increase in the gap bandwidth, which can cover nearly 90% of the entire frequency range of interest with realistic geometric and

material parameters. The numerically predicted phenomena are confirmed by experiments, which further show that, with a few cells, the proposed phnononic beams warrant considerable vibration attenuation.

As to the structure itself, the proposed phononic beams, through embedding tapered profiles inside the uniform beams, ensure structural integrity on the lattice surface whilst improving the inherent structural stiffness/strength weakness of conventional ABH structures in terms of load-bearing capability. Compared with most conventional PCs using add-on resonators or optimized complex geometries, the proposed structures are self-also self-contained and easier to fabricate, offering great potentials for various applications.

Chapter 7 Conclusions and Future Suggestions

This thesis covers the modeling, analyses and implementations of the Acoustic Black Hole (ABH) effect for vibration control applications. Along with Finite element analyses, studies are mainly based on a novel wavelet-decomposed and energy-based model to investigate various ABH features and the effect of damping layers using realistic ABH-featured beams. The main conclusions arising from this work can be summarized as follows.

By using the Mexico Hat Wavelets (MHW) for the decomposition of the displacement functions under Rayleigh-Ritz framework, the developed semi-analytical model guarantees a high simulation efficacy in characterizing the wave fluctuation feature of the ABH effect, as verified by both the FEM and experimental results. This is attributed to the unique features of the MHW in characterizing both highly localized and distributed waveforms as a result of flexible scaling and translation.

The energy based nature of the model allows the consideration of the full coupling between the damping layers and the host structures. Numerical results reveal that the stiffness of the damping layers plays a more important role than the mass does, which should be apprehended in the model; while the effect of the added mass also needs particular attention when the thickness of damping layers is considerable to that of the ABH wedge around the tip area. This conclusion suggests

that an optimal damping layer thickness should exist for each particular system configuration in order to strike a balance between the desired damping enhancement and the possible adverse coupling-induced reduction in the ABH effect.

The ABH effect enables a high energy density concentration in the vicinity of the ABH wedge tip (or indentation), somehow compromised by the inevitable residual thickness. Covering the ABH part with damping layers can compensate for the adverse effect of truncation and the proposed model provides an efficient tool to optimize the location and shape of the damping layers to achieve maximum ABH effect. Generally speaking, damping layers are preferable to be applied near the wedge tip as frequency increases.

The developed model deals with a realistic beam with finite size and uncovers the loss of the ABH effect, as opposed to the widely reported broadband phenomenon above the cut-on frequency in semi-infinite ABH structures. When this happens, the energy focalization capability in the tapered ABH region is significantly impaired and the vibration energy mainly concentrates within the uniform part of the beam delimited by the excitation force. The presence of the mechanical excitation introduces an impedance discontinuity and thus creates multiple wave reflections between the structure boundary and the excitation point, forming standing waves and local resonances in the uniform part of the beam at certain frequency bands. The failure frequencies can be predicted by calculating the local resonance frequencies of the beam portion delimited and pinned by the excitation point.

Due to its modular and energy-based nature, the developed model also offers a general platform for further including other control or energy harvesting elements to guide the design of ABH structures for various applications. Meanwhile, compared with FEM, it is also more flexible for parametric studies and system optimizations to achieve better ABH structural designs.

The ultimate pursuit of extremely thin wedge tips to maximum the ABH effect is practically unrealistic. Therefore, on the premise of the minimum achievable truncation thickness by currently available manufacturing technology, a modified ABH thickness profile and the use of an extended platform are investigated to maximize the ABH effect. It is shown that the modified thickness profile can significantly improve the ABH effect in terms of vibration reduction of the uniform part of the beam, enhanced energy distribution in the ABH part and the increased system loss factor, especially for a larger power parameter m and smaller truncation thickness. The extended platform results in an overall increase in the system damping above the characteristic frequency, as well as an appreciable shift of the ABH effect towards low frequency. In particular, it can significantly increase the first peak of the energy ratio and shift it to lower frequency, providing the possibility of catering ABH effect for lower frequency applications. This phenomenon, however, strongly depends on the modal behavior of the whole system, which needs meticulous analyses by the developed model to optimize the ABH performance for particular applications.

To further increase the low frequency ABH effect, multiple ABH elements are shown to be preferable to the single ABH configuration for a given allowable ABH space. For particular low frequency bands, the number of ABH elements should be carefully chosen by using the developed model because the increased damping effect are modal dependent. However, for higher frequency, placing one ABH element rather than multiple ABH elements is beneficial for more effective damping. Besides, the layout of the ABH elements shows little effect on the overall ABH effect.

In addition to the enhancement of system damping, multiple ABHs also create broadband attenuation bands and wave suppression phenomena at low frequencies. Through extension to infinite periodic structures, the developed wavelet-decomposed energy model is shown to provide an efficient and flexible means to predict, and eventually optimize the band structure of an infinite beam based on only a unit cell with periodic boundary conditions of displacement and rotational slope. Analyses confirm that the attenuation bands correspond exactly to the band gaps of the infinite structures with the same ABH elements. These band gaps are attributed to the local resonances of the ABH elements as a result of the strong resonating dynamics of the ABH region. Therefore, increasing the taper power index m within the smoothness criteria, or reducing the truncation thickness h_0 within the allowable practical range, would help generate broader and lower-frequency band gaps. Meanwhile, extending platform can also lower the band gap frequencies. Contrary to the conventional resonant lattices, only a very few ABH elements are needed to produce broad

attenuation gaps with no add-on resonator attachment or multiple geometric or material discontinuities.

For practical implementations, the above mentioned conventional ABH structures may be hampered by the structural strength weakness resulting from the extremely thin truncation thickness and also by limited attenuation bands only at relatively low frequency. To tackle the problem, a new type of phononic beams carved inside with two double-leaf ABH indentations is proposed. By incorporating the local resonance of the ABH indentations and Bragg scattering effects generated by a strengthening stud connecting the two branches of the ABH indentations, ultrawide band gaps are achieved. These band gaps can be tuned by adjusting the length of the stud and the ABH parameters to cover over 90% of the entire frequency range of interest. Meanwhile, experiments results show that with only three cells, the proposed phononic beams allow considerable vibration energy attenuation within an ultra-broad frequency range including the low frequency range which conventional PCs can hardly reach. These appealing features may offer great potential for applications such as vibration isolation and wave filtering in beam structures.

Based on the work presented in this thesis, some future suggestions are proposed as follows.

1) The proposed semi-analytical and numerical model only deals with 1D beam structures with a thickness profile symmetrical with respect to the mid-line due to the Euler-Bernoulli beam assumption. Exploring models which are not limited by these

161

assumptions in both 1D and 2D structures is necessary to investigate more realistic structures.

2) The phononic beams with ABH indentations proposed in this thesis demonstrate their high ability in vibration isolation and wave filtering. It is also of great interest to study and design 2D plate structures containing ABH feature to achieve possible band gaps, considering the wide application of plate structures in transportation industry, where light-weight and low vibration and noise is of paramount importance. It is understandable that the wave travel paths in plate are more complex than that in a beam and obtaining absolute band gaps might be difficult. However, achieving band gaps for particular wave modes might still be possible and meaningful.

3) The exploration of the ABH effect for noise control applications is also important and technically challenging. Physically, the reduction in the structural thickness can slow down the flexural wave from supersonic to subsonic. This may significantly change the sound radiation efficiency of the overall structure and offers possibilities for better structural design towards noise reduction. Meanwhile, the sound radiation problem becomes particularly interesting when band gaps emerge, specially near the critical frequency. Therefore, revisiting 2D or even more complex structures in an acoustic perspective adds a completely new dimension to the topic of ABH, which is technically challenging and practically relevant to a wide range of engineering problems for noise control applications.

162

Appendix A: Displacement expression considering additional boundary conditions Eqs. (5.12) and (5.13)

Considering the additional boundary condition Eq. (5.12), we can get

$$a_{n-2} = \sum_{i=1}^{n-3} \lambda\lambda_i a_i$$

$$w(x,t) = \sum_{i=1}^{n-3} \left\{ \begin{array}{l} \varphi_i(x) + \lambda\lambda_i\varphi_{n-2}(x) + \left[\lambda\lambda_i \dfrac{\lambda'_{n-2} - \lambda_{n-2}}{-\lambda'_{n-1} + \lambda_{n-1}} + \dfrac{\lambda'_i - \lambda_i}{-\lambda'_{n-1} + \lambda_{n-1}} \right] \varphi_{n-1}(x) \\[2ex] + \left[\lambda\lambda_i \left[\dfrac{\lambda'_{n-2} - \lambda_{n-2}}{\lambda'_{n-1} - \lambda_{n-1}} \lambda_{n-1} - \lambda_{n-2} \right] + \dfrac{\lambda'_i - \lambda_i}{\lambda'_{n-1} - \lambda_{n-1}} \lambda_{n-1} - \lambda_i \right] \varphi_n(x) \end{array} \right\} a_i$$

where $\quad \lambda\lambda_i = \dfrac{\dfrac{\lambda''_i - \lambda_i}{\lambda''_{n-1} - \lambda_{n-1}} - \dfrac{\lambda'_i - \lambda_i}{\lambda'_{n-1} - \lambda_{n-1}}}{-\dfrac{\lambda''_{n-2} - \lambda_{n-2}}{\lambda''_{n-1} - \lambda_{n-1}} + \dfrac{\lambda'_{n-2} - \lambda_{n-2}}{\lambda'_{n-1} - \lambda_{n-1}}}$

With the additional boundary condition Eq. (5.13), the displacement can be repressed by

$$a_{n-3} = \sum_{i=1}^{n-4} \beta_i a_i$$

$$w(x,t) = \sum_{i=1}^{n-4} \left\{ \begin{array}{l} \varphi_i(x) + \beta_i \varphi_{n-3}(x) + \left[\lambda\lambda_i + \beta_i \lambda\lambda_{n-3} \right] \varphi_{n-2}(x) \\[2mm] + \left[\begin{array}{l} \lambda\lambda_i \dfrac{\lambda'_{n-2} - \lambda_{n-2}}{-\lambda'_{n-1} + \lambda_{n-1}} + \dfrac{\lambda'_i - \lambda_i}{-\lambda'_{n-1} + \lambda_{n-1}} \\[3mm] + \beta_i \left(\lambda\lambda_i \dfrac{\lambda'_{n-2} - \lambda_{n-2}}{-\lambda'_{n-1} + \lambda_{n-1}} + \dfrac{\lambda'_{n-3} - \lambda_{n-3}}{-\lambda'_{n-1} + \lambda_{n-1}} \right) \end{array} \right] \varphi_{n-1}(x) \\[6mm] + \left\{ \begin{array}{l} \lambda\lambda_i \left(\dfrac{\lambda'_{n-2} - \lambda_{n-2}}{\lambda'_{n-1} - \lambda_{n-1}} \lambda_{n-1} - \lambda_{n-2} \right) + \dfrac{\lambda'_i - \lambda_i}{\lambda'_{n-1} - \lambda_{n-1}} \lambda_{n-1} - \lambda_i \\[3mm] + \beta_i \left[\lambda\lambda_{n-3} \left(\dfrac{\lambda'_{n-2} - \lambda_{n-2}}{\lambda'_{n-1} - \lambda_{n-1}} \lambda_{n-1} - \lambda_{n-2} \right) + \dfrac{\lambda'_{n-3} - \lambda_{n-3}}{\lambda'_{n-1} - \lambda_{n-1}} \lambda_{n-1} - \lambda_{n-3} \right] \end{array} \right\} \varphi_n(x) \end{array} \right\} a_i$$

where
$$\beta_i = \frac{\dfrac{\lambda'''_i - \lambda_i}{\lambda'''_{n-1} - \lambda_{n-1}} + \lambda\lambda_i \dfrac{\lambda'''_{n-2} - \lambda_{n-2}}{\lambda'''_{n-1} - \lambda_{n-1}} - \lambda\lambda_i \dfrac{\lambda'_{n-2} - \lambda_{n-2}}{\lambda'_{n-1} - \lambda_{n-1}} - \dfrac{\lambda'_i - \lambda_i}{\lambda'_{n-1} - \lambda_{n-1}}}{-\dfrac{\lambda'''_{n-3} - \lambda_{n-3}}{\lambda'''_{n-1} - \lambda_{n-1}} - \lambda\lambda_{n-3} \dfrac{\lambda'''_{n-2} - \lambda_{n-2}}{\lambda'''_{n-1} - \lambda_{n-1}} + \lambda\lambda_{n-3} \dfrac{\lambda'_{n-2} - \lambda_{n-2}}{\lambda'_{n-1} - \lambda_{n-1}} + \dfrac{\lambda'_{n-3} - \lambda_{n-3}}{\lambda'_{n-1} - \lambda_{n-1}}}$$

Reference

[1] D. Ross, E.K., E. Ungar, Damping of plate flexural vibrations by means of viscoelastic laminae. *Structural Damping*, **3**, 44-87 (1959).

[2] C. Vemula, A. Norris, and G. Cody, Attenuation of waves in plates and bars using a graded impedance interface at edges. *Journal of Sound and Vibration*, **196**(1), 107-127 (1996).

[3] R.A. Shelby, D.R. Smith, S. Schultz, Experimental verification of a negative index of refraction. *Science*, **292**(5514), 77-79 (2001).

[4] S. Zhang, Y.S. Park, J. Li, X. Lu, W. Zhang, and X. Zhang, Negative refractive index in chiral metamaterials. *Physical Review Letters*, **102**(2), 023901 (2009).

[5] H. Chen and C.T. Chan, Acoustic cloaking in three dimensions using acoustic metamaterials. *Applied Physics Letters*, **91**(18), 183518 (2007).

[6] C.L. Pekeris, Theory of Propagation of Sound in a Half‑Space of Variable Sound Velocity under Conditions of Formation of a Shadow Zone. *The Journal of the Acoustical Society of America*, **18**(2), 295-315 (1946).

[7] M.A. Mironov, Propagation of flexural wave in a plate whose thickness decreases smoothly to zero in a finite interval. *Soviet Physics- Acoustics*, **34**(3), 318-319 (1988).

[8] V.V. Krylov, Conditions for valixdity of the geometrical-acoustic approximation in application to waves in an acute-angel solid wedge. *Soviet Physics -*

Acoustics, **35**(2), 176-180 (1989).

[9]   V.V. Krylov and A.L. Shuvalov, Propagation of localised flexural vibrations along plate edges described by a power law. *Proceedings of the lnstitute of Acoustics*, **22**(2), 263-270 (2000).

[10] V.V. Krylov, On the velocities of localized vibration modes in immersed solid wedges. *The Journal of the Acoustical Society of America*, **103**(2), 767-770 (1998).

[11] V.V. Krylov, Geometrical-acoustics approach to the description of localized vibrational modes of an elastic solid wedge. *Soviet Physics-Technical Physics*, **35**(2), 137-140 (1990).

[12] V.V. Krylov, and F.J.B.S. Tilman, Acoustic 'black holes' for flexural waves as effective vibration dampers. *Journal of Sound and Vibration*, **274**(3), 605-619 (2004).

[13] V.V. Krylov, Acoustic'black holes' for flexural waves and their potential applications.   (2002).

[14] V.V. Krylov, New type of vibration dampers utilising the effect of acoustic black holes. *Acta Acustica united with Acustica*, **90**(5), 830-837 (2004).

[15] V. Denis, F. Gautier, A. Pelat, and J. Poittevin, Measurement and modelling of the reflection coefficient of an Acoustic Black Hole termination. *Journal of Sound and Vibration*, **349**, 67-79 (2015).

[16] P.A. Feurtado, S.C. Conlon, and F. Semperlotti, A normalized wave number

variation parameter for acoustic black hole design. *The Journal of the Acoustical Society of America*, **136**(2), EL148-152 (2014).

[17] M.R. Shepherd, P.A. Feurtado, and S.C. Conlon, Multi-objective optimization of acoustic black hole vibration absorbers. *The Journal of the Acoustical Society of America*, **140**(3), EL227-EL230 (2016).

[18] V.B. Georgiev, J. Cuenca, F. Gautier, L. Simon, and V.V. Krylov, Damping of structural vibrations in beams and elliptical plates using the acoustic black hole effect. *Journal of Sound and Vibration*, **330**(11), 2497-2508 (2011).

[19] V.B. Georgiev, J. Cuenca, F. Gautier, and L. Simon, Vibration reduction of beams and plates using Acoustic Black Hole effect. *Institute of Noise Control Engineering*, **2010**(6), 5149-5158 (2010).

[20] E.P. Bowyer, D.J. O'Boy, V.V. Krylov, and J.L. Horner, Effect of geometrical and material imperfections on damping flexural vibrations in plates with attached wedges of power law profile. *Applied Acoustics*, **73**(5), 514-523 (2012).

[21] D.J. O'Boy and V.V. Krylov, Damping of flexural vibrations in circular plates with tapered central holes. *Journal of Sound and Vibration*, **330**(10), 2220-2236 (2011).

[22] J. Daniel, E.P. Bowyer, and V.V. Krylov, Point mobility of a cylindrical plate incorporating a tapered hole of power-law profile. *The Journal of the Acoustical Society of America*, **129**(6), 3475-3482 (2011).

[23] V. Denis, A. Pelat, F. Gautier, and B. Elie, Modal Overlap Factor of a beam with an acoustic black hole termination. *Journal of Sound and Vibration*, **333**(12), 2475-2488 (2014).

[24] O. Aklouche, A. Pelat, S. Maugeais, and F. Gautier, Scattering of flexural waves by a pit of quadratic profile inserted in an infinite thin plate. *Journal of Sound and Vibration*, **375**, 38-52 (2016).

[25] D.J. O'Boy and V.V. Krylov, Vibration of a rectangular plate with a central power-law profiled groove by the Rayleigh-Ritz method. *Applied Acoustics*, **104**, 24-32 (2016).

[26] S.C. Conlon, J.B. Fahnline, and F. Semperlotti, Numerical analysis of the vibroacoustic properties of plates with embedded grids of acoustic black holes. *The Journal of the Acoustical Society of America*, **137**(1), 447-457 (2015).

[27] E.P. Bowyer and V.V. Krylov, Experimental study of sound radiation by plates containing circular indentations of power-law profile. *Applied Acoustics*, **88**, 30-37 (2015).

[28] E.P. Bowyer and V.V. Krylov, Sound radiation of rectangular plates containing tapered indentations of power-law profile. *Proceeding of Meetings on Acoustics*, **18**, 03002 (2013).

[29] L. Zhao, S.C. Conlon, and F. Semperlotti, Broadband energy harvesting using acoustic black hole structural tailoring. *Smart Materials and Structures*, **23**(6), 065021 (2014).

[30] L. Zhao, S.C. Conlon, and F. Semperlotti, An experimental study of vibration based energy harvesting in dynamically tailored structures with embedded acoustic black holes. *Smart Materials and Structures*, **24**(6), 065039 (2015).

[31] X.Q Zhou and F. Semperlotti, The energy absorption properties of Helmholtz resonators enhanced by acoustic black holes. *Inter-Noise*, Hamgurg, 2422-2430 (2016).

[32] V.V. Krylov and R.E.T.B. Winward, Experimental investigation of the acoustic black hole effect for flexural waves in tapered plates. *Journal of Sound and Vibration*, **300**(1-2), 43-49 (2007).

[33] V. Kralovic and V.V. Krylov, Damping of flexural vibrations in tapered rods of power-law profile experimental studies. Proceedings of the Institute of Acoustics, **29**(5), 66-73 (2007).

[34] E.P. Bowyer, J.M.L., V.V. Krylov and D.J. O'Boy, Experimental study of damping flexural vibrations in tapered turbofan blades. *Proceedings of the Acoustics 2012 Nantes Conference*, Nantes, France, 2201-2206 (2012).

[35] B.E. Anderson, M.C. Remillieux, P.Y. Le Bas, T. Ulrich, and L. Pieczonka, Ultrasonic radiation from wedges of cubic profile: Experimental results. *Ultrasonics*, **63**, 141-146 (2015).

[36] V. Denis, A. Pelat, and F. Gautier, Scattering effects induced by imperfections on an acoustic black hole placed at a structural waveguide termination. *Journal of Sound and Vibration*, **362**, 56-71 (2016).

[37] J.J. Bayod, Experimental Study of Vibration Damping in a Modified Elastic Wedge of Power-Law Profile. *Journal of Vibration and Acoustics*, **133**(6), 061003 (2011).

[38] E.P. Bowyer and V.V. Krylov, Slots of Power-Law Profile as Acoustic Black Holes for Flexural Waves in Metallic and Composite Plates. *Structures*, **6**, 48-58 (2016).

[39] E.P. Bowyer, V.V. Krylov, and D.J. O'Boy, Damping of flexural vibrations in rectangular plates by slots of power-law profile. *Proceedings of the Acoustics 2012 Nantes Conference*, Nantes, France, 2187-2192 (2012).

[40] E.P. Bowyer, D.J. O'Boy, V.V. Krylov, and F. Gautier, Experimental investigation of damping flexural vibrations using 2-D acoustic black hole. *Proceedings of ISMA2010 Including USD2010*, 1181-1192 (2010).

[41] E.P. Bowyer, D.J. O'Boy, and V.V. Krylov, Damping of flexural vibrations in plates containing ensembles of tapered indentations of power-law profile. *Proceeding of Meetings on Acoustics*, **18**, 03003 (2013).

[42] S. Yan, A.M. Lomonosov, and Z. Shen, Numerical and experimental study of Lamb wave propagation in a two-dimensional acoustic black hole. *Journal of Applied Physics*, **119**(21), 214902 (2016).

[43] W. Huang, H. Ji, J. Qiu, and L. Cheng, Wave Energy Focalization in a Plate With Imperfect Two-Dimensional Acoustic Black Hole Indentation. *Journal of Vibration and Acoustics*, **138**(6), 061004 (2016).

[44] E.P. Bowyer, and V.V. Krylov, Experimental investigation of damping flexural vibrations in glass fibre composite plates containing one- and two-dimensional acoustic black holes. *Composite Structures*, **107**(0), 406-415 (2014).

[45] P.A. Feurtado, and S. Conlon, An Experimental Investigation of Acoustic Black Hole Dynamics at Low, Mid, and High Frequency. *Journal of Vibration and Acoustics*, **138**(6), 061002 (2016).

[46] E.P. Bowyer, and V.V. Krylov, Damping of flexural vibrations in turbofan blades using the acoustic black hole effect. *Applied Acoustics*, **76**, 359-365 (2014).

[47] S. Foucauda, G. Michon, Y. Gourinata, A. Pelatb and F. Gautier, Immersed acoustic black hole as a travelling wave absorber understanding artificial cochlear mechanics. *Proceedings of the Acoustics 2012 Nantes Conference*, Nantes, France (2012).

[48] J.Y. Lee, and W. Jeon, Vibration damping using a spiral acoustic black hole. *The Journal of the Acoustical Society of America*, **141**(3), 1437-1445 (2017).

[49] L. Zhao, Passive Vibration Control Based on Embedded Acoustic Black Holes. *Journal of Vibration and Acoustics*, **138**(4), 041002 (2016).

[50] H. Zhu and F. Semperlotti, Phononic thin plates with embedded acoustic black holes. *Physical Review B*, **91**(10), 104304 (2015).

[51] H. Zhu and F. Semperlotti, Anomalous Refraction of Acoustic Guided Waves in Solids with Geometrically Tapered Metasurfaces. *Physical Review Letters*,

117(3), 034302 (2016).

[52] V.V. Krylov, Acoustic black holes: recent developments in the theory and applications. *IEEE Transactions on Ultrasonics, Ferroelectrics, and Frequency Control*, **61**(8), 1296-1306 (2014).

[53] L.L. Tang, L. Cheng, H. Ji, and J. Qiu, Characterization of acoustic black hole effect using a one-dimensional fully-coupled and wavelet-decomposed semi-analytical model. *Journal of Sound and Vibration*, **374**, 172-184 (2016).

[54] L. Cheng and R. Lapointe, Vibration attenuation of panel structures by optimally shaped viscoelastic coating with added weight considerations. *Thin-walled structures*, **21**(4), 307-326 (1995).

[55] L. Cheng, Vibroacoustic modeling of mechanically coupled structures: Artificial spring technique applied to light and heavy mediums. *Shock and Vibration*, **3**(3), 193-200 (1996).

[56] C.D. Bailey, Direct analytical solutions to non-uniform beam problems. *Journal of Sound and Vibration*, **56**(4), 201-507 (1978).

[57] S. Abrate, Vibration of non-uniform rods and beams. *Journal of Sound and Vibration*, **185**(4), 703-716 (1995).

[58] R.B. Bhat, Natural frequencies of rectangular plates using characteristic orthogonal polynomials in rayleigh-ritz method. *Journal of Sound and Vibration*, **102**(4), 493-499 (1985).

[59] D. Shi, Q. Wang, X. Shi, and F. Pang, Free Vibration Analysis of Moderately

Thick Rectangular Plates with Variable Thickness and Arbitrary Boundary Conditions. *Shock and Vibration*, **2014**, 1-25 (2014).

[60] S. Ng and Y. Araar, Free vibration and buckling analysis of clamped rectangular plates of variable thickness by the Galerkin method. *Journal of Sound and Vibration*, **135**(2), 263-274 (1989).

[61] I. Daubechies, Ten lectures on wavelets, *CBM-NSF conference series in applied mathematics*, Philadelphia: SIAM ED, (1992).

[62] T. Hou and H. Qin, Continuous and discrete Mexican hat wavelet transforms on manifolds. *Graphical Models*, **74**(4), 221-232 (2012).

[63] S.S. Rao, Mechanical vibrations. Addison-Wesley, (1995).

[64] L.L. Tang and L. Cheng, Loss of acoustic black hole effect in a structure of finite size. *Applied Physics Letters*, **109**(1), 014102 (2016).

[65] L.H. Sperling, Sound and vibration damping with polymers. *ACS Publications* (1990).

[66] V. Denis, A. Pelat, C. Touzé, and F. Gautier, Improvement of the acoustic black hole effect by using energy transfer due to geometric nonlinearity. *International Journal of Non-Linear Mechanics* (2016).

[67] L.L. Tang and L. Cheng, Enhanced Acoustic Black Hole effect in beams with a modified thickness profile and extended platform. *Journal of Sound and Vibration*, **391**, 116-126 (2017).

[68] L.L. Tang and L. Cheng, Broadband locally resonant band gaps in periodic

beam structures with embedded acoustic black holes. *Journal of Applied Physics*, **121**(19), 194901 (2017).

[69] M.H. Lu, L. Feng, and Y.F. Chen, Phononic crystals and acoustic metamaterials. *Materials Today*, **12**(12), 34-42 (2009).

[70] C. Xu, F. Cai, S. Xie, F. Li, R. Sun, X. Fu, R. Xiong, Y. Zhang, H. Zheng, and J. Li, Phononic Crystal Tunable via Ferroelectric Phase Transition. *Physical Review Applied*, **4**(3), 034009 (2015).

[71] T.Y. Huang, C. Shen, and Y. Jing, Membrane- and plate-type acoustic metamaterials. *The Journal of the Acoustical Society of America*, **139**(6), 3240 (2016).

[72] B. Morvan, A. Tinel, A.C. Hladky-Hennion, J. Vasseur, and B. Dubus, Experimental demonstration of the negative refraction of a transverse elastic wave in a two-dimensional solid phononic crystal. *Applied Physics Letters*, **96**(10), 101905 (2010).

[73] J. Pierre, O. Boyko, L. Belliard, J.O. Vasseur, and B. Bonello, Negative refraction of zero order flexural Lamb waves through a two-dimensional phononic crystal. *Applied Physics Letters*, **97**(12), 121919 (2010).

[74] Y. Wu, Y. Lai, and Z.Q. Zhang, Elastic metamaterials with simultaneously negative effective shear modulus and mass density. *Physical Review Letters*, **107**(10), 105506 (2011).

[75] Z. Liu, X. Zhang, Y. Mao, Y. Zhu, Z. Yang, C. Chan, and P. Sheng, Locally

resonant sonic materials. *Science,* **289** (5485), 1734-1736 (2000).

[76] A. Martin, M. Kadic, R. Schittny, T. Bückmann, and M. Wegener, Phonon band structures of three-dimensional pentamode metamaterials. *Physical Review B*, **86**(15): 155116 (2012).

[77] M.S. Kushwaha, P. Halevi, L. Dobrzynski, and B. Djafari-Rouhani, Acoustic band structure of periodic elastic composites. *Physical Review Letters*, **71**(13), 2022 (1993).

[78] X. Wen, J. Wen, D. Yu, G. Wang, Y. Liu, and X. Hang, Phononic Crystals. *National Defense Industry Press*, (2009) (In Chiese).

[79] J.S. Lee, S. Yoo, Y.K. Ahn, and Y.Y. Kim, Broadband sound blocking in phononic crystals with rotationally symmetric inclusions. *The Journal of the Acoustical Society of America*, **138**(3), EL217-222 (2015).

[80] S.R. Huisman, R.V. Nair, A. Hartsuiker, L.A. Woldering, A.P. Mosk, and W.L. Vos, Observation of sub-Bragg diffraction of waves in crystals. *Physical Review Letters*, **108**(8), 083901 (2012).

[81] Y. Xiao, J. Wen, G. Wang, and X. Wen, Theoretical and Experimental Study of Locally Resonant and Bragg Band Gaps in Flexural Beams Carrying Periodic Arrays of Beam-Like Resonators. *Journal of Vibration and Acoustics*, **135**(4), 041006 (2013).

[82] L. Liu and M.I. Hussein, Wave Motion in Periodic Flexural Beams and Characterization of the Transition Between Bragg Scattering and Local

175

Resonance. *Journal of Applied Mechanics*, **79**(1), 011003 (2012).

[83] M. Oudich and M. Badreddine Assouar, Surface acoustic wave band gaps in a diamond-based two-dimensional locally resonant phononic crystal for high frequency applications. *Journal of Applied Physics*, **111**(1), 014504 (2012).

[84] C. Goffaux and J. Sánchez-Dehesa, Two-dimensional phononic crystals studied using a variational method: Application to lattices of locally resonant materials. *Physical Review B*, **67**(14), 144301 (2003).

[85] M. Oudich, Y. Li, B.M. Assouar, and Z. Hou, A sonic band gap based on the locally resonant phononic plates with stubs. *New Journal of Physics*, **12**(8), 083049 (2010).

[86] L. Raghavan and A.S. Phani, Local resonance bandgaps in periodic media: theory and experiment. *The Journal of the Acoustical Society of America*, **134**(3), 1950-1959 (2013).

[87] C. Sugino, S. Leadenham, M. Ruzzene, and A. Erturk, On the mechanism of bandgap formation in locally resonant finite elastic metamaterials. *Journal of Applied Physics*, **120**(13), 134501 (2016).

[88] X. Wang and M.Y. Wang, An analysis of flexural wave band gaps of locally resonant beams with continuum beam resonators. *Meccanica*, **51**(1), 171-178 (2015).

[89] G. Wang, J. Wen, and X. Wen, Quasi-one-dimensional phononic crystals studied using the improved lumped-mass method: Application to locally resonant

beams with flexural wave band gap. *Physical Review B*, **71**(10): 104302 (2005).

[90] Y. Xiao, J. Wen, and X. Wen, Flexural wave band gaps in locally resonant thin plates with periodically attached spring–mass resonators. *Journal of Physics D: Applied Physics*, **45**(19), 195401 (2012).

[91] M.A. Badreddine and M. Oudich, Enlargement of a locally resonant sonic band gap by using double-sides stubbed phononic plates. *Applied Physics Letters*, **100**(12), 123506 (2012).

[92] H. Shen, J. Wen, D. Yu, and X. Wen, The vibrational properties of a periodic composite pipe in 3D space. *Journal of Sound and Vibration*, **328**(1-2), 57-70 (2009).

[93] Y. Xiao, J. Wen, D. Yu, and X. Wen, Flexural wave propagation in beams with periodically attached vibration absorbers: Band-gap behavior and band formation mechanisms. *Journal of Sound and Vibration*, **332**(4), 867-893 (2013).

[94] D.J. Mead, Wave propagation and natural modes in periodic systems: I. Mono-coupled systems. *Journal of Sound and Vibration*, **40**(1), 1-18 (1975).

[95] D.J. Mead, Wave propagation and natural modes in periodic systems: II. Multi-coupled systems, with and without damping. *Journal of Sound and Vibration*, **40**(1), 19-39 (1975).

[96] Y. Chen and L. Wang, Periodic co-continuous acoustic metamaterials with overlapping locally resonant and Bragg band gaps. *Applied Physics Letters*,

105(19), 191907 (2014).

[97] B. Yuan, V.F. Humphrey, J. Wen, and X. Wen, On the coupling of resonance and Bragg scattering effects in three-dimensional locally resonant sonic materials. *Ultrasonics*, **53**(7), 1332-1343 (2013).

[98] Q.J. Lim, P. Wang, S.J.A. Koh, E.H. Khoo, and K. Bertoldi, Wave propagation in fractal-inspired self-similar beam lattices. *Applied Physics Letters*, **107**(22), 221911 (2015).

[99] K. Matlack, A. Bauhofer, S. Krödel, A. Palermo, and C, Daraio, Composite 3D printed metastructures for low frequency and broadband vibration absorption. *Proceedings of the National Academy of Sciences of the United States of America*, **113**(30), 8386-8390 (2016).

[100] L. D'Alessandro, E. Belloni, R. Ardito, A. Corigliano, and F. Braghin, Modeling and experimental verification of an ultra-wide bandgap in 3D phononic crystal. *Applied Physics Letters*, **109**(22), 221907 (2016).

[101] Z.G. Chen and Y. Wu, Tunable Topological Phononic Crystals. *Physical Review Applied*, **5**(5), 054021(2016).

[102] P. Wang, L. Lu, and K. Bertoldi, Topological Phononic Crystals with One-Way Elastic Edge Waves. *Physical Review Letters*, **115**(10): 104302 (2015).

[103] O.R. Bilal and M.I. Hussein, Ultrawide phononic band gap for combined in-plane and out-of-plane waves. *Physical Review E*, **84**(6), 065701 (2011).

[104] L.L. Tang and L. Cheng, Ultrawide bandgaps in phononic beams with

double-leaf acoustic black hole indentations. *The Journal of the Acoustical Society of America* , **142**, 2802-2807 (2017).